Mechanical Characterization and Aging Induced Evolution of Cyclic Properties and Microstructure of Lead-Free Solder Materials

by

Md Mahmudur Rahman Chowdhury

A dissertation submitted to the Graduate Faculty of
Auburn University
in partial fulfillment of the
requirements for the Degree of
Doctor of Philosophy

Auburn, Alabama
May 02, 2020

Keywords: lead-free solder, aging, cyclic loading, dopants, mechanical properties, and microstructure

Approved by

Jeffrey C. Suhling, Chair, Quina Professor of Mechanical Engineering
Hareesh V. Tippur, McWane Professor of Mechanical Engineering
Nima Shamsaei, Philpott-WPS Associate Professor of Mechanical Engineering
Michael J. Bozack, Professor Emeritus of Physics

Abstract

Solder joints in electronic assemblies are often subjected to cyclic (positive/negative) mechanical strains and stresses. Such exposures can occur in variable temperature application environments or during accelerated life thermal cycling tests used for qualification. Lead free solder materials are widely used in the electronic packaging industry due to environmental concerns. However, experimental testing and microstructural characterization have revealed that Sn-Ag-Cu (SAC) lead free solders exhibit evolving properties that change significantly with isothermal aging and cyclic loading. This dissertation addresses those changes in the microstructure and properties of lead free solders by conducting four different projects.

In the first project, three new Bi-doped SAC solder materials (SAC_R, SAC_Q, and Innolot) have been chemically analyzed and then mechanically tested at high temperature in order to determine the nine Anand parameters. The nine Anand parameters were determined for each unique solder alloy from a set of uniaxial tensile tests performed at several strain rates and temperatures. Later, cyclic stress-strain behavior of these three doped alloys have been investigated and compared with the standard lead-free solder alloy.

In the second project, the effects of isothermal mechanical cycling on damage accumulation in lead free SAC305 and SAC_Q solder joints have been explored. Uniaxial samples of SAC305 and SAC_Q have been prepared and subjected to various durations of prior mechanical cycling. The cycled samples were then subsequently subjected to stress-strain or creep testing. The cycling induced degradations of several mechanical properties (elastic modulus, yield strength, ultimate strength, and creep strain rate) have been characterized and quantified with the amount of prior cycling. Moreover, these evolutions observed in the two lead free alloys have been correlated with the observed changes in their microstructures that occurred during the cycling.

In the third part of this dissertation, the aging induced evolutions of the cyclic stress-strain behavior of three different doped SAC solder materials has been investigated. The specimens were aged at 125 °C for different durations (0-6 months) and the evolution of the hysteresis loop area, peak load, and plastic strain range have been characterized. Later, the effects of prior aging on damage accumulation occurring in SAC305 and SAC_Q have been investigated while subjected to mechanical cycling (fatigue testing). Regions of interest near the center of the sample were marked using a nanoindentation system. Samples were then subjected to aging at 125 °C. After aging, the samples were then subjected to mechanical cycling. After various durations of cycling (e.g. 0, 10, 25, 50, 75, 100, 200, 300 cycles), the fixed were examined using scanning electron microscopy (SEM) Using the recorded images, the microstructural evolutions in the fixed regions were observed, and the effects of the initial aging on the results were determined.

In the last project, the mechanical cyclic induced evolutions in mechanical properties of SAC 305 individual solder joint have been investigated. The test assemblies in this study were (3X3) BGA packages composed of total nine 0.75 mm diameter lead free solder balls which were formulated by reflowing solder spheres soldered onto 0.55 mm diameter Cu pads on FR4 coupons. The solder balls were cycled using an Instron Micromechanical tester along with a newly designed fixture which facilitates the tester to cycle a solder ball individually. Nanoindentation tests were performed on the specimens to study the evolution in mechanical properties (e.g. elastic modulus, hardness and creep strain rate) of the solder balls as a function of duration of cycling.

Acknowledgments

I would like to express my sincere gratitude to my major professor Dr. Jeffrey C. Suhling for his support, excellence guidance, encouragement, and constructive remarks in every aspect of completing my PhD at Auburn University. I am grateful for getting the opportunity to work with a mentor like him. He is one of my role models and a source of inspiration. I am deeply grateful to my advisory committee members including Dr. Hareesh V. Tippur, Dr. Michael J. Bozack, and Dr. Nima Shamsaei for their insightful discussion about this research work. Special thanks are extended to my friends and co-workers Dr. Jordan Roberts, Dr. Munshi Basit, Dr. Md Hasnine, Dr. Sudan Ahmed, Dr. Nianjun Fu, Dr. Quang Nguyen, Dr. Promod Chowdhury, Dr. Mohammad Alam, Abdullah Fahim, Jing Wu, Jun Chen, KM Rafidh Hasan, Mohd Aminul Hoque, Kamrul Hasan, Mohammad Ashraful Haq, Debabrata Mondal and Mohammad Al Ahsan for their friendship and support.

I am also grateful to my family members especially to my Parents, my brother and sister, relatives, friends and all of my well-wisher for their continuous support and prayers throughout my life. Finally, I solemnly dedicate this dissertation and all achievements in pursuit of doctoral degree to my wife Mahi Mashriva Hossain and daughter Mahveen Chowdhury, for their love, support, and heartfelt consideration.

Table of Contents

List of Figures

List of Tables

CHAPTER 1

INTRODUCTION

1.1 Overview of Solders in Microelectronics

Solders have been used as the interconnecting material in electronic assemblies to provide both electrical and mechanical connections between components. As a joining material, in electronic assemblies, solder provides mechanical support, electrical and thermal interconnection between the semiconductor device (Si die) and the bonding pad. It also helps to dissipate the heat generated from the Si-chip [1].

In the past, the conventional eutectic or near eutectic Sn-Pb solder has been extensively used as primary interconnect material in electronic packaging industries. The eutectic (63Sn-37Pb) tin-lead alloy was very attractive due to its relatively low melting temperature (183 ^{o}C), which allows the soldering process compatible with most of the substrate materials and devices. Lead (Pb) provides many technical advantages to tin-lead solders that includes 1) prevent allotropic transformation of β-tin to α-tin at low temperature, 2) enhance wetting by lowering the surface tension of the solder and 3) increase corrosion resistance of the solder by formation of a oxide film which is insoluble and resistant to chemical attack etc.[1, 2].

However, lead is poisonous to human being as well as animals. According to a recent study, lead (Pb) in the child's blood could cause serious problem in neurological and physical development. Moreover, being a toxic element, it has some detrimental effect on the environment [2-8]. As a result, despite of all the advantages of tin-lead solders, governments of many countries are imposing regulations against the use of lead in the electronic devices [1, 2]. As an effort of eliminating lead in electronics, the EU adopted two directives, 1) the Waste of Electrical and Electronic Equipment (WEEE) and 2) the Directive of the Restriction of the Use of Certain Hazardous Substances (RoHS) in June 2000 [9]. As a result of the enforcement of the directives, all electrical or electronic equipment and devices produced in or imported to E.U. member states must comply with these lead-free standards except those items that are exempted from the bans. In addition to legislation enforcement there are emerging detection technologies to enforce compliance. So due to the general push towards the eco-efficiency and green electronics, manufacturers are motivated for the adoption of lead free electronics. Therefore, the conversion to lead free solders in the global electronic market appears imminent [10].

In the United States, as soon as lead-free solder legislation was proposed, the lead-free solder project headed by the NCMS initiated research and development of lead-free solder in a program lasting 4 years [11]. The results of the project have been made available in a database and offer information on such matters as modifying equipment and processes for selecting alternative materials. The project initially selected for study 79 types of alloys considered at the time to be potential candidates for use in lead-free solder. Basic attributes considered included toxicity, resource availability, economic feasibility, and wetting characteristics. The selection process narrowed the field down to the final seven alloys, and these received secondary evaluation for reliability and ease of mounting manufacturing. Evaluation of the individual alloys did not result in the final selection of a single candidate, but three alloys, Sn–58Bi, Sn–3.5Ag–4.8Bi, and Sn–3.5Ag, were recommended as candidates. Screening comments indicated that the Sn–58Bi eutectic alloy was not suitable for use as standard solder due to the scarcity of Bi resources. However, since this material can be used for mounting at less than 200 °C, and has chalked up a 20-year plus record of use in mainframe computers, this solder was deemed suitable for special applications. These results were used to construct a database on lead-free solder that includes the information in these tables along with other items such as (1) recommended applications for lead-free solder, (2) alloy composition guidelines reflecting price and availability, (3) database of the 7 selected alloys and comparison with Sn–Pb eutectic alloy, (4) data on the characteristics of the other 70 eliminated alloys, (5) optimal process conditions using various test PWBs, (6) strength evaluation and metallurgical reaction analysis for the selected alloys and various surface mounting process reactions, (7) predicted life (using NCMS Project proprietary life prediction software) and thermal fatigue evaluation for 4 of the selected alloys, and (8) assessment of nontoxicity and alloy composition.

1.2 Lead Free Solders

While selecting the suitable lead free alternative, it is important to consider that the properties of the lead free solder must comparable or superior to Tin-lead (Sn-Pb) solders. The performance requirement of solder alloys, for microelectronics application, are very strict. In general, the lead free solder alloy must have desired level of electrical and mechanical properties, melting temperature, wetting capability on most common PCB substrates etc. while at the same time must not enhance assembly cost. Compatible candidates of the Sn-Pb solders must have the following behaviors [3]:

- Melting temperature similar to eutectic Sn-Pb for a similar reflow profile
- Sufficient wettability for good metallization process
- Good electrical properties for transmitting electrical signals
- Strong mechanical properties for good fatigue resistance and reliability

- Inexpensive and easier manufacturability

Among various alloy systems that are considered as lead-free solder candidates, Sn-Ag-Cu alloys have been recognized as the most promising because of their relatively low melting temperature (compared with the Sn-Ag binary eutectic lead free solder), superior mechanical properties, and good compatibility with other components [12-14]. Sn-Ag-Cu alloys are widely used as lead-free solutions for ball-grid-array (BGA) interconnection in the microelectronic packaging industry as solder balls and pastes. Although no "drop in" replacement has been identified that is suitable for all applications, Sn-Ag, Sn-Ag-Cu (SAC), and other alloys involving elements such as Sn, Ag, Cu, Bi, In, and Zn have been identified as promising replacements for standard 63Sn-37Pb eutectic solder. Industries have proposed several SAC alloys which include 96.5Sn-3.0Ag-0.5Cu (SAC 305) in Japan, 95.5Sn-3.8Ag-0.7Cu (SAC 387) in the EU, and 95.5Sn-3.9Ag-0.6Cu (SAC 396) in the USA. The International Printed Circuit Association has suggested that 96.5Sn-3.0Ag-0.5Cu (SAC305) and Sn-3.9Ag- 0.6Cu (two near-eutectic alloys) will be the most widely used alloys in the future [15]. This prediction is attributed to their good mechanical properties, acceptable wetting properties, and suitable melting points [13, 16, 17].

1.3 Candidates for Alternative Lead Free Solders

About 70 different alloys were proposed as an alternative to the Sn-Pb solder. Most of these are Sn based solder where Sn is the main constituent along with one, two or even three other minor elements. These minor elements are added mainly to 1) decrease the melting temperature and 2) improve wetting and reliability of the solder [1]. The properties of Sn and the effects of different alloying elements on the Sn based solder alloys are described below:

1.3.1 Tin

The melting temperature of elemental Sn is 231 ºC. One of the main reasons of choosing Sn as the principle component in the lead free solder for electronic applications is its ability to spread and wet a number of various different substrates. In the solid state, tin can have two different phases or crystal structures 1) white or β-Sn with tetragonal crystal structure and 2) gray or α-Sn with diamond cubic crystal structure. At the room temperature the thermodynamically stable phase is β-Sn. Upon cooling, when the temperature goes below 13 ºC (allotropic transformation temperature), α-Sn becomes the thermodynamically stable phase. The allotropic transformation of β-Sn to α-Sn, results a significant volume change (around 27%) causing blistering of the tin surface, cracking or disintegration. This phenomenon is mainly a surface event and often referred as 'tin pest'. The low ductility of α-Sn is another reason of causing blistering and cracking of the tin after the transformation [1, 4, 5]. Although the equilibrium temperature for β-Sn to α-Sn is 13 ºC, the transformation occurs only after a significant undercooling and an extensive incubation period as long as several years. For example, no 'tin pest' was found on a SAC387 bulk sample after storing at -40 ºC for 5 years [5]. Presence of heterogeneous nuclei, also known as seeding, can considerably accelerate the kinetics of the transformation. The possibility of β → α transformation in a actual solder joint is even limited due to the constraints (component and substrate) on the both side of the joint [4, 5].

Addition of other elements, as an impurity, can affect the allotropic transformation. For example, the presence of Pb, Bi, Sb, Cu, Ge and Si inhibit β → α transformation while the presence of As, Zn, Al and Mg promote the transformation [4, 5].

Sn has a body centered tetragonal crystal structure (β-Sn), at room temperature, which is anisotropic. Hence, tin shows an anisotropic thermal (e.g. CTE) and mechanical (e.g. elastic modulus) properties as shown in Figure 1.1. As a result, during thermal cycling experiment, cracking occurs along the grain boundaries [1].

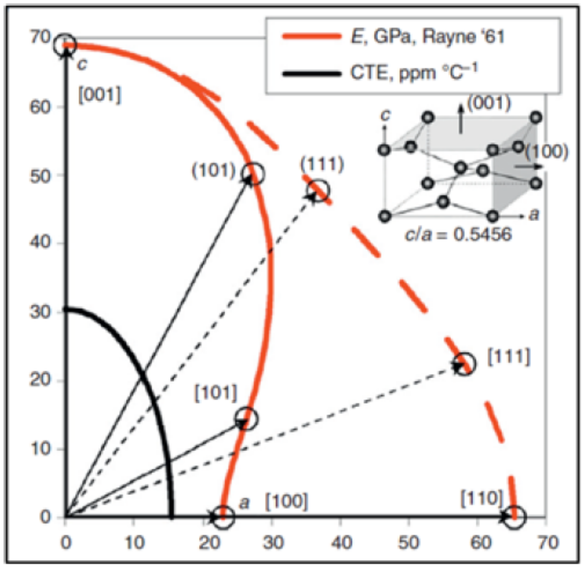

Figure 1.1 Elastic Modulus and Coefficient of Thermal Expansion (CTE) of Tin as a Function of Crystal Orientation [1]

1.3.2 Chromium (Cr)

Cr helps to improve shear ductility after long term aging. Besides, it also suppress kirkendall void formation in the solder joints [6].

1.3.3 Nickel (Ni)

Among all the micro-alloy additives, Ni is one of the most common element. Addition of Ni improves fluidity of SAC solders. Ni also improves the high strain rate properties of solder joints. For example, the drop strength of SAC alloys can be significantly improved by Ni addition. Although Ni does not have any significant influence on the creep properties of the solder, it inhibits Cu diffusion and thus reduce the thickness of Cu_3Sn intermetallic compound (IMC). The Ni addition greater than 0.01 wt% could suppress the growth of Cu_3Sn IMC even after long term (2000 hours) aging. Since Cu_3Sn IMC is very brittle, the growth of Cu_3Sn layer is very critical for the brittle failure of the solder joints. Addition of Ni on SAC solder causes to form more stable $(Cu, Ni)_6Sn_5$ IMC which act as a barrier layer and suppress the growth of Cu_3Sn layer. Therefore, by reducing the thickness of brittle Cu_3Sn layer, Ni helps to improve share strength of the solder joints. Ni also helps to improve strength by refining solder microstructure [7].

1.3.4 Zinc (Zn)

While Ni reduces only the formation Cu_3Sn, Zn doping can retard both Cu_3Sn and Cu_6Sn_5 IMC's in SAC solders. Zn also helps to improve the interface quality after multiple reflow and high temperature aging. Addition of 1.5% Zn in SAC207 solder could refine Ag_3Sn and Cu_6Sn_5 IMC's and hence increase strength by dispersion strengthening [6].

1.3.5 Cobalt (Co)

Co helps to reduce the growth of Cu_3Sn layer during high temperature aging. Addition of small amount of Co (<0.1 wt%) can improve the properties of SAC solders. Co increases the number of nucleation sites and hence significantly refine the grains of SAC305 solder. Thus it helps to improve shear strength of the solder joints [6].

1.3.6 Bismuth (Bi)

If added in small amount, Bi can improve the wetting ability and reduce melting temperature of lead free solder alloys. It also increases strength of the bulk solder and inhibit the large Ag_3Sn formation in the bulk solder. It is recommended to avoid Pb contamination in the solder before using Bi as an additive. Because Bi can react with Pb to form a brittle IMC at the grain boundary and reduce strength significantly. If present in excess amount, Bi can cause solidification crack due to the increase in the gap between solidus and liquidus temperature [6].

1.3.7 Antimony (Sb)

Sb improves mechanical properties of lead free solders but it is toxic in nature. A small percentage (0.5 wt%) of Sb can improve drop test reliability of SAC solder joints [8]. Besides, Sb also helps to enhance strength of the solder by solid solution strengthening [7].

1.3.8 Germanium (Ge)

Ge doped solders shows low Cu dissolution from the Cu pad and hence suitable for the wave soldering process. Ge significantly improve wetting properties of the lead free solders and refine the solder microstructure. As a result, Ge addition improves the strength and ductility of the lead free solder [8].

1.3.9 Sn-Ag-Cu System

A variety of SAC alloys with different chemical compositions have been the proposed by various user groups and industry experts. Among the various lead free solder candidates, Sn-Ag-Cu alloys have gained a significant interest in the academia as well as in the industry because of their superior mechanical properties, relatively low melting temperature, and good solderability or wetting properties [18, 19] . A graphical representation of the market share of different lead free solders is presented in Figure 1.2. It is clear from the figure that Sn-Ag-Cu alloys are dominating in the lead free solder market.

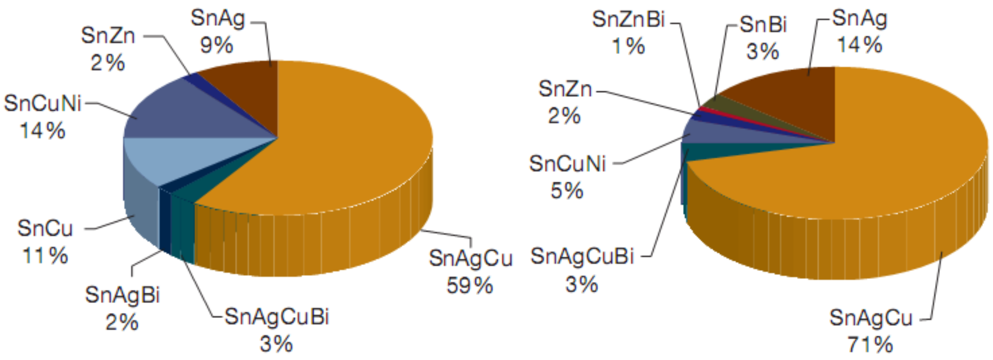

(a) Wave Solders (b) Reflow Solders

Figure 1.2 Market Share of Lead Free Solder
(https://www.ameslab.gov/files/LeadFreeSolder_Foundation.pdf)

Figure 1.3 shows a typical 3-D ternary phase diagram. The contours on the top surfaces of the figure represent the isothermal lines. Each of the 3 sectors represents the binary phase diagram of two of the three elements. The center of the diagram, where the isothermal lines reach the common, lowest point, is the eutectic point of the ternary system.

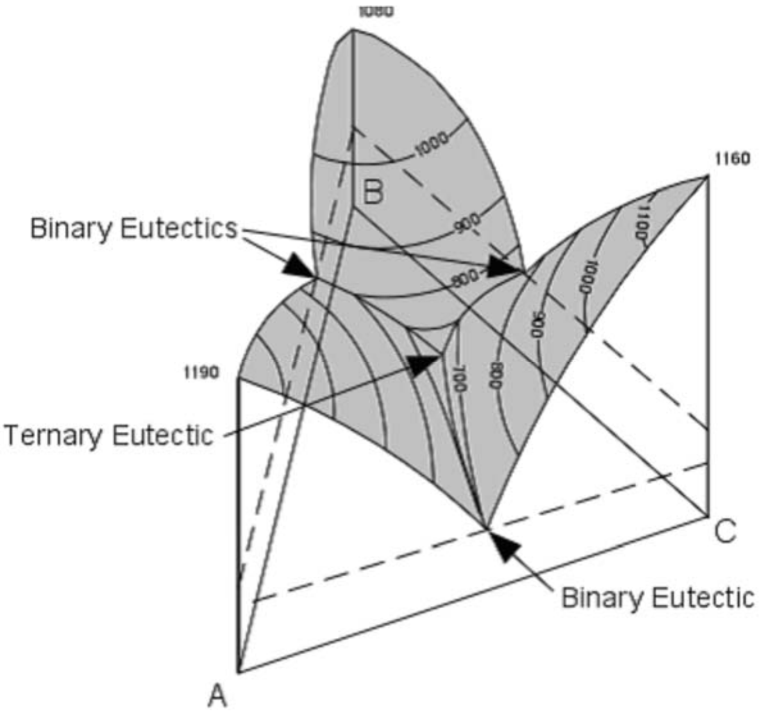

Figure 1.3 Typical 3-D Ternary Phase Diagram

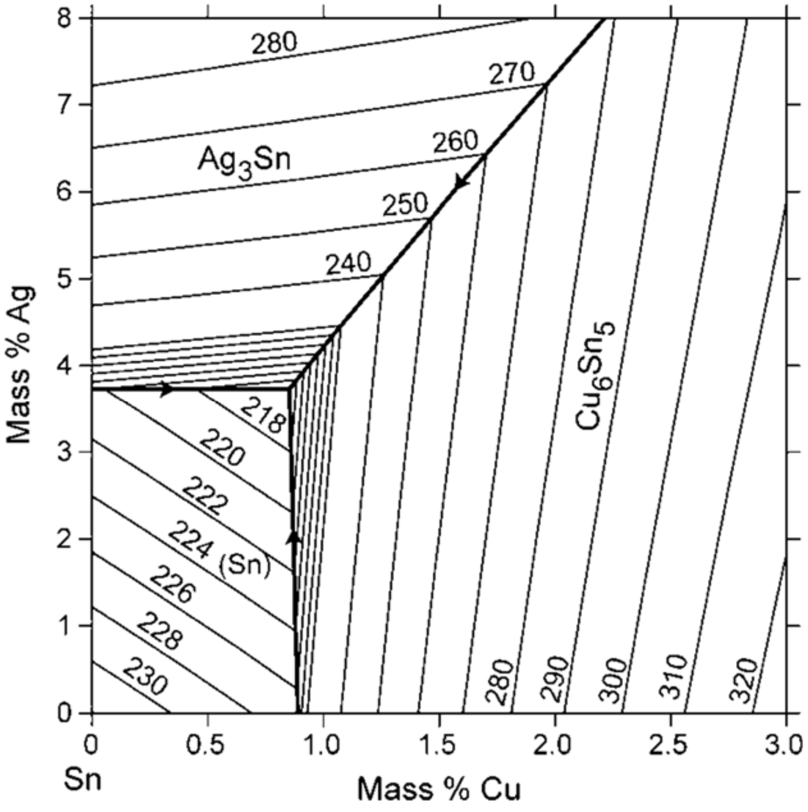

Figure 1.4 Sn-Ag-Cu Ternary Phase Diagram

Figure 1.4 is the top view (2-D) of the ternary phase diagram of Sn-Ag-Cu. The area indicated in the red box is the near eutectic region. Most of the SAC alloy compositions currently on the market are within this region. The eutectic and near eutectic melting temperature has been determined to be 217 °C, although the precise eutectic point is not known [20]. In SAC alloys, the formation of intermetallic compounds between the primary elements Sn and Ag, and Cu affect all the properties of the alloys. There are three possible intermetallic compounds that may be formed: Ag_3Sn forms due to the reaction between Sn and Ag and Cu_6Sn_5 forms due to the Sn and Cu reaction. The compound Cu_3Sn will not form at the eutectic point unless the Cu content is high enough for the formation of Cu_3Sn at higher temperatures, so in bulk specimens Cu_3Sn is not presented. There is no reaction between Ag and Cu to form any kind of intermetallic compounds. Figure 1.5 shows a typical microstructure of SAC lead free solders. The near eutectic SAC solidifies into three phases, i.e., β-Sn (primary phase), Ag_3Sn and Cu_6Sn_5. It consists of β-Sn dendrites surrounded by interdendritic eutectic regions incorporating a fine dispersion of Ag_3Sn and Cu6Sn5 intermetallic particles in β-Sn. The volume fraction of Ag_3Sn IMCs is much higher than that of Cu_6Sn_5 IMCs in SAC solder microstructures. The particles of intermetallic compounds possess much higher strength than the bulk material. Fine intermetallic particles in the Sn matrix can therefore strengthen the alloys. The intermetallic compounds can also improve the fatigue life of the solders, as SAC alloys are reported to be 3-4 times better fatigue properties than the Sn-Pb eutectic solders. Moreover, the dendrite structure can effectively pin and block movement of dislocations and therefore improve solder mechanical behavior.

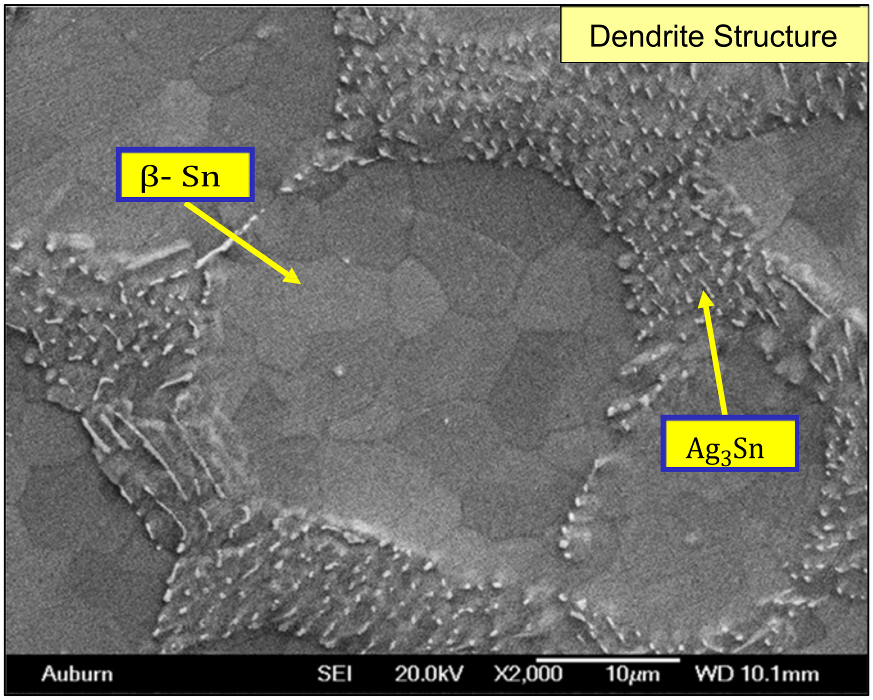

Figure 1.5 Typical Microstructure of SAC Lead Free Solders

During the initial stages of the development of lead free solder, eutectic Sn-Ag-Cu alloy (SAC387: 95.5Sn-3.8Ag-0.7Cu) was most popular. But, due to the cost of the patent by Iowa State University and the higher Ag%, SAC305 (96.5Sn-3.0Ag-0.5Cu) was seen to be advantageous over SAC387. Moreover the performance of SAC305 is similar to that of the eutectic Sn-Ag-Cu alloy. As a result, the electronic industry has chosen SAC305 to use in most of the lead-free applications [6].

1.3.10 Sn-Ag-Cu + X System

Despite the benefits mentioned above, SAC family solders sometimes are still questionable as complete substitutes for eutectic Sn-Pb because of costs, some patent issues, aesthetic consideration, and relatively high melting temperature (217 °C vs. 183 °C). Moreover, due to the increased price of Ag, the cost of SAC305 solder bar has increased about 3 times in the past 10 years [6]. Besides, the mechanical properties of the lead free alloy is not stable during the long time exposure at an elevated temperature (aging effect). It has been reported previously, that isothermal aging causes a significant reduction in the reliability of the lead free solder joints [21]. As a result, people are now looking for a low cost alternative with better reliability than SAC305. According to the results of many recent studies, performance characteristics of SAC solder alloys are able to be optimized by doping, that is, by adding a small amount of other alloying elements into the SAC solder alloys.

The proposed doping element candidates include Bi, Ni, Co, Ge, Zn, La, Mg, Mn, Ce, Ti, Fe, In, B, etc. For example, adding 0.05% (wt.) Ni can successfully stabilize the microstructure, inhibit the excessive consumption of metal base and thus increase the reliability of the solder joints [22-24]. In addition, doping rear earth (RE) elements can significantly enhance wettability, refine microstructure and improve ductility of SAC alloys [25-28]. Even though dopants can greatly alter the mechanical, electrical and physical behavior of SAC solders, the effect on melting temperature, however, is found to be negligible. This is another advantage for doped solder alloys because manufacturers can still use the same processing conditions as conventional SAC alloys. However, it takes much more time and cost to figure out the optimal composition levels for the dopants.

1.4 Mechanical Properties of Lead Free Solders

For the SAC lead free solders, the properties of Sn dominate their behavior as Sn has a very high weight percentage. Sn has a Body-Center Tetragonal (BCT) crystal structure with lattice parameters a = b = 5.83Å and c = 3.18 Å. Therefore, it is highly anisotropic in mechanical properties such as elastic modulus and hardness. In other words, the mechanical properties of Sn are highly dependent on the grain orientation. As shown in Figure 1.6, the elastic modulus of Sn is 67.6 GPa in the (001) direction, while it is only 23.6 GPa in the (100) direction [29]. Also, Sn is highly thermally anisotropic: the coefficients of thermal expansion (CTE) in the principal directions at 30 ºC are α[100] = α[010] = 16.5 × 10^{-6} ºC^{-1} and α[001] = 32.4 × 10^{-6} ºC^{-1} [30].

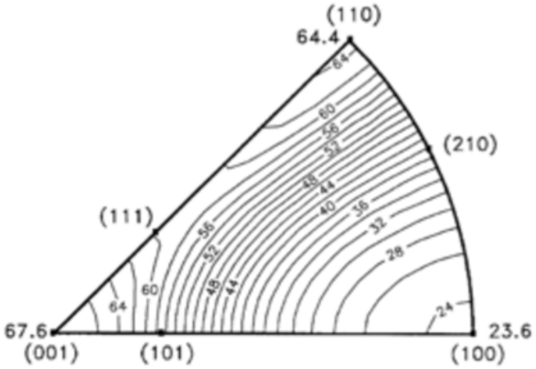

Figure 1.6 Variation of Elastic Modulus of β-Sn with Grain Orientation [22]

In an electronic device, a number of different types of engineering materials exists in a close proximity. For example, a printed circuit board (PCB) is typically a glass fiber reinforced polymer (composite material), a die is a semiconductor material which is often encapsulated in a plastic or a ceramic, and the tracking and the solder joints are metallic materials. Solder joints are used to create an electrical circuit by mounting chips and components on the PCB. Hence an ideal solder joint should have a good conductivity to transmit electrical signals and at the same time, adequate strength to provide mechanical support and connection. Hence, mechanical properties of solder joints are critically important to ensure reliability of the electronic products. Among all the mechanical properties, tensile, fatigue, and creep performance of the solder are critically important. Thus an accurate measurement of mechanical properties and development of constitutive equations for solder materials are required in mechanical design, process optimization and reliability assessment.

1.4.1 Tensile Properties (Stress-Strain Behavior)

Under the action of an increasing stress, metals usually exhibit elasticity, plasticity, and a maximum in stress is followed by necking and fracture. The slope of the linear elastic portion of the stress vs. strain plot is the modulus, and the stress at termination of elastic behavior is the yield stress. Tensile properties indicate how the material will react to forces being applied in tension. Although in real life, actual solder joints are rarely under uniaxial tensile load, these properties are required for design purpose. Tensile properties help to determine the response of a material under uniaxial tension loading. Tensile tests provide us information about several material properties, such as ultimate tensile strength (UTS), yield strength (YS), effective elastic modulus (E), elongation, etc.

The tensile behavior of a material is commonly described by a stress-strain curve. A tensile test experiment typically provide a load-elongation curve which is then converted into a stress-strain curve using following equations:

$$\sigma_e = \frac{F}{A_o} \tag{1.1}$$

$$\varepsilon_e = \frac{\Delta L}{L_o} = \frac{L_f - L_o}{L_o} \tag{1.2}$$

Where, F is the applied load, A_o is the initial cross-sectional area, L_o is the initial length, L_f is the final length (after deformation), σ_e is the engineering stress, and ε_e is the engineering strain. Since the change in physical shape is negligible, for most of the cases, ‘engineering’ stress-strain curves are used instead of ‘true’ stress-strain curves. A typical stress-strain curve for a ductile material is presented in Figure 1.7. As shown in the figure, stress and strain shows a linear relationship at the beginning of the test. In this linear portion of the curve, stress and strain follows a particular relationship known as Hook's Law which is described as:

$$\sigma = E\varepsilon \tag{1.3}$$

Where E is the effective elastic modulus which is defined by the slope of the initial portion of the stress-strain curve. No plastic deformation occurs in the linear elastic part of the stress-strain curve. Hence theoretically, within the linear portion, if the stress is released, the material should come back to its original shape (zero deformation). However, for a viscoplastic material like solder, time dependent plastic deformation or creep occurs even with a small load (below yield stress). As a result, the value of effective elastic modulus, obtained from stress-strain curve, is typically smaller than the value of modulus measured from a dynamic measurement technique like ultrasonic or acoustic method. The rapid wave propagation, in a dynamic technique, mostly eliminates any inelastic deformation [31-33].

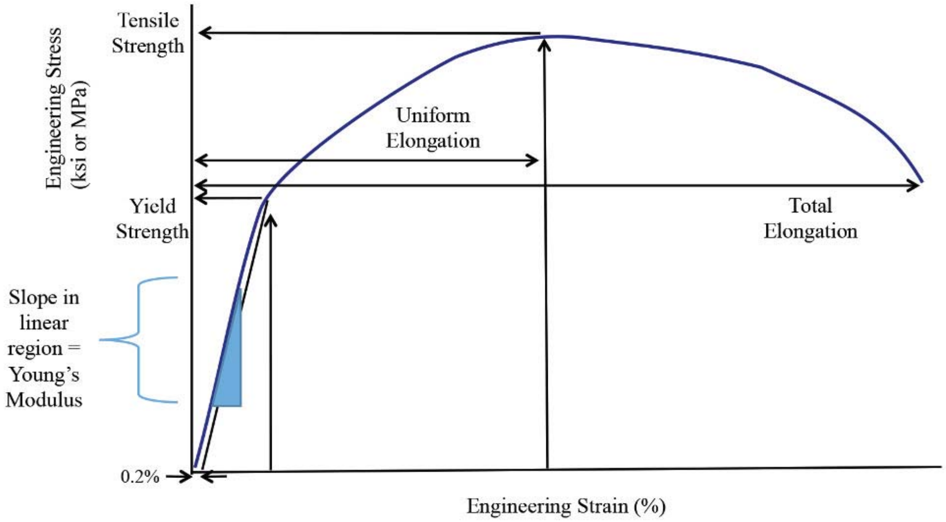

Figure 1.7 Typical Tensile Test Response of a Ductile Material

[https://www.thefabricator.com/article/metalsmaterials/getting-to-know-more-about-the-metal-you-are-forming]

Eventually, after a certain period of time the stress-strain curve become nonlinear. This nonlinearity is caused by the stress induced inelastic deformation or plastic flow of the material. In this stage, the atoms of the test specimen undergoes a rearrangement among themselves and moves to a new equilibrium position. In a crystalline material, like solder, this rearrangement is caused by dislocation motion. The point where the curve begins to show a nonlinear behavior or inelastic plastic flow is called yield point and the stress associated with the point is known as yield strength (YS). Since it is difficult to identify the exact stress that caused the plastic flow, YS is typically defined as the stress required to cause 0.2% plastic deformation. Yield strength of a material can be determined from the stress-strain curve by drawing a line parallel to the initial linear portion but 0.2% offset from the origin. The stress associated with the intersection of the parallel line and the stress-strain curve is the yield strength of the material. The ultimate tensile strength (UTS) or tensile strength is defined as the maximum stress obtained from a uniaxial tension test. After UTS, the decrease in stress (as shown in Figure 1.7) is due to the localized deformation also known as necking in the test sample. If the test continues beyond the UTS, the test sample will eventually break or fail. The stress associated with it is called failure strength and strain at the failure point is known as total elongation (Figure 1.7).

1.4.2 Creep

Creep deformation refers to the time dependent plastic flow or deformation of a material that occurs when the material is exposed to a constant load, typically below yield strength, for a long period of time. Creep deformation becomes significant when the material operates at a high homologous temperature (T_h), which is defined by the ratio of operating temperature (T) and the melting temperature (T_m) of the material.

$$T_h = \frac{T}{T_m} \tag{1.4}$$

Creep deformation becomes the dominant failure mode in a metallic material if T_h is greater than $0.5T_m$. [34]. The melting temperature of lead free SAC solder is around 217 ºC (490 K) causing T_h for the alloys, for room temperature (298 K) operating conditions, is $0.61T_m$. As a result, lead free SAC solder alloys display creep deformation even in room temperature operating condition. Due to the mismatches of the coefficient of thermal expansion (CTE) of silicon chip and other assembly materials used in an electronic package, solder joints are remain under mechanical stress. These mechanical stresses can cause time dependent creep deformation of solder materials. In microelectronic packaging, creep deformation is regarded as one of the major failure mechanisms of solder joints [35].

Creep test is typically conducted by applying a constant uniaxial load on the test specimen at a particular temperature. During the test, deformation of the test specimen is recorded as a function of test time and the result of the creep test is presented as a 'creep strain' vs. 'time' plot. The extent of creep deformation significantly depends on the applied stress level and the test temperature. Figure 1.8 represents a typical creep curve which consists of three distinct regions, after the initial jump, namely, primary, secondary, and tertiary regions.

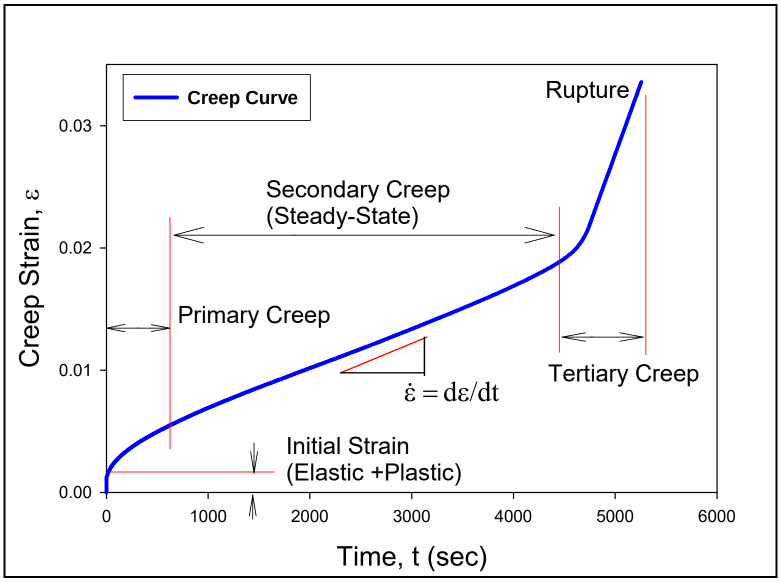

Figure 1.8 Typical Creep Curve

Every creep test begins with an initial strain which corresponds to the instantaneous response (mostly elastic) of the material due to the applied force/load. In the primary creep stage, the material starts to deform with at a high strain rate (high slope at the beginning of the primary region) and then the strain rate decrease gradually with increasing time. This is due to the work hardening of the material which resists deformation. Eventually, with increasing test time, the creep strain rate reaches to a steady state stage which is known as steady state creep or secondary creep region. The constant creep rate, in the secondary stage, is due to the dynamic balance between strain hardening and recrystallization [36]. The strain rate in the secondary stage is very important since very often researchers use this parameter in the finite element simulations to predict reliability of the solder joints under different test conditions. After secondary creep, the material enter into the tertiary creep region followed by an immediate rupture. Tertiary region begins when the strain rate start increasing abruptly from the constant value.

1.4.3 Fatigue

Thermally cycling induced solder joint fatigue is a common failure mode in electronic packaging. When subjected to temperature changes, stresses in electronic assemblies are typically developed due to the mismatches in CTE of the soldered components and the Printed Circuit Board (PCB). Cyclic temperature changes, either due to external environment or power switching, can therefore lead to substantial alternating stresses and strains within the solder joints. During cyclic loading, micro cracks form within the solder material followed by macro cracks which leads to damage and ultimately to fatigue failure (see Figure 1.9). The facts that the original bulk design strengths are not exceeded and the only warning sign of an impending fracture is an often indiscernible internal crack, make fatigue damage especially dangerous for electronic packages.

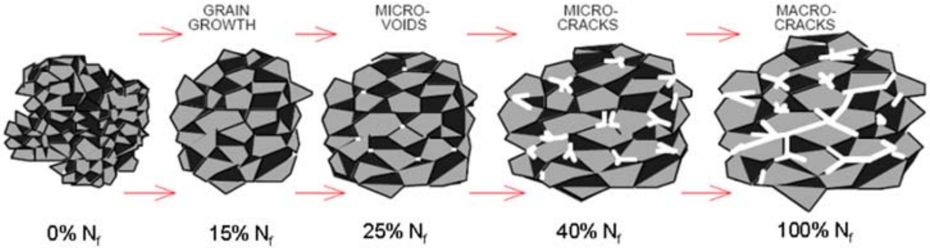

Figure 1.9 Depiction of the Effects of the Accumulating Fatigue Damage [37]

Fatigue test results are obtained by cycling smooth or notched specimens until failure, and are presented in a form of S-N diagram (where S is the stress amplitude, and N the number of cycles to failure) as shown in Figure 1.10. Since the 1950s, researchers have developed several models to predict the number of cycles to failure of solder materials including the Engelmaier-Wild equation [37], Palmgren-Miner linear damage law, Coffin-Manson relation [38], etc.

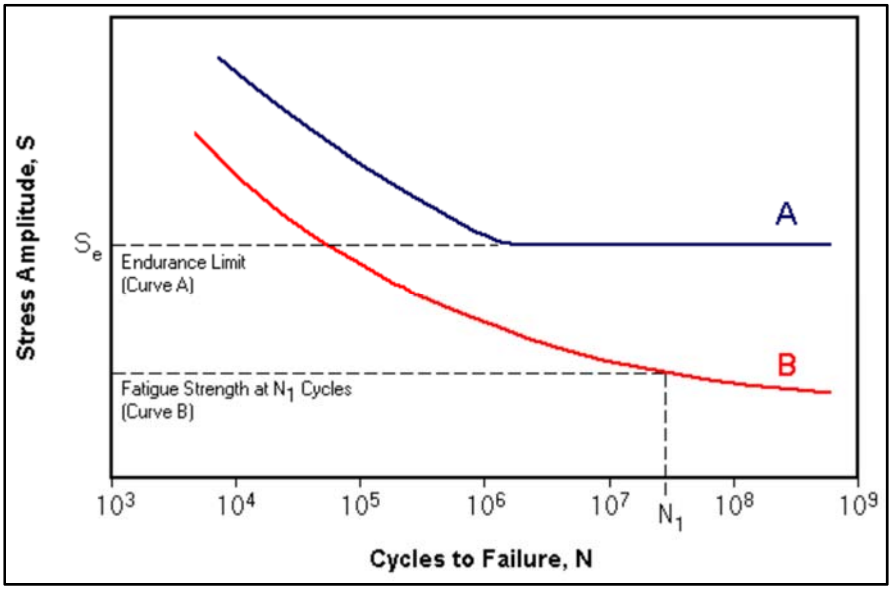

Figure 1.10 Typical S-N Curve for Ductile Materials
(http://www.mdme.info/MEMmods/MEM30007A/properties/Properties.html)

During fatigue damage process, slip occurs first, followed by cracks that can be seen only at high magnification. These cracks continue to grow under cycle loading and eventually become visible to the unaided eye. The cracks tend to combine such that just a few major cracks grow. These cracks (or crack) reach a critical size, and sudden fracture occurs. The higher the stress magnitude, the sooner all processes occur. Cracks may also stop without further growth as a result of compressive residual stress fields or as a crack grows out of a high-stress region such as a notch. Thus fatigue generally consists of crack nucleation, growth, and final fracture. At high stress levels, a large portion of the total fatigue life is associated with microcrack and macrocrack growth. At low stress levels, a great deal of the total fatigue life is spent in the nucleation of the crack and microcrack growth.

1.4.4 Cyclic Stress-Strain Behavior

The stress-strain behavior obtained from a monotonic tension or compression test can be quite different from that obtained under cyclic loading. This was first observed during the late nineteenth century by Bauschinger [39]. His experiments indicated that the yield strength in tension or compression was reduced after applying a load of the opposite sign that caused inelastic deformation. Therefore, one single reversal of inelastic strain can change the stress-strain behavior. Three types of cyclic stress-strain behavior can be obtained for most of metal alloys at different initial conditions [40] as shown in Figure 1.11: (a) cyclic hardening for fully annealed condition, (b) both cyclic hardening and softening for partially annealed condition, and (c) cyclic softening for cold-worked condition. The mechanism of hardening and softening can be described in terms of dislocation substructure, motion, and slip. If dislocations are constrained to move or glide and slip is minimized, the material is said to cyclically harden. Reconfiguration of the dislocation structure can also tend to promote greater dislocation mobility. Therefore, dislocations are able to circumnavigate around microstructural barriers that generally tend to restrict deformation, such as precipitates and grain boundaries. Thus, such a material is said to cyclically soften.

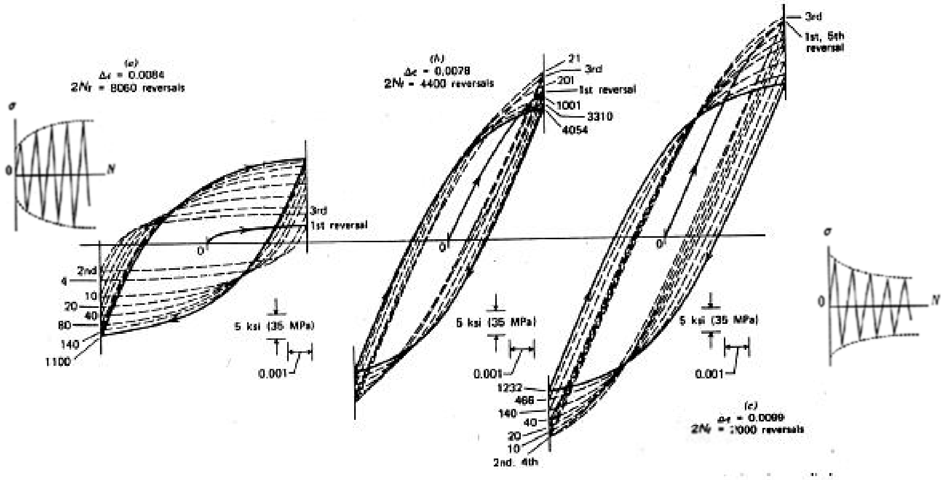

Figure 1.11 Cyclic Stress-Strain behavior of Alloys (a) Cyclic hardening (b) Cyclic Hardening and Softening (c) Cyclic softening

1.5 Objectives of This Research

This research mainly concentrates on the effects of aging on the microstructure and the cyclic stress-strain or fatigue behavior of doped Sn-Ag-Cu (SAC) lead free solders. Also, some work will be done to better understand the damage accumulation that occurs in lead free solders during fatigue testing. The general objectives of this research are:

(1) Investigate the mechanical properties of three new doped Pb-free solder alloys (SAC_R, SAC_Q, and Innolot) at several high temperatures (125, 150, 175, 200 °C) and different strain rates. Examine mechanical properties of lead free solders of interest and explore the effects of aging on them;

(2) Determine a New Set of Anand model Parameters Considering over a wide range of temperatures and strain rates and investigate the correlation of Anand model predicted results and experimental results;

(3) Investigate the cyclic stress-strain behavior of doped SAC solder alloys and compare the results with conventional SAC305 lead free solder alloys to examine the effect of the dopants;

(4) Characterize the effects of aging on the cyclic stress-strain behavior of doped SAC solder alloys and compare with the results of a standard SAC solder alloy (SAC 305);

(5) Explore the mechanical cycling induced evolution of cyclic stress-strain behavior, stress-strain behavior (Elastic Modulus, Yield Stress, and Ultimate Strength), and creep behavior of SAC305 and SAC_Q lead free solder;

(6) Develop an experimental technique to obtain the microstructural evolution occurring in a fixed region of SAC305 and SAC_Q lead-free solder materials after different cycling periods;

(7) Examine the aging induced microstructural changes occurring in small fixed regions of reflowed (RF) SAC305 and SAC_Q lead free solder materials and correlate the changes with experimental results.

(8) Develop an experimental setup to investigate the effects of mechanical shear cycling on the constitutive behaviors of individual Pb-Free Solder joints during fatigue testing.

1.6 Organization of the Dissertation

This dissertation is presented in the following chapters:

Chapter 1: Introduction to lead free solders alloys and mechanical properties of solder materials.

Chapter 2: Literature review on isothermal aging effects, mechanical properties of lead free solder, cyclic stress-strain behavior, effects of aging on solder mechanical properties, microstructural evolution during aging of SAC alloys, life prediction and reliability models of electronic packages.

Chapter 3: Description of experimental procedure, sample preparation, experimental equipment, empirical models and data processing.

Chapter 4: Study on the mechanical behavior of lead free solder alloys subjected to extreme high temperature application and applicability of Anand viscoplastic model for high temperatures.

Chapter 5: Characterization of the cyclic stress-strain behavior (hysteresis loop area, peak stress and plastic strain range) of doped SAC lead free solders, and the study on the effects of aging on the fatigue behavior of doped SAC solder alloys.

Chapter 6: Investigation of the evolution of constitutive behavior (stress-strain and creep), cyclic stress-strain behavior and microstructure of doped ASC solder materials during fatigue testing.

Chapter 7: Visualization of the aging induced microstructure evolution of SAC305 and SAC_Q solder alloys due to cyclic loading in fixed regions.

Chapter 8: Investigation on the evolution of mechanical properties (modulus, hardness, and secondary creep rate) of individual solder joints due to shear cyclic loading.

Chapter 9: Summary and conclusions of the dissertation.

CHAPTER 2

LITERATURE REVIEW

2.1 Introduction

Thermally cycling induced solder joint fatigue is a common failure mode in electronic packaging. Lead free solder joints in electronic assemblies are typically subjected to cyclic loadings, either in actual application or in accelerated life testing used for qualification. When exposed to extreme temperature thermal cycling, these solder joints experience a cyclic shear strain caused because of the differences in coefficients of thermal expansion of the various components of the package. Cyclic temperature changes can therefore lead to substantial alternating stresses and strains within the solder joints. Energy dissipation occurs during such cyclic loading due to yielding and occurrence of viscoplastic deformations, and the strain energy density dissipated per cycle can be calculated from the area of stress-strain hysteresis loops. The cycling eventually leads to micro cracks being formed within the solder material, followed by macro cracks which leads to damage progression and ultimately to fatigue failure. Similar effects also occur in lead free solder uniaxial samples subjected to tension and compression cyclic loading when they are exposed to isothermal repetitive mechanical cycling between two fixed strain extremes. The material damage that occurs during cyclic loading becomes immediately evident through the “load drop” and “widening” that occurs in the cyclic stress-strain curves as cycling progresses. Eventually, this damage leads to micro crack formation, crack growth, and failure. Aging of solder materials degrades their mechanical and creep properties, and will exacerbate the rate of damage accumulation during cycling loading.

As the electronic industries transition to lead free soldering by the motivation of environmental concerns, legislative mandates, and market differentiation, great efforts have been undertaken to develop desirable lead free solders and establish a corresponding database of material properties. Many researchers have attempted to measure the key mechanical properties of lead free solders. However, large discrepancies have been found in the published data from various groups. There are several reasons for these discrepancies. Firstly, the differences in specimen preparation methods among the researchers cause different microstructures in the specimens that directly affect the experimental results significantly. Secondly, the testing methods and the test conditions may also be different which will again affect the results. Thirdly, mechanical properties obtained from the bulk solders might be different from the measured properties of solder joints. Finally, the lack of standardization in the data acquisition and processing of mechanical properties makes it difficult to obtain good laboratory-to-laboratory comparisons. Apart from the above mentioned reasons for the discrepancies in solder material properties, another critical factor is aging effects. Aging is mostly neglected in the majority of prior studies, which will further exacerbate these problems. Thermal aging causes changes in the microstructure and hence the mechanical response of lead free solders. Changes in mechanical response include reductions in the initial effective elastic modulus, yield stress, and ultimate strength, as well as increased creep rates. Solder joints with highly degraded microstructure and material properties are so vulnerable that the service life of the package is often severely shortened.

2.2 Effects of Isothermal Aging on Solder Mechanical Properties

Several studies have been performed on degradation of solder material properties when the alloys are exposed to isothermal aging. For example, Ma, et al. [41] studied the evolution of Young’s modulus, yield stress, and ultimate tensile strength of SAC305 and SAC405 solder alloys under various aging conditions. A linear-exponential model was developed to describe the material property evolution. They have shown that the material properties decreased dramatically in the first 20 days for both room temperature aging as well as elevated temperature aging. After 20 days of aging, the properties change slowly and linearly and it continues for longer aging time. Zhang, et al. [42] also studied the aging effects on tensile properties of SACN05 (N = 1%, 2%, 3% and 4% silver) series solders for different amount of aging at temperatures 25-125 °C. They have demonstrated that the mechanical properties degraded more dramatically when the aging temperature was increased. The data also shows that the degradation becomes linear with longer aging time. Cai, et al. [43] have also shown that the aging effects are significant for lead free solders (SAC105, SAC205, SAC305 and SAC405) for room temperature aging as well as elevated temperature aging. They have also shown that the aging effects can be reduced by using certain dopants to (e.g. Bi, In, Ni, La, Mg, Mn, Ce, Co, Ti, Zn, etc.) SAC solder alloys to enhance the reliability of lead free solders. Che, et al. [44] have measured stress-strain curves for various SAC alloys at different strain rates, while Zhu, et al. [45] have measured the mechanical properties of SAC305 at different strain rates and temperatures. The mechanical properties of a lead free solder are strongly influenced by its microstructure, which is controlled by its thermal history including solidification rate and thermal aging after solidification. Due to aging phenomena, the microstructure, mechanical response, and failure behavior of lead free solder joints in electronic assemblies are constantly evolving when exposed to isothermal aging and/or thermal cycling environments. Such aging effects are greatly exacerbated at higher temperatures typical of thermal cycling qualification tests. However, significant changes occur even with aging at room temperature [45].

Aging effects on the constitutive and failure behaviors of lead free solders have been studied extensively by several prior researchers [21, 41-55]. In early investigations, the mechanical properties and creep behavior of SAC alloys were shown to be severely degraded by prior exposure to room temperature (25 °C) and elevated temperature (50, 75, 100, and 125 °C) aging [21, 41-47]. The measured stress-strain data demonstrated large reductions in stiffness, yield stress, ultimate strength, and strain to failure (up to 50%) during the first 6 months after reflow solidification. After approximately 10-20 days of aging, the lead free solder joint material properties were observed to degrade at a slow but constant rate. In addition, even more dramatic evolution was observed in the creep response of aged solders, where up to 10,000X increases in the secondary creep rates were observed for aging up to 6 months. The aged solder materials were also found to enter the tertiary creep range (imminent failure) at much lower strain levels than virgin solders (non-aged, tested immediately after reflow solidification). Mustafa, et al. [48] have demonstrated that the hysteresis loop area in cyclic (tension/compression) loading of various SAC solder alloys changes significantly with aging. For strain controlled tests, the hysteresis loop area deceases and for the stress controlled tests, the loop area increases with aging time. Using the developed approaches, the influence of aging on the fatigue life of lead free alloys was also examined [49]. Zhang and coworkers [50-52] have shown that large reductions in the thermal cycling reliability of BGA test assemblies occurs when they are subjected to aging prior to accelerated life testing. Motalab, et al. [53, 54] have included aging effects in the Anand constitutive model and energy density based failure criterion for SAC solders, and then used these theories with finite element analyses to predict the thermal cycling life of aged BGA assemblies. Good correlations were achieved with the measured lifetimes from references [50, 51]. Other groups have also noted the strong effects of aging, and extensive listing of references can be found in [21, 41-54].

2.3 Constitutive Modelling for Solder Models (Anand Model)

In the electronic packaging industry, it is important to be able to make accurate predictions of board level solder joint reliability during thermal cycling exposures. The solder material constitutive law plays an important role in the development of thermo-mechanical models for microelectronic assemblies. Under thermo-mechanical loading, the solder material undergoes elastic and in-elastic deformations. Elastic deformations are recoverable, while inelastic deformations consist of time-independent plastic deformations and time-dependent creep deformations, which are not recoverable. Solder constitutive behavior can be represented by a combination of elastic, plastic (isotropic or kinetic hardening), and viscoplastic/creep models. The linear elastic region in a uniaxial stress-strain curve can be modeled by Hooke’s law where stress and strain are related by an elastic modulus (E). The plastic strain hardening region can be modeled by a time-independent non-linear stress-strain relationship based on either isotropic or kinematic strain hardening. Isotropic hardening assumes that the origin of the von Mises yield surface remains stationary in the stress space and the size of its yield surface expands resulting from strain hardening. In kinematic hardening, the von Mises yield surface does not change in size, but the origin of the yield surface is allowed to translate in the stress space to model strain hardening effects of increasing plastic flow stress. For solder materials, the tensile stress and strain curves are dependent on the test temperature and strain rate. The elastic modulus (E), yield stress (YS) and the tensile strength (UTS) properties vary with temperature and strain rate.

The Anand viscoelastic constitutive model is often used to represent the material behavior of the solder in finite element simulations. This model is defined using nine material parameters, and the reliability prediction results are often highly sensitive to the Anand parameters. The viscoplastic constitutive equations proposed by Anand [55] have become popular for rate-dependent deformation of metals at high temperatures. They were initially developed for structural metals, but have been adopted for microelectronic solders (Sn-Pb and lead free) for homologous temperatures in excess of 0.5Tm. The so-called Anand model has been widely applied for the solder stress-strain relations in finite element simulations of electronic packages, where solders undergo small elastic deformations and large viscoplastic deformations. For example, Che, et al. [56] have considered multiple constitutive theories, and then demonstrated that the Anand equations were well matched with predictions of lead free solder fatigue life. In addition, Pei and coworkers [57] have calculated the nine parameters of the Anand model by conducting tensile testing of Sn3.5Ag and Sn3.8Ag0.7Cu lead free solders at several temperatures and strain rates.

Mysore, et al. [58] have found the Anand material parameters for SAC305 (Sn3.0Ag0.5Cu) lead free solder alloy by performing double lap shear tests. They suggested that the Anand parameters for solder joint samples are significantly different than those measured by testing of bulk solder specimens. In addition, Motalab, et al. [59] have evaluated the Anand parameters for SAC305 solder using two approaches, including stress-strain testing and creep testing. Bai and coworkers [60] suggested a modified approach for SAC305 (Sn3.0Ag0.5Cu) lead free solder where strain rate and temperature dependent values were included for Anand model parameter ho. The Anand model constants for SAC105 (Snl.0Ag0.5Cu) lead free solder have been reported by Amagai, et al. [61] and Kim, et al. [62]. Finally, Basit et al. reported the Anand model constants for SACN05 (N=1, 2, 3, 4) lead free solder, different solidification profile and aging effects [63].

2.4 Reduction of Aging Effect by Dopant

Addition of 4th element in the SAC solder is known as doped SAC alloy. Dopants (microalloy additions) play an important role to control microstructure and mechanical properties of the alloy. Dopants have been found to strongly influence the properties and behaviors of lead free solders. For example, addition of Bismuth (Bi) as a dopant has been demonstrated to have several beneficial effects. Bi helps to reduce solidification temperature, increases strength by means of precipitation hardening, and also helps to reduce IMC (Intermetallic Compound) layer thickness in lead free solder materials [64]. The Effect of Bi on the mechanical properties of a SAC (Sn3.5Ag0.9Cu) alloy was investigated by Matahir and coworkers [65]. They reported that the shear strength increased with increasing Bi addition up to 2 wt%. Beyond that point, the shear strength decreased with increasing Bi%. Improved shear strength might attribute to the role of Bi on the morphology of microstructure and distribution of dominant IMC (Ag_3Sn). Reduction of strength at higher Bi content was due to the evolution of Bi rich phase and fragmentation of the IMC. Pandher, et al. [66] also reported that addition of 2% Bi in SAC alloys improves wetting and alloy spreading.

Zhao, et al. [67] found that addition of 0.02% Ni to SAC105 increased the formation of NiCuSn IMC and reduced the localized grain size at solder/NiAu pad interface. In addition, the effects using various doped elements (i.e. Co, Fe, In, Ni, Zn and Cu) in SAC305 BGA solder joints on Cu pads were studied by Sousa, et al. [68]. They concluded that addition of low levels of Zn had a significant beneficial effect on the interfacial IMC. Lee and coworkers [69] found that micro-alloying SAC alloys with Ni and Bi improved thermal fatigue life and drop impact resistance. Yeung, et al. [70] studied a novel lead-free solder SACQ. Based on drop test, thermal cycling, and finite element simulation, they conclude that the doped alloy has improved board level reliability when compared to SAC105.

Sun et. al. [71] reviewed the effects of different alloying elements (Mn, Fe, Bi, Ni, In, Zn, Ga, Sb, Mg,) Rear Earth (RE) Elements (Ce, La, Y, Er, Pr, Nd, Yb,) and nanoparticles (Al_2O_3, Al, TiO_2, ZnO, ZrO_2, CNT, Graphene, CeO_2, TiB_2, Ni-Coated CNT, Mo, SiC, $SrTiO_3$, Co) on melting temperature, wettability, mechanical properties, microstructure, interfacial reaction and Sn whiskers.

For SAC305 solder, average width of eutectic region was found as 6.8 ± 2.8 μm and grain size of β-Sn was 24.8 ± 5.9 μm. Indium (In), helps to refine IMC and Sn-rich phase as well as makes the microstructure more uniform. Titanium (Ti) can significantly reduce Sn grain size and width of eutectic region by heterogeneous nucleation of IMC's. Iron (Fe) forms large $FeSn_2$ IMC which has a weak interface with β-Sn matrix. Magnesium (Mg) helps to coarsen eutectic region. Addition of Al in SAC105 refines β-Sn dendrites and enlarge eutectic regions. Besides, it also prevent Ag_3Sn and Cu_6Sn_5 and forms two new IMC Ag_3Al and Al_2Cu. Zn also helps to refine β-Sn dendrites significantly. Ni was found to reduce the size of Sn-rich phase and refine the microstructure. Since Antimony (Sb) has higher affinity towards Sn, presence of Sb reduces the driving force to form Cu-Sn IMC's resulting a narrow IMC layer in the solder joint. Sb also helps to refine IMC grain size.

RE elements can significantly refine the microstructure of SAC solders. Er can reduces the particle size of Ag_3Sn and Cu_6Sn_5 whereas Pr and Nd refine β-Sn dendrites and IMC particle size by forming uniformly dispersed fine $RESn_3$. These fine particles act as heterogeneous nucleation sites during solidification. However, excessive amount of RE elements will cause to form bulk $RESn_3$ phase which has a negative effect on mechanical properties. La, Ce and Y also have a similar effect on solder microstructure.

Al and Ni nanoparticle was found to reduce IMC particle size, spacing and IMC layer thickness by forming very fine and uniformly dispersed Sn-Ni-Cu and Sn-Sg-Al IMCs. Addition of small amount of Fe nanoparticles refine the microstructure and forms $FeSn_2$ phase. Al_2O_3 nanoparticles increase the size of eutectic region and reduce Ag_3Sn particle size. TiO_2 and SiC nanoparticle reduces the size and spacing between Ag_3Sn particles. $SrTiO_3$ nanoparticle reduces the size of Ag_3Sn and Cu_6Sn_5 particles by promoting the rate of nucleation during solidification. ZnO suppresses Ag_3Sn and Cu_6Sn_5 IMC formation and reduces β-Sn grain size by 22%.

The Effect of dopants on the aging induced changes in microstructure was also studies by a number of scientists. Sadiq et. al. [72] worked with different Lanthanum (La) doped SAC305 alloys and recorded the changes in microstructure and mechanical properties during isothermal aging at 150 °C for 6 different aging conditions (i.e. 0 , 10, 25, 50, 100 and 200 hours). They reported that La drastically reduces the IMC particle size and also significantly inhibit the growth of IMC particles during isothermal aging. Based on polarized light image they found that in as cast condition, grain size of SAC305 was ~8 mm and was significantly reduced (~1 mm) after La addition. From the graph presented in that paper, it is also clear that aging doesn't have any significant influence in average grain size.

In another study, Lee et. al. [73] studied the effect of Lanthanum (La) addition and high temperature storage on the microstructure and microhardness of Sn-3.5Ag solder joints. Their experimental results confirms that addition of La refine the solder microstructure. They explained that during solidification of the solder, $LaSn_3$ compounds form at the beginning and provide extra nucleation sites for Ag_3Sn IMC to grow resulting a refine microstructure. Addition of La was also found to reduce the thickness of IMC layer after soldering as well as isothermal aging. They also reported that La addition helps to improve microhardness and thermal resistance of solder joints.

Hao et. al. [74] studied the effects rare earth element Er addition on the evolution of microstructure of lead free eutectic SAC (Sn-3.8Ag-0.7Cu) solder joints during isothermal aging. Aging was conducted at 170 ºC for 4 different holding periods (i.e. 0, 200, 500 and 1000 hours). The authors measured the thickness of IMC layer of Sn-3.8Ag-0.7Cu and Sn-3.8Ag-0.7Cu-0.15Er alloy after different aging duration. They found that Er addition reduces the thickness of IMC layer in as reflowed condition and also significantly reduces the growth during aging. They argued that Er combines with Sn to form $ErSn_3$ IMC and reduces the activity of Sn which subsequently suppress the formation of Cu_6Sn_5 IMC layer. They also observed that $ErSn_3$ IMCs formed during solidification of solder act as a heterogeneous nucleation site for Ag_3Sn and Cu_6Sn_5 precipitates. The increase in nucleation sites results a refinement of Ag_3Sn and Cu_6Sn_5 particles. Addition of Er also found to make the microstructure more uniform and reduce the coarsening rate of the IMCs during isothermal aging.

Witkin [75] and Delhaise et al. [76] studied the effect of aging of Bi doped SAC alloys. In both study, the authors reported an elimination or at least reduction of aging induced degradation in SAC-Bi alloys.

2.5 Cyclic Stress-Strain Behavior of Solder Materials

The stress-strain behavior obtained from a monotonic tension or compression tests can be quite different from that obtained under cyclic loading. This was first observed during the late nineteenth century by Bauschinger [39]. His experiments indicated that the yield strength in tension or compression was reduced after applying a load of the opposite sign that caused inelastic deformation. Thus, one single reversal of inelastic strain can change the stress-strain behavior of metals. In the early 1960s, Morrow [40] reviewed several experimental techniques and methods for interpreting results and also illustrated typical phenomenological cyclic-dependent deformation and fracture behavior. He observed that a stable hysteresis loop quickly developed under cyclic conditions. Based on this observation, he also developed a descriptive theory of fatigue based upon cumulative plastic strain energy as a criterion for fatigue damage, and elastic strain energy as a criterion for fracture. He demonstrated quantitatively that the fatigue properties of a metal can be related to its cyclic stress-strain properties.

Many prior researchers have studied the cyclic stress-strain behavior of solder materials. Models to predict fatigue life of solder alloys under thermal cycling or thermomechanical fatigue loading have been developed in several investigations [77-84].

For example, Guo, et al. [78] investigated the evolution of the hysteresis loops for both thermomechanical fatigue and isothermal fatigue for 63Sn-37Pb solder, and also compared the hysteresis loops found at various failure cycles. They performed mechanical cyclic tests at 25 °C and 80 °C under strain control for strain limits of 0.3% to 3%. For thermal cycling, they tested between 25 °C and 80 °C, with a 120 second ramp. They also developed a mathematical correlation between the sizes of the isothermal hysteresis loop and thermal cycling hysteresis loop. Busso, et al. [79] studied cyclic stress-strain behavior of 60Sn-40Pb solder using cyclic torsion tests performed on a feedback controlled servo-hydraulic testing machine. They also developed a viscoplastic constitutive model that included a strong Bauschinger effect exhibited by solder during cyclic loading. Frear, et al. [80] observed that under conditions of cyclic strain, the microstructure of 60Sn-40Pb alloy experienced a heterogeneous coarsening. They then developed a microstructure based finite element simulation methodology for the prediction of solder joint fatigue life. Yang, et al. [84] investigated cyclic stress-strain behavior of 63Sn-37Pb solder under triangular waveform, trapezoid waveform, and multi-level dwell time waveform cyclic loading.

Measurement of deformations during thermal cycling and stress-strain hysteresis in solder joints have also been examined. For example, Hall [85-86] experimented the stress-strain hysteresis of a leadless ceramic chip carrier (LCC) mounted to an organic PCB during the thermal cycling. Another research conducted by Pao [87-89] evaluated the thermo-mechanical hysteresis of different Sn-based alloys using a 2-beam geometry. In addition, Haacke, et al. [90] characterized both the thermomechanical fatigue and hysteresis for Sn-Pb solder. For lead free solders, Raeder and co-workers [91] have investigated the thermomechanical deformation behavior of Sn-Bi eutectic solder under cyclic loading, and the findings were quantified using the plastic strain energy density. Later, Dusek, et al. [92] explored the cyclic stress-strain behavior and hysteresis loop evolution for Sn-Ag-Cu (SAC) lead free solders during isothermal fatigue at several different temperatures (T = 25, 30, 60, and 125 °C) and found that the number of cycles to fatigue failure increased with the increment of temperatures for the same stress level. They have also claimed this phenomenon attributed to the use of slow cycling, where creep and stress relaxation play dominant roles. Hu, et al. [93] reported that under constant strain range, the stress range decreased during cyclic testing of Sn-Pb solder. They also observed the fifth hysteresis loops at 22 C for total strain ranges of 1%, 2%, and 5%, and reported that with increasing strain range, the area of the hysteresis loops increased. The stress range was found to have decreased by 85% as the temperature was increased from 22 C to 50 C. Shi, et al. [94] studied the effects of frequency and temperature on hysteresis loops during cyclic loading. They reported that the area of the hysteresis loops decreased with the reduction of the frequency from 1 Hz to 0.0001 Hz, and that the area of hysteresis loop also decreased with the increasing testing temperature from 25 °C to 150 °C. Kanchanomai, et al. [95] have performed uniaxial fatigue tests on Sn-Ag solder, while Pang and coworkers [96] have performed uniaxial fatigue tests on SAC387 lead free solder. Mustafa, et al. [48] investigated the aging induced evolution of the cyclic stress-strain and fatigue properties of bulk lead-free SAC solder specimens.

2.6 Isothermal and Thermomechanical Fatigue Criteria for Solder Materials

Several previous studies have been conducted on the fatigue behavior of lead free solders. Herkommer, et al. [97] have developed a damage model that is capable of predicting material behavior under both mechanical shear cycling and thermal cycling loading conditions. Zhang and Dasgupta [98-99] have discussed the mechanical and thermal cycling durability of selected lead-free solders (Sn3.9Ag0.6Cu, Sn3.5Ag, and Sn0.7Cu), and developed a mechanical fatigue damage criterion. They demonstrated good correlation between predictions of their criterion and experimental cycles to failure under different strain rates and temperature conditions. Whitelaw, et al. [100] have determined the parameters of the Bonder-Partom model from uniaxial cyclic stress-strain tests for both lead-free and Sn-Pb solders. They have also verified their model under isothermal mechanical cycling conditions. Korhonen, et al. [101] conducted uniaxial cyclic tests at various temperatures for near eutectic Sn-Ag-Cu alloy to understand the isothermal fatigue behavior. Nucleation and growth mechanisms of fatigue damage were also observed using optical microscopy, scanning electron microscopy (SEM), and the Electron Back-Scattering Diffraction (EBSD) method. Fatigue failure behavior and cyclic creep deformation were observed by Shang, et al. [102], and they related the fatigue behavior to cyclic stress amplitude, number of cycles, stress ratio, frequency, temperature, alloy composition, and microstructure for different lead-free solders. Both uniaxial cyclic tests and shear cyclic tests were carried out by Andersson, et al. [103] to establish a comparison between the isothermal mechanical fatigue properties of lead free solder joints and bulk solders. The fatigue ductility exponent in the Coffin-Manson law for a Sn-Ag-Cu micro-solder joint was investigated by Kanda, et al. [104] in terms of the cyclic strain-hardening property and inelastic strain energy in fracture for isothermal fatigue. They established a relationship between the equivalent inelastic strain range and the fatigue life under triangular and trapezoidal waves for both as-soldered and aged specimens. Shang, et al. [102] reviewed the recent fatigue studies of Sn-rich Pb-free solder alloys to provide an overview of the current understanding of cyclic deformation, cyclic softening, fatigue crack initiation, fatigue crack growth, and fatigue life behavior in those alloys. Fossum, et al. [105] proposed a practical viscoplastic damage model to characterize 95.5Sn-3.9Ag-0.6Cu lead free solder under cyclic thermomechanical loading conditions. Isothermal low cycle mechanical fatigue tests of solder joints for 63Sn-37Pb, Sn-3.7Ag, Sn-4.0Ag-0.5Cu and Sn-8Zn-3Bi solders were performed by Andersson, et al. [106]. They found that Sn-4.0Ag-0.5Cu lead free solder exhibited the best isothermal fatigue properties. Kanchonmai, et al. [95] performed low cycle fatigue tests of Sn-3.5Ag eutectic lead free solder under various temperatures and frequencies, and then used three different prediction models including the Coffin-Manson model, Smith-Topper model, and Morrow model. Lau, et al. [107] investigated the thermal cycling fatigue life of lead-free solder joints in a plastic ball grid array (PBGA) package assembly. They concluded that the thermal-fatigue life of the solder joints would be over-estimated based on a pure shear theory. In addition to pure shear, bending, twisting and expansion/contraction deformations were needed to be included. Pang, et al. [95] investigated isothermal low cycle fatigue for 95.5Sn-3.8Ag-0.7Cu bulk solder specimens over a range of test temperatures (-40, 25, 75 and 125 °C) and frequencies (1Hz, 0.01 Hz and 0.001 Hz). They proposed frequency modified Coffin-Manson model and Morrow model relationships for 95.5Sn-3.8Ag-0.7Cu lead free solder at 125 °C and over the entire range of test frequencies.

2.7 Effects of Thermomechanical Cycling on Solder Properties

The effects of mechanical cycling on the microstructure of eutectic Sn-Pb and Lead free solder joints have been explored by several researchers. Chen, et al. [108] studied the microstructure evolution of Sn-Ag-based solder interconnects during thermal cycling.

They noted during the cycling, recrystallization was observed and Ag_3Sn IMC particles segregated in those regions. Berthou, et al. [109] investigated microstructure of SAC joints when subjected to thermal cycling and thermal loading, and stated that huge stresses were developed in areas where tin grain recrystallization occurred. This resulted in the joints failing by thermomechanical cycling fatigue. During thermal cycling, Yin and coauthors [110] noticed that recrystallization of β-Sn phases occurred, and there was coarsening of precipitates in the solder joints. Coarsening of the IMC particles during cycling has also been observed by other researchers [111-113]. Thermal cycling has also been found to induce significant changes in the mechanical properties of SAC solders due to damage accumulation [111-117]. Changes in elastic modulus [114], hardness [115], reliability [116], creep behavior [111-112], and constitutive response [117] have been reported.

Matin, et al. [118-119] studied the effects of both mechanical and thermal loadings on SAC solder joints using Optical Microscopy (OM) and Scanning Electron Microscopy (SEM). It was observed that for thermal loads, damage propagated through the grain boundaries, while for the pure mechanical load, the damage was seen to have occurred between slip bands and eutectic regions in the form of micro-cracks and voids. Many researchers have also investigated the evolution of mechanical properties of solder joint materials under thermal cycling or mechanical cycling conditions. Chen, et al. [108] reported that the hardness of SAC305 decreased by about 39% and 20%, respectively, in the recrystallized and non-recrystallized regions after 2815 thermal cycles between 0 °C and 100 °C. Dutta and coworkers [111-112] studied the effects of TMC induced microstructural coarsening on the creep behavior of lead free solders. They reported that the creep rate increases with the precipitate size proportionately when the stresses are low.

On the other hand, precipitate coarsening changes the threshold stress for particle-limited creep when the stresses are high. Erinc, et al. [114] found the global elastic modulus was dropping for the three SAC405 samples of different thickness as the thermal cycling progressed (-40 °C to 125 °C). Furthermore, a significant reduction in board-level drop reliability with increased thermal cycling was reported in [116].

2.8 Effects of Aging on the Microstructure of Solder

Due to their low melting temperatures, solders are exposed to high homologous temperatures in most product applications. Thus, there is a continuous state of active diffusion processes in the solder alloys, and their microstructures are inherently unstable and will continually evolve during normal operating temperature conditions of electronic packaging assemblies. High temperature storage, which is also known as isothermal aging, of the solder alloys causes a significant change in the microstructure leading to a degradation of mechanical properties. In recent days, electronic industries are moving towards lead free solders due to the growing concern about environment. Effect of aging in lead free solder is even more significant. Sahaym et al. [120] examined the evolution of microstructure of bulk SAC105 and SAC305 solder during isothermal aging at 150 ºC. They observed the changes of identical region after 4 different aging durations (0 hr., 110 hr., 194 hr., and 310 hr.). They reported that after 310 hours of aging, the average size of IMC precipitates has increased from 0.35 μm to 2.5 μm and the average grain size has increase from 4.5 μm to 7.5 μm. The authors also observed that a small percentage (~10%) of β-Sn grains, especially those near the eutectic region, has went through recrystallization during isothermal aging. They claimed the stress on the β-Sn grains, due to the growth of

IMC particle, is responsible for the recrystallization. The extent of recrystallization was less in SAC105 than in SAC305 due to the relative difference in IMC volume fraction.

Maleki et al. [121] studied the evolution of microstructure of SAC405 and pure Sn during isothermal aging at 150 ºC after 144 hours and 296 hours. They also performed Mechanical testing (shear test) to correlate changes in microstructure and mechanical properties. Sample size was approximately 1 × 0.3 × 0.3 mm and it was attached to Cu-pad. They reported that in as-reflowed condition, the microstructure of SAC405 was consisted of ~70 vol% of eutectic phase and ~30 vol% of β-Sn dendrite, whereas the mean diameter of IMC particles and interparticle distance was ~250 nm and ~630 nm, respectively. Average particle size increases with aging time due to Ostwald ripening. During IMC growth, they attributed bulk diffusion to be the main rate controlling mechanism. On the other hand, aspect ratio decreases and interparticle spacing increases with aging due to the driving force to reduce surface energy. Electron backscatter diffraction (EBSD) analysis confirmed the presence of large grains (~200 µm) in SAC405 solder before aging. After 296 hours of aging at 150 ºC they didn’t find any significant change in grain size and orientation. On the other hand, pure tin has a fine grain (~10 µm) microstructure before aging which grows significantly during aging and become ~200 µm after aging. They attributed the reduction of mechanical properties during aging for SAC 405 to the IMC’s coarsening whereas for pure Sn to the grain coarsening.

Telang et al. [122] worked on the effects of aging at 150 ºC on microstructure, especially grain size and grain-boundary misorientation, of several alloys including Pure Sn (ingot and reflowed), Eutectic Sn-3.5Ag (ingot), Eutectic Sn-3.8Ag-0.7Cu (ingot), Sn-1.6Ag (solder ball), Sn-3.0Ag (solder ball), and Sn-3.0Ag-0.6Cu (solder ball). For Sn-

3.5Ag alloy they studied three different aging conditions (i.e. 0, 200, and 400 hours.) whereas for rest of the alloys they studied two different aging conditions (i.e. 0. and 200 hours). Before aging, grain size of pure Sn ingot and Reflowed Pure Sn was 50-150 μm (equiaxed) and 100-250 μm (equiaxed), respectively. After aging for 200 hours, the grain size of pure Sn for both condition was >500 μm with irregular shape. After comparing the microstructure of eutectic Sn-Ag (3.5% Ag) ingot with pure Sn ingot, they found that Sn-Ag alloy has a much finer (10-30 μm) grain size, which was very stable. Aging of Ag-Sn alloy did not cause any significant grain growth due to the pinning effect of Ag_3Sn IMC particles. On the other hand, the grain size of SAC (Sn-3.8Ag-0.7Cu) ingot was similar to that of Sn-Ag ingot (10-30 μm). But, aging for 200 hours caused a significant growth in the grain size (~120 μm) of the alloy. From their experimental observations the authors also have discussed the effect of Ag and Cu on preferred grain orientation and grain size.

Allen et al. [123] studied two near eutectic lead free SAC solders (bulk Sn-3.5Ag-0.9Cu and SAC405 joint). They used 3 different aging temperatures (152, 177, and 201 °C) and 5 different aging durations (0, 1, 2, 4, and 8 weeks). They measured the density of IMC particle after different aging conditions and based on their experimental results they conclude that the rate controlling mechanism for coarsening is volume diffusion (n=3). They also reported that the coarsening kinetics of eutectic SAC solder is slower than that of eutectic Sn-Pb solders. Kumar et al. [124] worked with SAC105 and SAC305 alloys. For isothermal aging experiments, they polished a bulk reflowed solder samples and then aged the samples at 150 °C in high vacuum (to prevent oxidation). After different aging intervals (i.e. 0, 110, 194, 220, and 330 hours) they captured the SEM image of the same region, of any particular sample, to quantify the coarsening behavior of the IMC's. They found that the growth rate of Cu_6Sn_5 particles are much faster than Ag_3Sn particles, due to the higher diffusivity of Cu than Ag in Sn matrix. Besides, the fraction of Ag_3Sn particles was significantly higher than Cu_6Sn_5 particles. Hence, they decided to focus their study on the coarsening of Ag_3Sn particles only. They predicted coarsening rate of Ag_3Sn particles, during isothermal aging, and then compared with the experimental observations. They conclude that the model could efficiently measure thermomechanical history during isothermal aging and thermomechanical cycling (TMC) below 200 cycles. After 200 cycles the IMC particles undergo dissolution and re-precipitation/redistribution which can't be captured properly by this model. In addition to coarsening, during isothermal aging, they also had observed recrystallization near the eutectic region. They explained that the growth of IMC particles might play an important role in recrystallization.

Besides bulk solder samples, researchers have also explored the effect of aging on the actual solder joints. Chauhan et al. [125] monitored the effect of isothermal aging at 100 °C on phase coarsening and evolution of SAC305 solder joint. They used image processing software to quantify size, interparticle spacing and volume fraction of Ag_3Sn and Cu_6Sn_5 IMC's. Impact of these changes on secondary creep response was modeled using multiscale creep model. The authors performed their experiments in 4 different aging conditions (0, 24, 600, and 1000 hours.) and presented average results of 3 samples (solder joint) for each aging condition. They found that the size of Ag_3Sn increases monotonically with increasing aging time whereas the size of Cu_6Sn_5 decreased after 600 hours of aging. They didn't find any significant change in Sn grain morphology after 1000 hours (41 days) of aging.

Yang et al. [126] prepared solder joints using 2 different soldering methods (laser and infrared soldering) and captured the evolution of microstructure during aging up to 190 ^{o}C for times up to 300 days. They reported that the evolution is consisted of the growth of IMC's and the Cu-Sn layer near the interface. Although they had studied two different initial microstructure, obtained from 2 different soldering methods, aging at 190 ^{o}C caused the final microstructures to be the same. Chiu et al. [127] examined the effect of aging time and temperature on the board level reliability during the drop test of lead free SAC solder joints. They reported that kirkendall void formation, at the interface of Cu pad and Cu_3Sn IMC, is the main reason for getting lower drop reliability during drop test. Fix et al. [128] explored the effect of aging time (0 to 1000 hours) and temperatures (125 to 175 ^{o}C) on the microstructure of SAC405 solder joint. They have confirmed a significant growth of Ag_3Sn and Cu_6Sn_5 IMCs with aging time. The authors modeled phase growth based on Ostwald ripening mechanism. They conclude that a growth exponent $n = 3$, which indicated volume diffusion as the growth rate controlling mechanism, matches very well with the experimental growth rate data. The effect of aging at 150 ^{o}C on the evolution of eutectic Sn-Ag solder joint for up to 800 hours was studied by Ahat et al. [129]. From experimental results, they conclude that the thickness of IMC layer increases linearly with square root of aging time. Choi et al. [130] investigated the effect of different soldering and aging time on the interface layer of Sn-3.5Ag solder and Cu substrate. They used the same solder joint to age at 130 ^{o}C for different time duration up to 800 hours They found that thickness of IMC layer continue to grow with increasing aging duration. However, the growth behavior of IMC layer during aging strongly depends on the initial morphology and hence on the soldering time.

Akhtar et al. [131] studied the evolution of microstructure near the interface of a solder joint during isothermal aging at 150 ºC, for four different aging duration (0, 250, 500, and 1000 hours). They used SAC305 solder joint (ball diameter 500 μm) with two different surface finish (Immersion Gold (ImAu) and Immersion Tin (Sn)). Image analysis software ImageJ was used to measure the thickness of the IMC layer. They also calculated the activation energy based on the measured thickness data. They found that the thickness of the IMC layer increases with increasing aging time. Besides, the morphology of the IMC layer, for both surface finishes, change from scallop type to layer type after the aging treatment. Based on their calculations they found that the activation energy of SAC305/ImSn system was less than SAC305/ImAu system resulting a higher IMC layer growth rate in SAC305/ImSn system.

A comparative study was performed by Berthou et al. [132] where the authors compared the failure mechanism of BGA packages with SAC305 solder joints subjected to two different conditions: (a) accelerated thermal cycling (ATC) between -55 to 125 ºC and (b) thermal storage at 80, 125, and 150 ºC for 1000 hours. During ATC, they found recrystallization of big Sn grains to small grains in the regions of high stress accumulation. Cracks initiates and grows at interface of the new recrystallized grains. On the other hand, thermal storage for 1000 hours caused a significant growth of IMC layer near the interface as well as the IMCs in the bulk. They didn’t reported any recrystallization after thermal storage.

2.9 Summary

In this chapter, the existing literature on the effects of aging on the mechanical properties and the microstructure of lead free solder was extensively discussed. The mechanical properties of a solder are strongly influenced by its microstructure, which is controlled by its thermal history including its solidification rate and thermal exposures after solidification. Aging of lead free solders leads to degradations in their constitutive and failure behaviors. For example, research in the literature has shown that aging leads to large reductions in solder material properties including shear strength, elastic modulus, nanoindentation joint modulus and hardness, high strain rate mechanical behavior, creep response, and Anand model parameters. Other studies have shown that aging causes severe degradations in uniaxial cyclic stress-strain curves and fatigue life, shear cyclic stress-strain curves and fatigue life, fracture behavior, drop reliability, and thermal cycling reliability.

Dopants have been found to strongly influence the properties and behaviors of lead free solders. For Example, Bi helps to reduce solidification temperature, increases strength by means of precipitation hardening, helps to reduce IMC (Intermetallic Compound) layer thickness, and also reduce aging induced degradation of mechanical properties in lead free solder materials. Ni helps to improve thermal fatigue life and drop test performance by refining Sn grain size and reducing the IMC layer formation near the Cu pad.

Previous studies on cyclic stress-strain behavior of solder alloys were also discussed. Several experimental investigations, and developed theories for cyclic stress strain behavior of different solder alloys were presented for various testing conditions. Studies on the dependence of hysteresis loop shape and size for different frequencies and testing temperatures were also discussed. It has been demonstrated that the area of the hysteresis loop decreases with increasing frequency of cyclic loading, whereas the area of the hysteresis loop decreases with the increasing testing temperature. It is also reported in the literature that with increasing strain range, the area of the hysteresis loop increases. Several attempts have also been made to establish a correlation between isothermal mechanical loading hysteresis loops and thermal cycling hysteresis loops for lead free solders.

Lastly, evolution of microstructure and mechanical properties of solder materials subjected to cyclic loading were discussed. Several fatigue life prediction models such as, the Coffin-Manson model, Smith-Topper model, and Morrow model have been used by researchers. Fatigue tests have been performed for the solder alloys under strain controlled uniaxial, shear, and torsional loadings. Nucleation and growth mechanisms of fatigue damage were also observed using optical microscopy, scanning electron microscopy (SEM), and the Electron Back-Scattering Diffraction (EBSD) method. Finally, a short discussion of the literature regarding aging effects on fatigue behavior for solder materials has been presented. The changes in solder mechanical behavior are a result of the evolution of the SAC solder microstructure that occurs during aging. The most well-known and widely observed changes are coarsening of the Ag_3Sn and Cu_6Sn_5 intermetallic compounds (IMCs) present in the eutectic regions between beta-Sn dendrites. Several researchers have proposed empirical models to describe the growth of these secondary phase particles as a function of aging temperature and aging time, and related this growth to mechanical property changes.

CHAPTER 3

EXPERIMENTAL PROCEDURE

3.1 Introduction

The specimen preparation and testing techniques are presented in this chapter. The mechanical characterization of solder alloy is typically performed by uniaxial loading of machined or mold cast samples, or by shear loading of joint samples. In some parts of this study, mold cast samples using some high precision rectangular cross-section glass tubes have been tested under uniaxial loading to characterize mechanically. However, the thin flat specimens tend to buckle during compression in fatigue testing. In order to prevent buckling, the circular cross-section specimens were also introduced, and fixtures were designed to grip the cylindrical specimens. In last part of this study, solder joints samples were also used to characterize the Pb-Free solder joint material. The mechanical testing was performed using a tension/torsion thermo-mechanical test system. After testing, empirical models were utilized to represent the stress-strain, creep, and cyclic stress-strain experimental data. For the microstructural analysis, the rectangular cross-sectional solder specimens were polished and then the microstructures were examined using SEM or polarized light microscope.

3.2 Uniaxial Test Sample Preparation

Initially, bulk solder material was cut into pieces by a shear cutter machine. Then the small pieces were melted in a quartz crucible using circular heating elements (Figure 3.1), which is controlled by a digital controller using the feedback from a thermocouple attached on the crucible. Using vacuum suction process, uniaxial test specimens of lead free solder alloy were formed with controlled microstructure in glass tubes. The melted solder material was sucked into the glass tube by inserting one end into the molten solder in the crucible and then applying suction to the other end using a rubber tube connected to a vacuum suction pump. A manually controlled regulator on the vacuum line regulates the amount of solder drawn into the tube. When the tube contains the desired amount of solder, it was solidified through quenching in a water bath at room temperature.

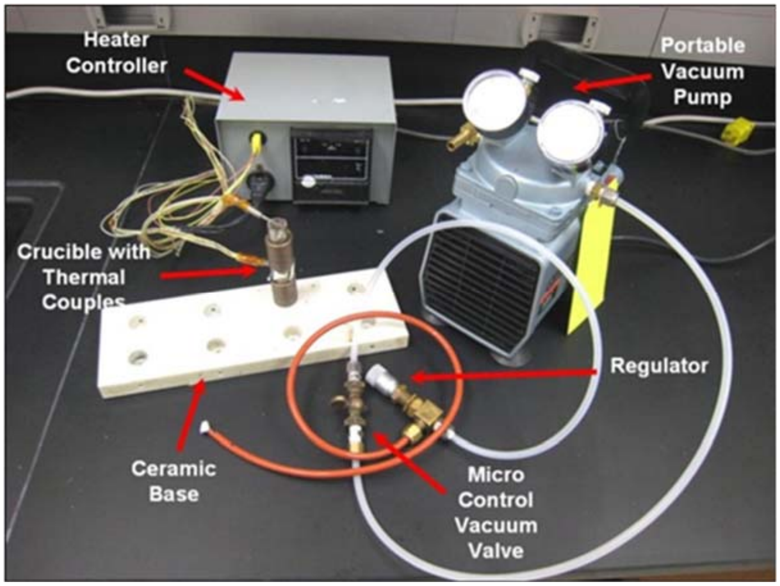

Figure 3.1 Equipment used for Specimen Preparation

After that, the tensile specimens were prepared using two different solidification profiles.

1) Water quenched (WQ) solidification profile, leading to fine microstructures and the upper limits of the mechanical properties for each alloy.
2) Reflowed (RF) solidification profile, leading to a coarse microstructure very similar to an actual solder joints. The solder test specimens were passed through a controlled heating and cooling chamber using a SMT (surface mount technology) reflow oven.

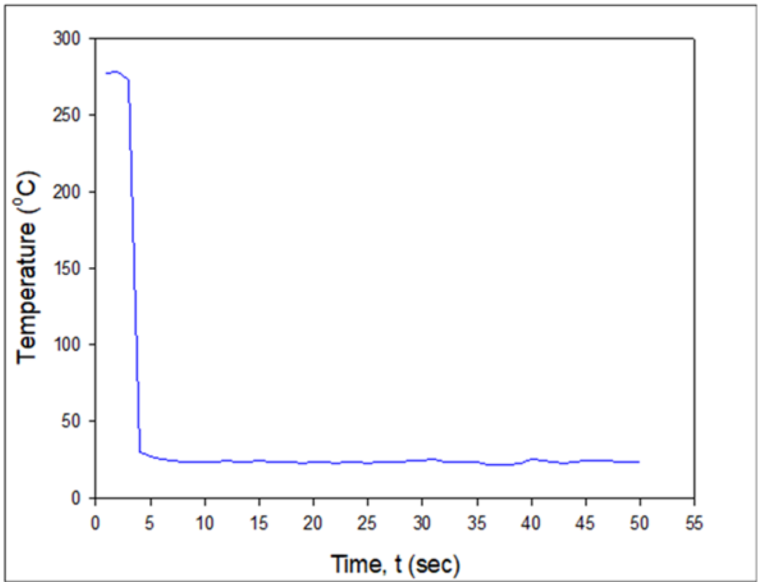

Figure 3.2 Water Quenched (WQ) Cooling Profiles

The temperature vs. time variations for the WQ profile is shown in Figure 3.2. For the samples with reflowed profile, test specimens were initially prepared using WQ profile and then the samples within the glass tubes were sent through a 9 zone Heller 1800EXL reflow oven (Figure 3.3).

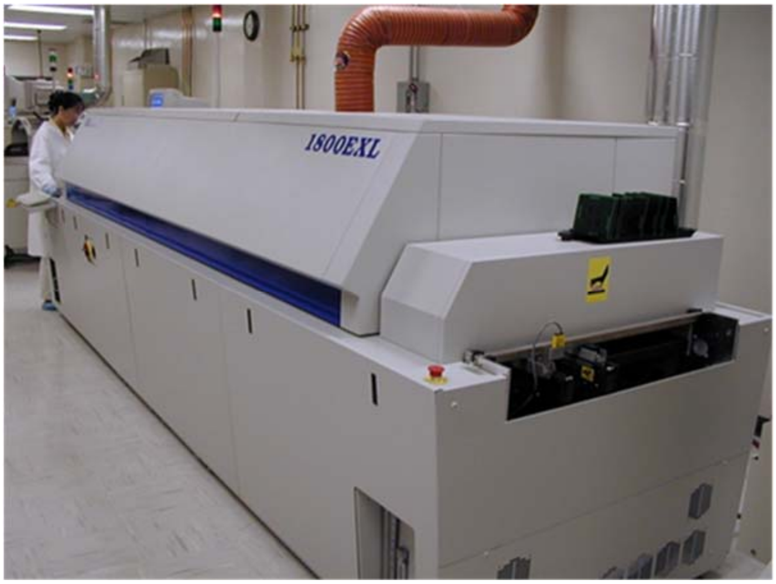

Figure 3.3 Heller 1800EXL Reflow Oven

Inside the oven, solder samples were re-melted and experienced to a pre-set temperature profile which is very similar to that used for the actual solder joints. The reflow temperature profile used in this study is presented in Figure 3.4.

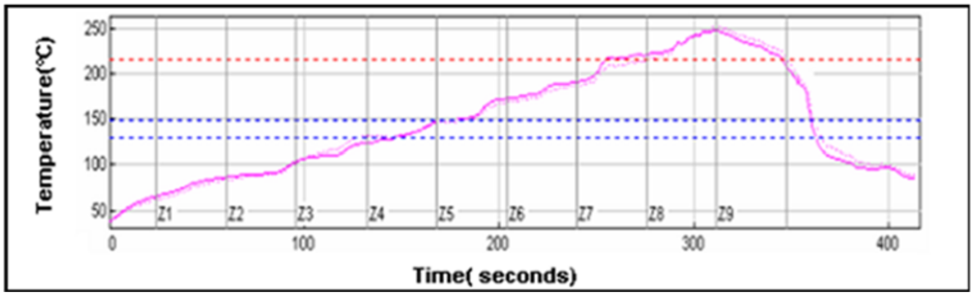

Figure 3.4 Reflow (RF) Cooling Profiles

A typical glass tubes filled with solder and final solder samples after extraction from the glass tubes are shown in Figure 3.5. Glass has lower coefficient of thermal expansion (CTE) compared to solder. As a result, for some solder alloy and cooling rate combinations, solidified solder samples were easily pulled out from the glass tube due to the difference is the CTE of glass and solder. Another way followed to extract the solder sample from the glass tube is by carefully breaking the glass. The tubes in this work had a length of 120 mm, and a cross-sectional area of 3.0 x 0.5 mm. A thickness of 0.5 mm was chosen since it matches the height of typical BGA solder joints. The nominal dimensions of the final test samples were 80 x 3 x 0.5 mm. The specimens were stored in a low temperature freezer after the water quenched/reflow process to minimize any aging effects. The solder microstructure has been verified to be consistent throughout a specimen volume, and from specimen to specimen by cross-sectioning. A micro-focus x-ray system was used to inspect the samples for the presence of flaws (e.g. notches and external indentations) and/or internal voids (non-visible). Specimens with no flaws and voids were generated using proper experimental techniques, and Figure 3.6 illustrates x-rays scans for good and poor specimens.


(a) Within Glass Tubes


(b) After Extraction

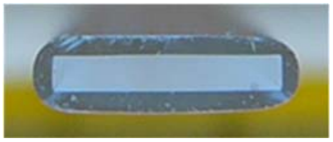
(c) Cross-Section

Figure 3.5 Solder Uniaxial Test Specimens

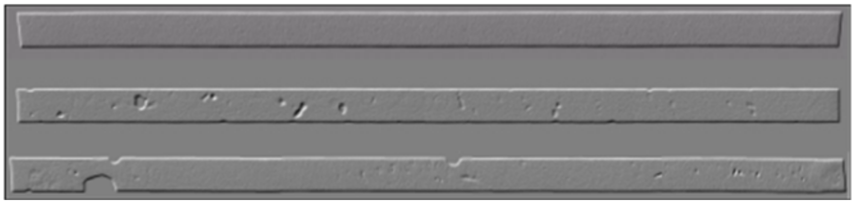

Figure 3.6 X-Ray Inspection of Solder Test Specimens (Good and Bad Samples)

3.3 Uniaxial Tensile Testing System

The tension/torsion thermo-mechanical test system (Wisdom Technology MT-200) used to perform the stress-strain tests in this study is presented in Figure 3.7. This instrument is optimized for loading small specimens such as thin films, solder joints, gold wire, fibers, etc. It provides an axial displacement resolution of 0.1 micron. Samples can be tested over a temperature range of -185 to +300 °C using supplemental environmental chambers added to the system.

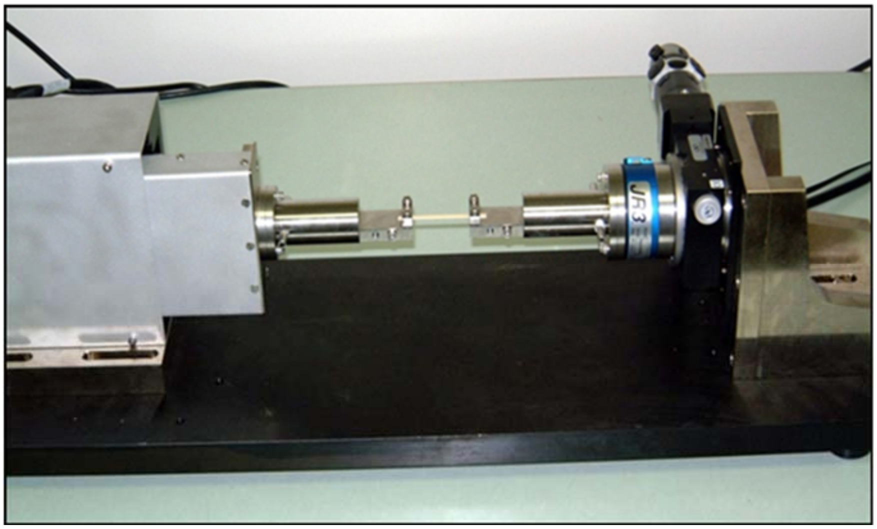

Figure 3.7 Mechanical Test System with Uniaxial Sample

Forces and displacements were measured in the uniaxial tests, and the axial stress and axial strain were calculated using

$$\sigma = \frac{F}{A} \qquad \varepsilon = \frac{\Delta L}{L} = \frac{\delta}{L} \tag{3.1}$$

Where, F is the measured uniaxial force, δ is the measured crosshead displacement, σ is the uniaxial stress, ε is the uniaxial strain, A is the original cross-sectional area, and L is the chosen specimen gage length (initial length between the grips). In order to ensure a uniaxial stress state, the gage length of the specimen was kept as 60 mm (thus the length to width ratio was 20 to 1).

3.4 Typical Stress-Strain Data Processing

A typical SAC solder tensile stress strain curve is illustrated in Figure 3.8. The standard material properties are labelled on the graph including the effective elastic modulus E (initial slope of the stress-strain curve). This effective modulus is rate dependent since solder behavior is viscoplastic. The value of the effective modulus will become the true elastic modulus as the testing speed is increased to the limit of infinite strain rate. The yield stress σ_Y (YS) is defined using the typical definition of the stress level that results in a permanent strain of $\varepsilon = .002 = 0.2\%$ upon unloading. The maximum (saturation) stress on the stress-strain curve is the ultimate tensile strength σ_u (UTS). As shown the figure, the stress-strain curve for the solder material has an elastic region at the beginning, a small transition region followed by a plastic region. As the strain becomes significantly high, localized deformation takes place which is also known as necking. Necking causes a visible reduction in cross-sectional area and a drop in the applied load, near the end of the stress strain curve, leading towards a rupture.

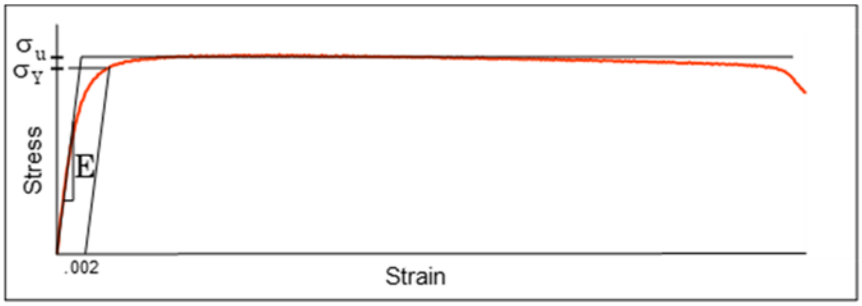

Figure 3.8 SAC Stress-Strain Curve and Material Properties

Figure 3.9 illustrates a typical set of 5 solder stress strain curves measured for the same alloy under similar environmental and aging conditions. In this work, a four parameter hyperbolic tangent empirical model has been used to represent the “average” stress-strain curve through a set of experimental data (red curve in Figure 3.9). Material constants C_1, C_2, C_3, and C_4 are determined through regression fitting of the model to experimental data (Equation 3.2). The effective elastic modulus E at zero strain is calculated from the model constants using Equation 3.3.

$$\sigma = C_1 \tanh(C_2\varepsilon) + C_3 \tanh(C_4\varepsilon) \tag{3.2}$$

$$E = \sigma'(0) = C_1C_2 + C_3C_4 \tag{3.3}$$

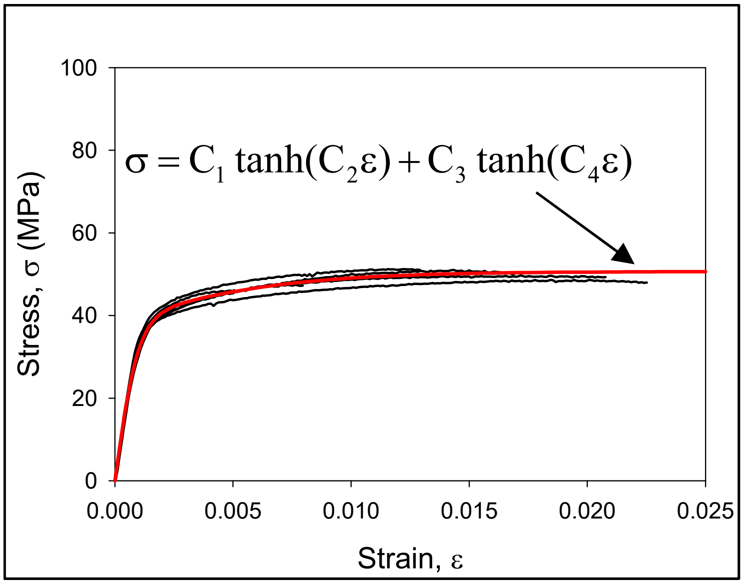

Figure 3.9 Empirical Model Fit to Solder Stress-Strain Curves

3.5 Sample Preparation for Cyclic Stress-Strain Test

For cyclic stress-strain testing, unlike prior studies that used rectangular cross-section glass tubes, glass tubes with circular cross-sections were adopted in this part to produce cylindrical specimens that are more resistant to buckling during the compression portions of cyclic stress-strain testing. Buckling is the bending of a slender element when subjected to compression, which leads to a sideway deflection. If buckling occurs during fatigue testing, it can be told from the test sample, corresponding hysteresis loop and cycles to failure. The resistance to buckling can be significantly improved by using the cylindrical specimens in proper size. Cylindrical glass tubes of inner diameter 1.2 mm were used in this case. For cyclic stress-strain tests, specimens were formed in circular cross-section glass tubes using the same vacuum suction process as shown in Figure 3.1. The reflow profile was chosen to closely mimic profiles used for BGA assemblies, so that the obtained microstructures were similar to those found in typical solder joints. Typical cylindrical glass tube assembly filled with solder and a final extracted specimen are shown in Figure 3.10. The samples were initially cooled in a water bath and were later reflowed.

(a) Solder specimen in glass tube

(b) Final specimen after reflow and extraction

Figure 3.10 Cylindrical solder test specimen

3.6 Cyclic Stress-Strain Testing

The universal micro-tension/torsion thermo-mechanical (Wisdom Technology MT-200) testing machine shown in Figure 3.7 was used to perform the cyclic testing in this work. Figure 3.11 shows the utilized specimen grips that contained V-shaped grooves that clamped the ends of the samples. A gage length of 5 mm was used for the tests, and the displacements could be controlled to a resolution of 0.1 micron. The samples were mechanically cycled at room temperature (T = 25 °C) under strain control. For SAC305, a total strain range of $\varepsilon = \pm 0.01$ was used per cycle, while for SAC_Q, a total strain range of $\varepsilon = \pm 0.005$ was used per cycle. In both cases, a strain rate of $\dot{\varepsilon} = 0.002 \text{ sec}^{-1}$ was utilized.

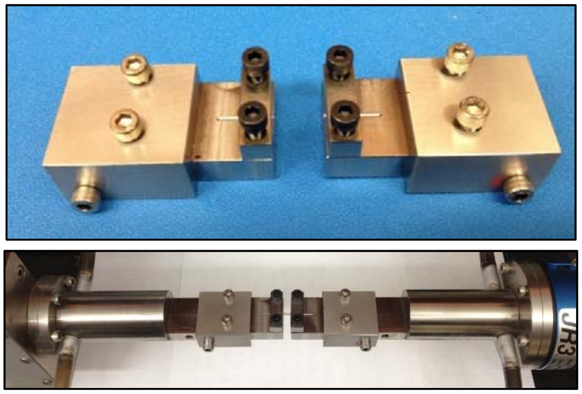

Figure 3.11 Fixtures with V-grooves used to grip the samples.

3.7 Cyclic Stress-Strain Data Processing

Typical measured cyclic shear stress–strain curves and hysteresis loops for a doped SAC solder specimen are shown in Figure 3.12. In this case, all samples were tested under strain controlled cycling with strain limits of ±0.005. Initially, a tensile loading was applied starting from a relaxed point (point A). Then, the loading was gradually increasing at a strain rate of 10^{-3} to generate the initial portion of the stress-strain curve until the strain reached +0.005 (point B). At that time, the direction of crosshead motion was reversed and the sample was then compressed until the strain reached -0.005 (point C). Again, the direction of loading was reversed and testing continued in tension until the strain again reached +0.005 (point B). Hence, the first hysteresis loop was ended. Further loops (between points B and C) were created by continuing the alternating tensile and compressive loadings in a similar fashion.

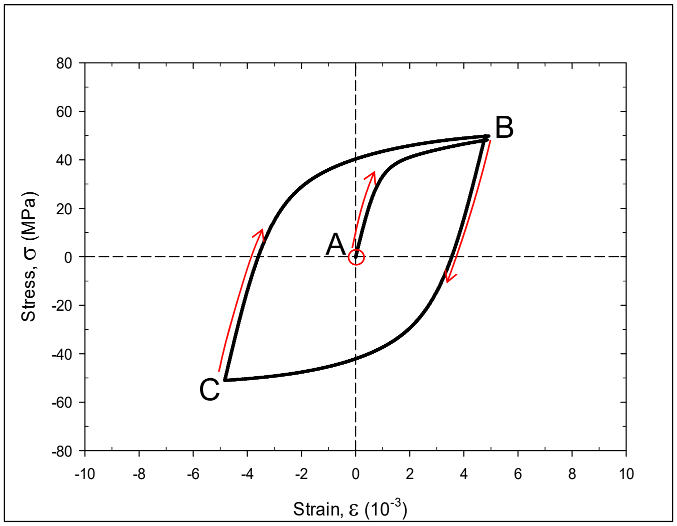

Figure 3.12 Typical Cyclic Stress-Strain Results for bulk samples (Strain Controlled)

A 4-parameter hyperbolic tangent model was used to process the cyclic stress-strain data. Two different equations of this hyperbolic tangent model were used to represent the tension portion (C to B, top) and the compression portion (B to C, bottom) of the stress-strain behavior in each cycle.

$$f_1(\varepsilon) = -A_1 \tanh(A_2(-\varepsilon+\varepsilon_2)) - A_3 \tanh(A_4(-\varepsilon+\varepsilon_2)) + \sigma_1 \tag{3.4}$$

$$f_2(\varepsilon) = B_1 \tanh(B_2(\varepsilon-\varepsilon_1)) + B_3 \tanh(B_4(\varepsilon-\varepsilon_1)) + \sigma_2 \tag{3.5}$$

$$\varepsilon_1 \le \varepsilon \le \varepsilon_2$$

Where the empirical fits $f_1(\varepsilon)$ for the compression loading region (bottom of the hysteresis loop) and $f_2(\varepsilon)$ for the tensile region (top of the hysteresis loop). From the stress-strain data for each cycle, the constants in the empirical models of eq. (3.4) and (3.5) can be determined through a nonlinear regression analysis. The associated hysteresis loop area can then be calculated using the eq. (3.6).

$$\Delta W = \int_{\varepsilon_1}^{\varepsilon_2} \left[f_2(\varepsilon) - f_1(\varepsilon) \right] \, d\varepsilon \tag{3.6}$$

This area represents the energy density dissipated per cycle during the cyclic loading.

From the recorded cyclic stress-strain curves, the areas of the hysteresis loops are calculated using the procedure outlined above. In addition, the plastic strain ranges and peak stresses are determined as illustrated in Figure 3.13. The plastic strain range is equal to the total strain range minus the elastic strain range, which is the distance between the two strain axis intercepts on the graph. The peak stress is simply the maximum stress recorded during the cycle. The hysteresis loop area and plastic strain range are usually considered as fatigue damage driving forces, and are widely used in models to predict fatigue life of solders.

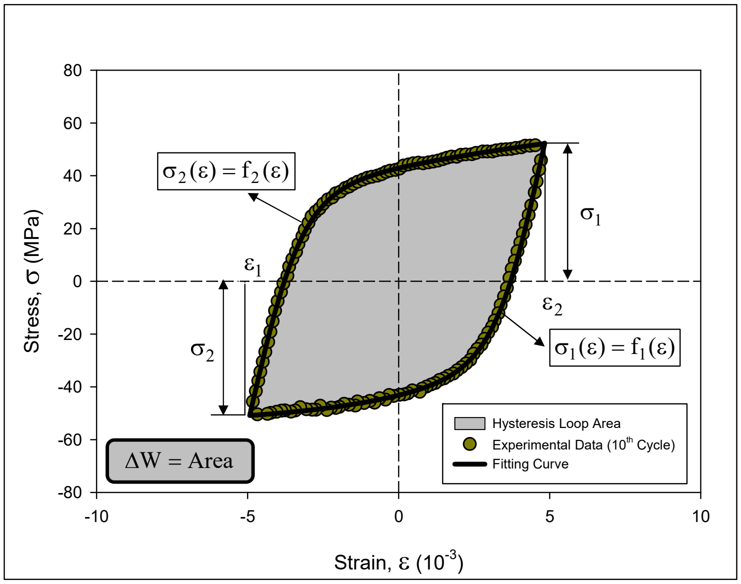

Figure 3.13 Cyclic stress-strain curve and hysteresis loop for a SAC solder.

To study the effects of cycling on damage accumulation and degradation of the constitutive behavior of SAC305 and SAC_Q, uniaxial samples have been prepared and subjected to various durations of prior isothermal mechanical cycling (e.g. 0, 50, 100, 300, 600, 900, 1200 cycles) that were below the fatigue life of the material. These various amounts of prior cycling served to impart various levels of fatigue damage to the samples. The same strain ranges of $\varepsilon = \pm 0.01$ and $\varepsilon = \pm 0.005$ were used for SAC305 and SAC_Q, respectively. After cycling (damage accumulation), the specimens were subjected to stress-strain or creep testing.

3.8 Microstructure Study

For microstructure analysis, the fabricated solder samples were cut into small pieces and potted in epoxy. Details of the preparation process included mechanical grinding with several SiC papers (#320 to #400, #600, #800 and #1200) in a rotating metallographic disc as shown in Figure 3.14. The final polishing was conducted with 0.02 μm colloidal silica suspensions where BUEHLER MasterMet 2 was the abrasive solution and BUEHLER ChemoMet was the polishing cloth. This procedure resulted in mirror finish samples suitable for optical microscopy, Scanning Electron Microscopy (SEM), as well as nanoindentation. Microstructure analysis of the solder alloys was performed on the mounted and polished testing coupons by using an OLYMPUS BX60 Optical Microscope (Figure 3.15), and a JEOL JSM 7000F Field Emission SEM (Figure 3.16). In addition, EDS (Energy-Dispersive X-ray Spectroscopy) was employed to explore the chemical composition of different phases in the microstructure.

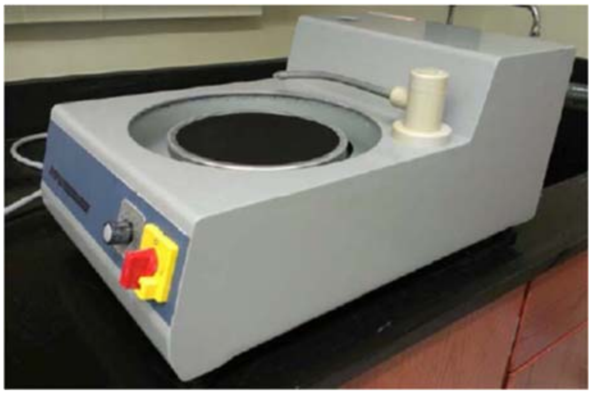

Figure 3.14 Grinding and Polishing Machine

Figure 3.15 OLYMPUS BX60 Optical Microscope

Figure 3.16 JEOL JSM-7000F Field Emission SEM

To observe microstructural evolution due to both mechanical cycling and aging, special rectangular cross-section uniaxial test specimens were prepared and polished. The vacuum suction approach discussed above was again utilized with glass tubes with rectangular cross-sections, and the final specimen dimensions were 30 x 3 x 0.5 mm. After preparation, but prior to cycling, the solder specimens were mounted on a cylindrical epoxy preform by reversible tape to facilitate polishing. In this way, the tested SAC305 solder cross-sectional samples were polished but not encapsulated in microscopy potting compound. The sample polishing process included mechanical grinding with several SiC papers (#400, #600, #800 and #1200), and then final polishing with 0.02 μm colloidal silica suspensions. The prepared samples were then placed within the nanoindentation system (Figure 3.17), and several fixed square regions with dimensions of approximately 90 x 90 μm were then selected in the polished region of each sample for subsequent SEM observations. To locate and track the selected fixed regions, they were demarcated using four nanoindentation marks placed at their corners using a Hysitron TI 950 nanoindentation system as shown in Figure 3.18. After polishing and applying the nanoindentation marks, the specimens were carefully removed from the temporary carriers. The indentation marks were positioned close enough to enable region identification, but far enough away from the region to avoid influencing the microstructure evolution. Lastly, a field emission SEM was used to study the changes of solder microstructure caused by both fatigue cycling and aging.

Figure 3.17 Hysitron TI950 TriboIndenter

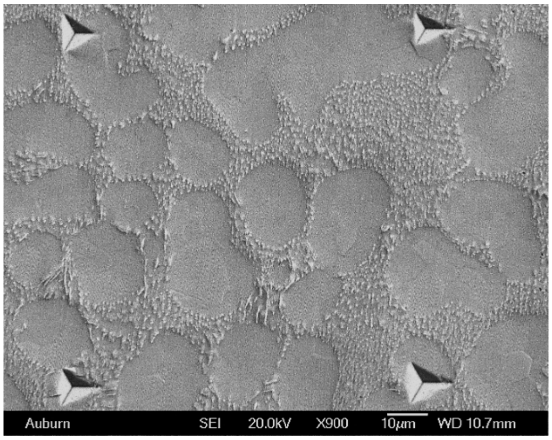

Figure 3.18 - Typical Fixed Region with Indentation Marks

3.9 Sample Preparation for Nanoindentation

For this study, SAC305 (96.5Sn-3.0Ag-0.5Cu) and SAC_Q (92.7Sn-3.4Ag-0.5Cu-3.3Bi) lead free solder joints were tested. The joints had a diameter of about 30mils (762 µm). Figure 3.19 shows an example of the test joints used for the experiments. The samples consisted of a 3 x 3 Ball Grid Array (BGA) of the lead free alloys to be tested. The substrates used in the specimens were FR-4 PCBs. Samples which had an Immersion Silver (ImAg) surface finish on the copper pads were chosen. Flux was deposited on the pads using a stencil. A reflow profile with a maximum temperature of 245 °C was obtained with the help of a Vitonics-Soltec convection oven. The profile also ensured that the assembly was kept above the liquidus temperature for about 45-60 seconds. The samples were then cleaned, dried and stored in a freezer at -40 °C to hinder any aging effects.

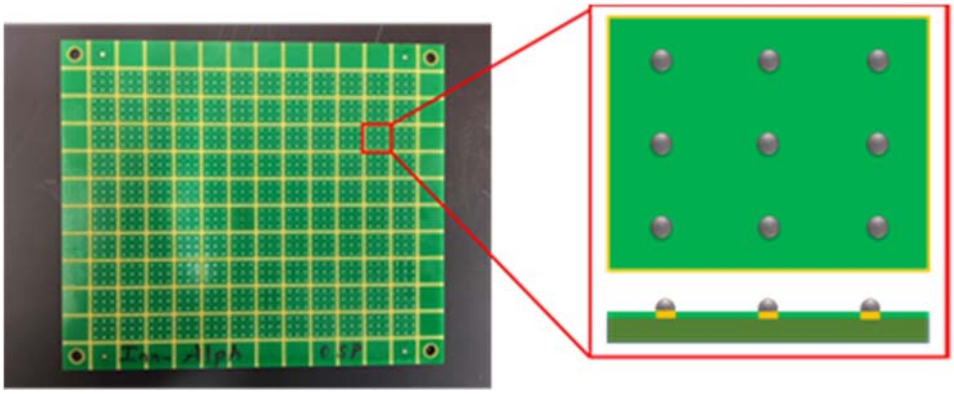

Figure 3.19 3x3 BGA Specimen Sample

Samples were covered with a tape and then confined in epoxy resin. The tape was used to prevent epoxy from entering the space between the individual joints which allows the cycling of each joint separately. The tape from these samples were removed by coarse grinding using a 320 grit SiC paper. Grinding papers up to 1200 grit were then used to reduce the scratches on the samples. The samples were then finally polished a 0.02 µm colloidal silica suspension to flatten the top surface of the solder joints and making the joints suitable for nanoindentation tests. All the polished joints were viewed under a Polarized Light Microscope to verify that all experiments were conducted on single grain joints. The Micromechanical Tester shown in Figure 3.20 was used to cycle the individual solder joint. The cyclic shear loading was conducted with a peak load of 600 gf (equivalent to a stress of about 24MPa). The joints were individually cycled in the shear direction for various durations of 50, 100, 150, 200 and 300 cycles. After every selected cyclic condition, the sample was removed and the degradation in Elastic Modulus, Hardness and Creep Strain Rate of each joint was characterized using the nanoindentation machine.

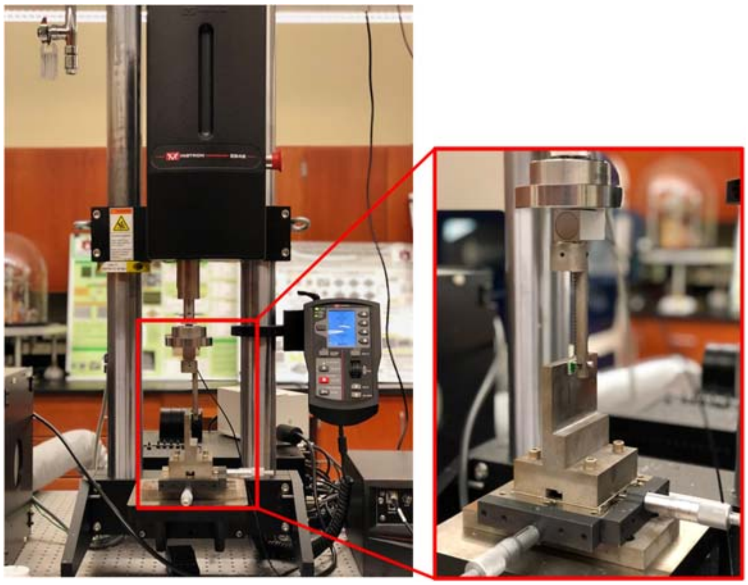

Figure 3.20 Micromechanical Tester used for the Mechanical Cycling Tests

3.10 Nanoindentation Machine and Test Procedures

The nanoindentation machine utilized a probe with a Berkovich geometric tip to record the changes in load against indentation displacement. The recorded data was measured in the direction normal to the polished face. At least 5 indents were made on every solder joint for each set of conditions. Through trial and error, it was observed that a peak holding load of 30 mN was ideal for the nanoindentation tests. Using this high load not only prevented creep effects but also ensured that the indents made were deep enough to prevent surface effects while also ensuring these large indents covered all the solder phases present. A schematic depicting all the experimental techniques described above and used for this study has been presented in Figure 3.21.

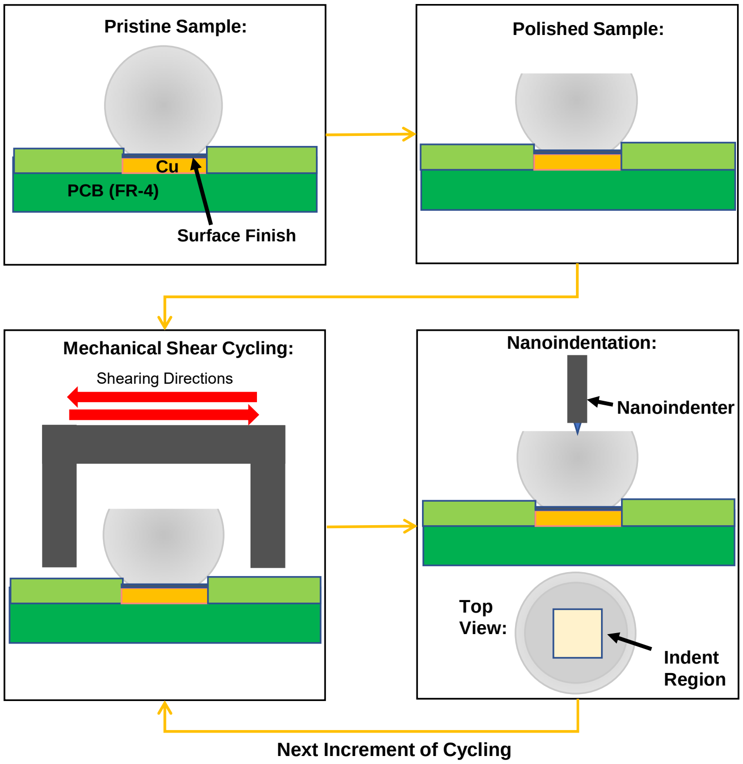

Figure 3.21 Schematic showing the experimental procedure

3.11 Measurement of Elastic Modulus and Hardness

A typical load (P) versus displacement (h) curve, obtained after a nanoindentation test, is presented in Figure 3.22. This curve has three different segments where the first, second, and third segments represent the displacements during the loading, holding and unloading period, respectively.

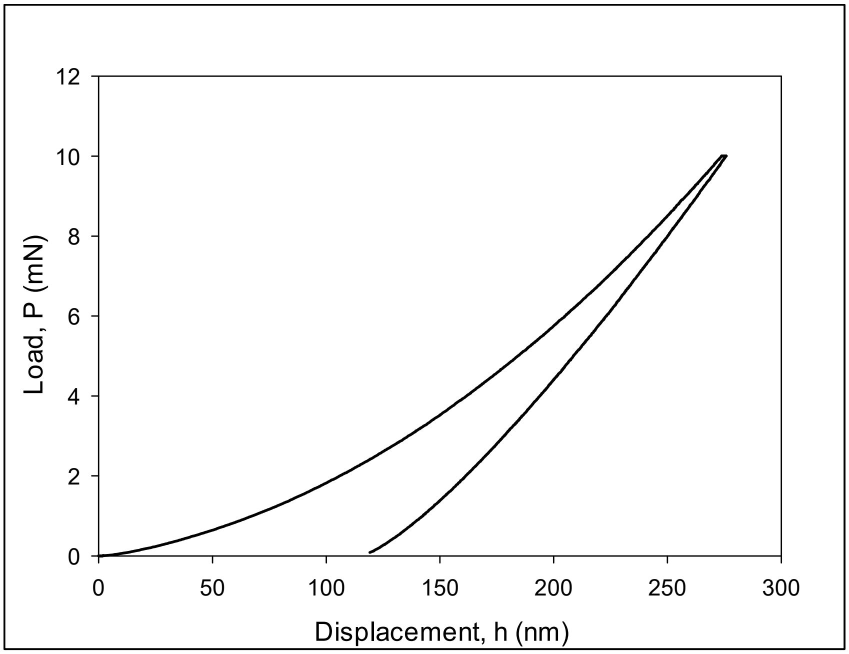

Figure 3.22 An example of the load-displacement curve obtained after nanoindentation testing.

During a nanoindentation experiment, the effects of the non-rigidity of an indenter, during a nanoindentation experiment, can be addressed by introducing a term called reduced modulus (E_r) through the following equation:

$$\frac{1}{E_r} = \frac{(1-\nu^2)}{E} + \frac{(1-\nu_i^{\,2})}{E_i} \tag{3.7}$$

Where, E is the elastic modulus of the test specimen, E_i is the known elastic modulus of the indenter tip material, ν and ν_i are the Poisson's ratio of the test specimen and the indenter tip, respectively. Typically reduced modulus was measured from an indentation experiment using the following equation:

$$E_r = \frac{\sqrt{\Pi}}{2} \times \frac{S}{\sqrt{A}} \tag{3.8}$$

Where, S is the stiffness of the test specimen at the maximum load and A is the projected contact area at the maximum load. Stiffness was determined from the initial slope ($\frac{dP}{dh}$) of the unloading segment of a load displacement curve. The contact area A was measured following the technique proposed by Oliver and Pharr [133] where they assumed the contact area to be a function of contact depth. For an ideal Berkovich tip, it can be expressed as

$$A(h_c) = 24.5h_c^2 \tag{3.9}$$

In order to address any deviation from the ideal Berkovich geometry due to tip blunting, a modified version of equation 3.6 was utilized.

$$A(h_c) = 24.5h_c^2 + C_1h_c^1 + C_2h_c^{1/2} + C_3h_c^{1/4} + C_4h_c^{1/8} + C_5h_c^{1/16} \tag{3.10}$$

Where, C_1, C_2, C_3, C_4, and C_5 are fitting constants. In order to determine the values of these constants, multiple indents were made at multiple depths on a quartz sample with known elastic modulus (69.6 GPa). The contact areas at the different known depths were determined from equation 3.5 and these values were plotted to get an A versus h_c plot. The values of constants C_1 to C_5 were determined by fitting the plot by Equation 3.10. Once the values of the constants are known for a particular tip geometry, equation 3.8 was used to determine the value of reduced modulus (E_r) for any unknown material and equation 3.7 was used to convert E_r to elastic modulus E.

Hardness is a material property that defines the resistance of the surface against plastic deformation. During a nanoindentation experiment, hardness H was determined by dividing the maximum load by the projected contact area.

$$H = \frac{P_{max}}{A} \tag{3.11}$$

Tabor [134-135] developed an approximate relationship between hardness and yield strength of which is true for many metals.

$$H \approx 3\sigma_Y \qquad \text{Or} \qquad \sigma_Y \approx \frac{H}{3} \tag{3.12}$$

The above equation was used to determine stress during nanoindentation experiments.

3.12 Summary and Discussion

All the experimental procedures and the data processing steps were presented in this chapter. Micro-scale uniaxial tensile specimens were prepared in a rectangular shaped hollow glass tube using a vacuum suction method. Uniaxial tensile tests were performed using a micro tension torsion testing system. Later, newly designed micro-cylinder shaped uniaxial lead free solder test specimens have been introduced to solve the buckling problem during compression in the cyclic or fatigue testing. Gripping fixtures were designed and added to the test system to grip the cylindrical specimens. After testing, empirical models were utilized to represent the stress strain, creep, and cyclic stress-strain experimental data.

To study the effects of mechanical cycling on the solder microstructure, and the aging induced solder microstructural changes during fatigue testing, SAC305 and SAC Q uniaxial samples with various durations of prior mechanical cycling have been prepared. After polishing, small indentation marks were added to the cross-sections to facilitate locating the identical regions of interest. Then the microstructural changes in the fixed regions during cycling with and without aging were examined using SEM.

In the later part of this study, a unique specimen preparation procedure was to fabricate actual 3 x 3 BGA solder joint array specimens to explore the effect of shear mechanical cycling on damage accumulation in SAC305 and SAC_Q solder joints. The solder balls were cycled individually with a peak load of 600 gf by a Micromechanical tester for various durations (50, 100, 150, 200, 300 cycles), all of which were below the fatigue life of these joints. After each cycling duration, nanoindentation experiments were conducted on the samples to test for changes in elastic modulus, hardness, and creep response.

CHAPTER 4

HIGH TEMPARATURE MECHANICAL BEHAVIOR AND ANAND PARAMETERS OF Bi-DOPED SAC ALLOYS

4.1 Introduction

Solder joint reliability in harsh environment applications are big concerns in the electronic packaging industry. The reliabilities of electronic packages used in various products depend on the environmental conditions experienced during field use. Consumer electronics are typically designed using maximum operating temperatures of 100 °C or less. However, there are several important harsh environment uses of electronic packaging, where electronics can be exposed to temperatures up to 200 °C. This leads to reduced values of the solder mechanical properties due to the normal temperature dependencies exhibited by metals. It is important to make accurate predictions of solder joint reliability at extreme high Temperatures. The Anand viscoelastic constitutive model is often used to represent the material behavior of the solder in finite element simulations. This model is defined using nine material parameters, and the reliability prediction results are often highly sensitive to the Anand parameters.

In this chapter, several SAC+Bi lead free solder materials recommended for high reliability applications have been chemically analyzed and then mechanically tested in order to determine the temperature dependent mechanical properties of these alloys. The alloys are referred to as Ecolloy (SAC_R), CYCLOMAX (SAC_Q), and Innolot by their vendors. The first two SAC-Bi alloys (SAC_R and SAC_Q) were found to be composed of Sn, Ag, Cu, and a single X-element dopant. Such solders are commonly referred to as SAC-X in the literature. For the third material (Innolot), three different dopants are present along with Sn, Ag and Cu. The EDX method was used to determine the approximate chemical composition of the materials, and Bismuth (Bi) was found to be the X-additive for both SAC_R and SAC_Q. In addition, the SAC_R material was found to have no silver (Ag), which is the reason it is marketed as a low cost (economy) material.

The mechanical behavior of these alloys have been explored at several extreme high temperatures from 125 to 200 °C. For each of 4 elevated temperatures (T = 125, 150, 175, and 200 °C), tensile stress-strain tests were performed at three strain rates (SR = 0.001, 0.0001, and 0.00001 sec^{-1}). For each alloy and testing temperature, the stress-strain curve shape and high temperature tensile properties (initial modulus, yield stress, and ultimate tensile strength) of the solder alloys were measured and compared. Test specimens were initially solidified with water quenched (WQ) cooling profiles.

Later, the nine Anand parameters were determined for SAC_Q solder alloy from a set of uniaxial tensile tests performed at several strain rates and temperatures. Testing conditions included strain rates of 0.001, 0.0001, and 0.00001 (sec^{-1}), and temperatures of 100, 125, 150, 175, and 200 ºC. The Anand parameters were calculated from each set of stress-strain data using an established procedure that is described in detail in the chapter. The mechanical properties and the values of Anand parameters for this new Bi-doped alloy was compared with standard SAC305 lead free alloys.

4.2 Anand Viscoplastic Constitutive Model

The Anand viscoelastic constitutive model [55] is often used to represent the material behavior of the lead free solders in finite element simulations. This model is defined using nine material parameters, and the reliability prediction results are often highly sensitive to the values of the Anand parameters. There are several publications listing values of Anand parameters for particular solder alloys. For example, Anand parameters for alloys such as Sn-3.5Ag, SAC105, SAC305, and SAC387 have been documented [53-54, 61, 98-100]

4.2.1 Review of Anand Model Equations (1D)

Several authors [53-54, 59] have previously reviewed the general equations of the Anand constitutive model for one-dimensional (uniaxial) stress states. The theoretical approach is based on a scalar internal variable s, which represents the material resistance to plastic flow. The model includes three equations: (1) stress equation, (2) flow equation, and (3) evolution equation. These expressions unify the rate-independent plastic behavior and creep behavior of the material. The Anand model does not contain an explicit yield condition or a loading/unloading criterion.

The stress equation is expressed as

$$\sigma = c\,s\,;\ c < 1 \tag{4.1}$$

Where, s is the scalar internal valuable. Quantity c is a function of the temperature and strain rate, and is given by

$$c = c(\dot{\varepsilon}_p, T) = \frac{1}{\xi}\sinh^{-1}\left\{\left[\frac{\dot{\varepsilon}_p}{A}e^{\left(\frac{Q}{RT}\right)}\right]^m\right\} \tag{4.2}$$

where $\dot{\varepsilon}_p$ is the plastic strain rate, A is the pre-exponential factor, ξ is the multiplier of stress, m is the strain rate sensitivity, Q is the activation energy, R is the universal gas constant, and T is the absolute temperature. By substitution of eq. (4.2) into eq. (4.1), the reformatted stress equation becomes:

$$\sigma = \frac{s}{\xi}\sinh^{-1}\left\{\left[\frac{\dot{\varepsilon}_p}{A}e^{\left(\frac{Q}{RT}\right)}\right]^m\right\} \tag{4.3}$$

The Anand model flow equation is found by solving for the strain rate in eq. (4.3):

$$\dot{\varepsilon}_p = A\, e^{-\left(\frac{Q}{RT}\right)} \left[\sinh\left(\xi \frac{\sigma}{s}\right)\right]^{\frac{1}{m}} \tag{4.4}$$

The evolution equation describes the variation of internal variable s with time. In its differential form, it can be expressed as:

$$\begin{aligned} \dot{s} &= h(\sigma, s, T)\dot{\varepsilon}_p \\ \dot{s} &= \left[h_o \left(1 - \frac{s}{s^*}\right)^a \operatorname{sign}\left(1 - \frac{s}{s^*}\right)\right] \dot{\varepsilon}_p ; \quad a > 1 \end{aligned} \tag{4.5}$$

The term $h(\sigma, s, T)$ in eq. (4.5) is associated with dynamic hardening and recovery, and its initial value is the hardening constant h(0) = h_o. Parameter a is the strain rate sensitivity of the hardening process, and parameter s* is the saturation value of the deformation resistance given by

$$s^* = \hat{s}\left[\frac{\dot{\varepsilon}_p}{A} e^{\left(\frac{Q}{RT}\right)}\right]^n \tag{4.6}$$

Where, $\hat{s}$ is a coefficient, and n is the strain rate sensitivity. Equation (4.5) can be expressed as

$$ds = h_o \left(1 - \frac{s}{s^*}\right)^a d\varepsilon_p \tag{4.7}$$

For s < s*, and then integrated resulting in an evolution expression for the internal variable s:

$$s = s^* - \left[\left(s^* - s_o\right)^{(1-a)} + (a-1)\left\{(h_o)\left(s^*\right)^{-a}\right\}\varepsilon_p\right]^{\frac{1}{1-a}} \tag{4.8}$$

Where, the initial value is $s(0) = s_o$ at time $t = 0$. Combining eq. (4.6) and eq. (4.8) results in an evolution equation for the internal variable s in terms of the plastic strain and plastic strain rate:

$$s = \hat{s}\left[\frac{\dot{\varepsilon}_p}{A}e^{\left(\frac{Q}{RT}\right)}\right]^n - \left[\left(\hat{s}\left[\frac{\dot{\varepsilon}_p}{A}e^{\left(\frac{Q}{RT}\right)}\right]^n - s_o\right)^{(1-a)} + (a-1)\left\{(h_o)\left(\hat{s}\left[\frac{\dot{\varepsilon}_p}{A}e^{\left(\frac{Q}{RT}\right)}\right]^n\right)^{-a}\right\}\varepsilon_p\right]^{\frac{1}{1-a}} \qquad (4.9)$$

Or,

$$s = s(\dot{\varepsilon}_p, \varepsilon_p) \qquad (4.10)$$

The final versions of the Anand model equations are the stress equation in eq. (4.3), the flow equation in eq. (4.4), and the integrated evolution equation in eq. (4.9). These expressions include 9 material parameters: A, ξ, Q/R, m in eqs. (4.3, 4 4); and constants h_o, a, s_o, $\hat{s}$, and n in eq. (4.9).

4.2.2 Uniaxial Stress-Strain Theoretical Response

Equations (4.3) and (4.9) can be combined to give an expression for the uniaxial stress-strain law (post yield) predicted by the Anand model:

$$\sigma = \frac{1}{\xi}\sinh^{-1}\left\{\left[\frac{\dot{\varepsilon}_p}{A}e^{\left(\frac{Q}{RT}\right)}\right]^m\right\}\left(\hat{s}\left[\frac{\dot{\varepsilon}_p}{A}e^{\left(\frac{Q}{RT}\right)}\right]^n - \left[\left(\hat{s}\left[\frac{\dot{\varepsilon}_p}{A}e^{\left(\frac{Q}{RT}\right)}\right]^n - s_o\right)^{(1-a)} + (a-1)\left\{(h_o)\left(\hat{s}\left[\frac{\dot{\varepsilon}_p}{A}e^{\left(\frac{Q}{RT}\right)}\right]^n\right)^{-a}\right\}\varepsilon_p\right]^{\frac{1}{1-a}}\right)$$

$$\sigma = \sigma(\dot{\varepsilon}_p, \varepsilon_p) \qquad (4.11)$$

For a uniaxial tensile test performed at fixed (constant) strain rate $\dot{\varepsilon}_p$ and constant temperature T, this equation represents nonlinear stress-strain behavior in the form of a power law type function after yielding:

$$\sigma = \sigma(\varepsilon_p) \qquad (4.12)$$

The yield stress (σ_Y) and the Ultimate Tensile Strength (UTS = maximum or saturation stress) can be obtained from eq. (4.11) by taking the limits for small and large plastic strains. The yield stress is given by the limit as ε_p goes to 0:

$$\sigma_Y = \sigma\big|_{\varepsilon_p \to 0} = cs_0 = \frac{1}{\xi}\sinh^{-1}\left\{\left[\frac{\dot{\varepsilon}_p}{A} e^{\left(\frac{Q}{RT}\right)}\right]^m\right\} s_0 = c\,s_0 \equiv \sigma_0 \tag{4.13}$$

While, the UTS is given by the limit as ε_p goes to ∞:

$$\text{UTS} = \sigma\big|_{\varepsilon_p \to \infty} = \frac{\hat{s}}{\xi}\left[\frac{\dot{\varepsilon}_p}{A} e^{\left(\frac{Q}{RT}\right)}\right]^n \sinh^{-1}\left\{\left[\frac{\dot{\varepsilon}_p}{A} e^{\left(\frac{Q}{RT}\right)}\right]^m\right\} \equiv \sigma^* \tag{4.14}$$

By substituting eq. (4.14) into eq. (4.11), the stress-strain power law relation after yielding can be expressed as:

$$\sigma = \sigma^* - \left[\left(\sigma^* - c\,s_0\right)^{(1-a)} + (a-1)\ \left\{\left(ch_0\right)\left(\sigma^*\right)^{-a}\right\} \varepsilon_p\right]^{1/(1-a)} \tag{4.15}$$

4.2.3 Procedure for Determining the Anand Model Parameters from Uniaxial Stress Strain data

Anand [55] suggested using stress-strain data measured over a wide range of temperatures and strain rates to determine the 9 parameters (A, ξ, Q/R, m, h_o, a, s_o, $\hat{s}$, and n) in the viscoelastic constitutive relations presented above. Several previous studies [53-54, 59], have outlined a procedure for performing this task. Values of the saturation stress (σ^* = UTS) can be extracted from the peak stress values on the stress-strain curves for several temperatures and strain rates. Also, stress vs. plastic strain data (σ vs. ε_p) can be extracted from the recorded stress-strain curves (σ, ε) at the various temperatures and strain rates. The conversion of total strain to plastic strain for each data set is performed using:

$$\varepsilon_p = \varepsilon - \frac{\sigma}{E} \tag{4.16}$$

Where, E is the initial elastic modulus. The sequential procedure for calculating the Anand model parameters consists of:

1. The six Anand parameters $\hat{s}$, ξ, A, Q/R, n and m are determined using a nonlinear least-squares regression fit of eq. (4.14) to the recorded saturation stress (UTS) vs. temperature and strain rate data.
2. The remaining three Anand parameters (s_o, h_o, and a) are found using nonlinear regression fits of eq. (4.15) to the recorded stress vs. plastic strain data at several temperatures and strain rates.

4.3 Chemical Composition of the SAC-Bi Alloys

Chemical compositions of the SAC-Bi alloys are presented in Table 4.1 along with the compositions of the traditional SAC305 alloys Innolot has a well published 6-element target composition, while the compositions of SAC_R (Ecolloy) and SAC_Q (CYCLOMAX) are unpublished. Energy Dispersive X-Ray Spectroscopy (EDX) was used to explore the compositions of these two alloys. All three alloys were found to employ Bismuth (Bi) as the primary X-additive. The composition of SAC_R is most similar to that of SAC 105. However, the SAC_R material does not have any measureable silver (Ag) content, contrary to all other SAC alloys. This is most likely the reason it is marketed as a low cost (economy) material. The silver contents of SAC_Q and Innolot are similar to SAC405, at 3.41% and 3.80%, respectively.

Table 4.1 Chemical Compositions of the Solder Alloys

Alloy	Sn	Ag	Cu	Bi	Ni	Sb
SAC_R	96.62	0.00	0.92	2.46	0.00	0.00
SAC_Q	92.77	3.41	0.52	3.30	0.00	0.00
Innolot	90.95	3.80	0.70	3.00	0.15	1.40
SAC 305	96.50	3.00	0.50	0.00	0.00	0.00

4.4 Stress-Strain Data for Various Temperatures

As mentioned earlier, we performed the uniaxial tensile test of the water quenched doped lead free solder specimens at temperatures of 25, 50, 75, 100, 125, 150, 175, and 200 °C at a strain rate of 0.001 sec^{-1} for SAC_R and Innolot. We also performed the same testing for SAC_Q at same different temperatures but, in this case, we considered three different strain rates (0.001, 0.0001, and 0.00001 sec^{-1}). The measured high temperature stress-strain curves for SAC_R, SAC_Q, and Innolot alloys are shown in Figures 4.1-4.3. Each colored curve is the "average" experimental stress-strain curve for a particular strain rate and temperature. They were determined by performing nonlinear regression fits of the empirical model in Equation 3.2 (chapter 3) to the experimental data (six recorded stress-strain curves for each alloy and set of conditions). The colors of the curves represent the testing temperature with black = 25 °C, blue = 50 °C, green = 75 °C, brown =100 °C red = 125 °C, purple = 150 °C, cyan = 175 °C, and green = 200 °C. Again, in each plot, the top curve represents the average stress-strain curve at 25 °C, and the bottom curve is the average stress-strain curve at 200 °C. From the graphs in figures 4.1 - 4.3, we see that the effective elastic modulus, yield stress (YS), and ultimate tensile strength (UTS) decrease monotonically with temperature, which was expected. The decrease was nearly linear with the testing temperature for all alloys. By comparing the analogous results for the same temperature and alloy but different strain rates, we observed that as the strain rate decreases, the effective elastic modulus, yield stress (YS) and ultimate tensile strength (UTS) decrease. Among these three new doped alloys, Innolot and SAC_Q exhibited much higher mechanical properties (stiffness and strength) than SAC_R samples at any specific strain rate and temperature due to the presence of Ag.

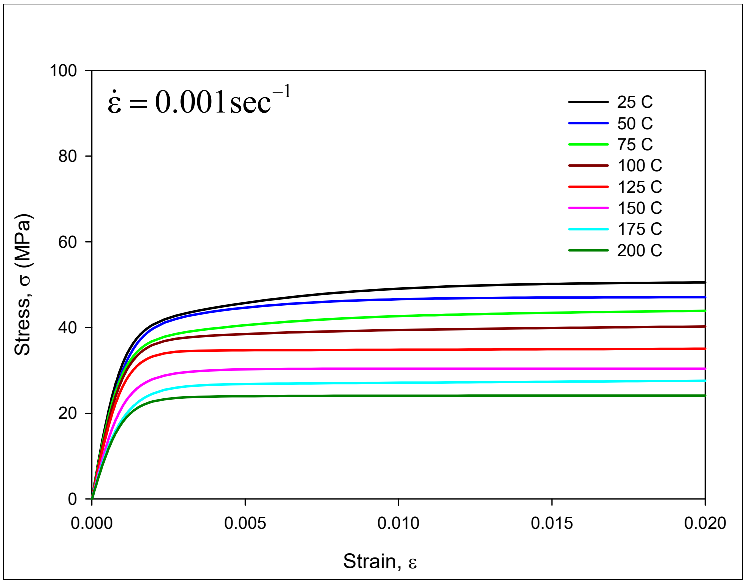

Figure 4.1 Stress-Strain Curves for SAC_R (WQ)

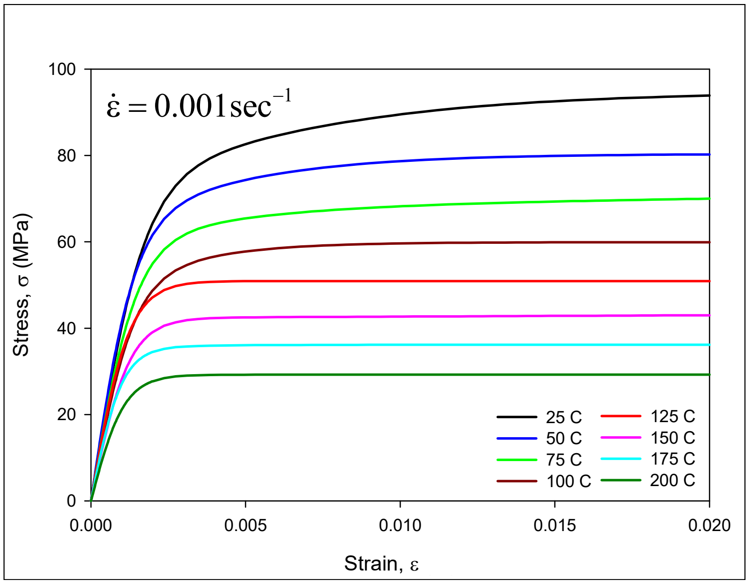

Figure 4.2 Stress-Strain Curves for SAC_Q (WQ)

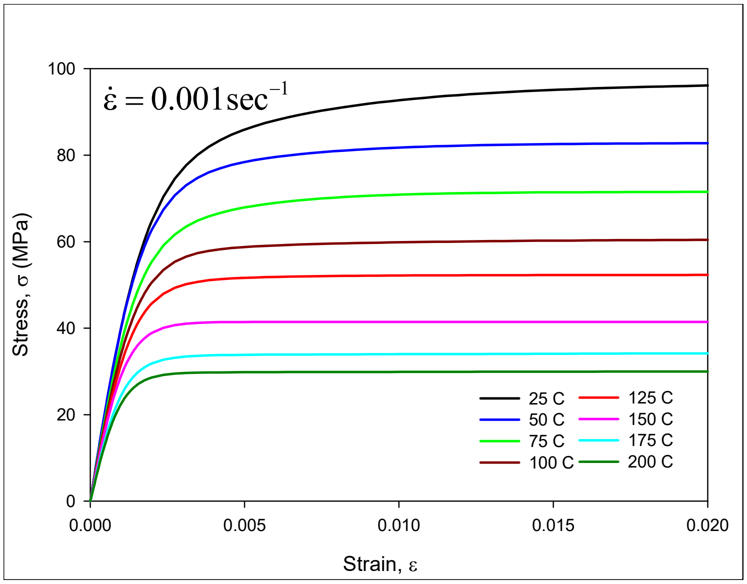

Figure 4.3 Stress-Strain Curves for Innolot (WQ)

4.5 Comparison of Mechanical Behavior of Solder Alloy at Various Temperature

Comparisons of the uniaxial tensile test results for the five solder alloys at different test temperature and strain rate are shown in Figures 4.4 which represents comparison at 0.001 $\sec^{-1}$ strain rate. In each plot, different color curve represents different alloy with green = SAC_R blue = SAC_Q, black = Innolot, green dotted line = SAC_R and blue dotted line = SAC305. It can be easily seen that both the SAC_Q and Innolot alloys strongly outperformed SAC305 and SAC_R outperformed SAC105 at a particular temperature, with much higher ultimate tensile strength (UTS) and superior initial elastic modulus. The stress-strain curves for SAC_Q and Innolot are very similar at each strain rate, but Innolot exhibits slightly higher mechanical properties. The strength of SAC_R is slightly higher than SAC105, even though SAC_R does not contain any Ag. Similar results were found for all testing temperatures.

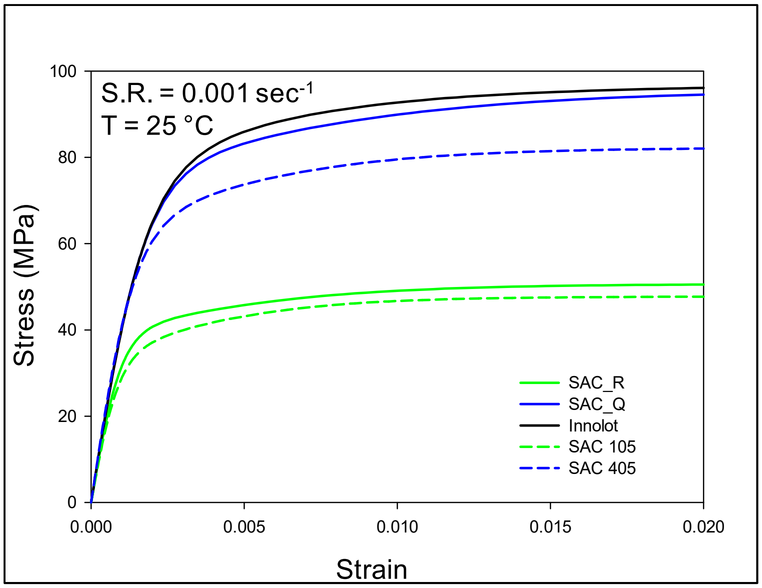

Figure 4.4 Stress-Strain Curves for SAC_Q with and without Prior Aging

The mechanical properties of the three alloys have been extracted from the measured stress-strain data and tabulated in Tables 4.2. Large reductions in the properties were observed to occur between T = 25 °C and T = 200 °C. For example, ultimate tensile strength dropped 40-50% for SAC_R alloy and 60-70% dropped for SAC_Q and Innolot. Linear variations in the properties with temperature were observed.

As shown in Figure 4.30 (a), among all three SAC-Bi alloys, Innolot has the highest strength whereas SAC_R has lowest strength which is about 50% of that of Innolot. The presence of Bi along with Ni and Sb is the reason for superior mechanical properties of Innolot. While comparing with SAC105, it was found that although SAC_R does not have any Ag, it has better mechanical properties than SAC105. The presence of Bi along with slightly more Cu is the reason for that. It was found that the strength of SAC105 was 47 MPa when tested at 25 ºC and the strength dropped to 22 MPa at 125 ºC testing temperature. Reduction of strength was found to be 53%. Whereas the strength of SAC_R dropped from 49 MPa (at 25 ºC) to 34 MPa (at 125 ºC), which indicates only 30% reduction in strength. Hence it can be said that the strength of SAC_R is less sensitive of testing temperature than SAC105.

Table 4.2 Tensile Stress-Strain Properties of Doped SAC Solder Alloys

Temperature	SAC_R		SAC_Q		Innolot	
	U.T.S	Y.S.	U.T.S	Y.S.	U.T.S	Y.S.
25	49.05	43.19	92.53	79.56	92.37	82.00
50	46.48	42.84	78.75	71.11	81.90	75.40
75	42.11	38.82	67.67	63.12	70.58	65.37
100	39.08	37.56	59.78	55.53	59.31	57.43
125	34.88	32.59	51.81	48.55	51.91	50.46
150	29.21	28.04	42.73	42.02	41.62	41.03
175	26.59	25.30	36.27	35.67	33.69	33.34
200	24.03	23.71	29.33	28.44	29.94	29.54

4.6 Stress-Strain Data for Various Strain Rates

Mechanical stress-strain tests have been performed on SAC_Q solder samples at 15 different test conditions achieved by a combination of three strain rates ($\dot{\varepsilon}$ = 0.001, 0.0001, and 0.00001 sec-1) and five test temperatures (T = 100, 125, 150, 175, and 200 ºC). Test specimens were prepared using WQ cooling profile (WQ) to yield the fine microstructures and the upper limits of the mechanical properties for SAC_Q alloy. From the experimental stress-strain data, the nine Anand constitutive model parameters were determined for the alloy SAC_Q. The recorded stress-strain curves for SAC_Q (WQ) at strain rates of 0.001, 0.0001, and 0.00001 sec^{-1} are shown in Figures 4.7a, 4.7b, and 4.7c, respectively. Each curve in these plots is an “average” stress-strain curve representing the fit of the empirical model in eq. (3.2) to the 6-8 recorded stress-strain curves for the particular strain rate and temperature. The eight different colored curves in each graph are the results for the 5 testing temperatures (T = 25, 50, 75, 100, 125, 150, 175, and 200 °C). For example, the top (black) curve in each plot is the average stress-strain curve at room temperature (25 °C), and the bottom (green) curve is the average stress-strain curve at 200 °C. By comparing the analogous results for the same temperature and alloy but different strain rates, we observed that as the strain rate decreases, the effective elastic modulus, yield stress (YS) and ultimate tensile strength (UTS) decrease.

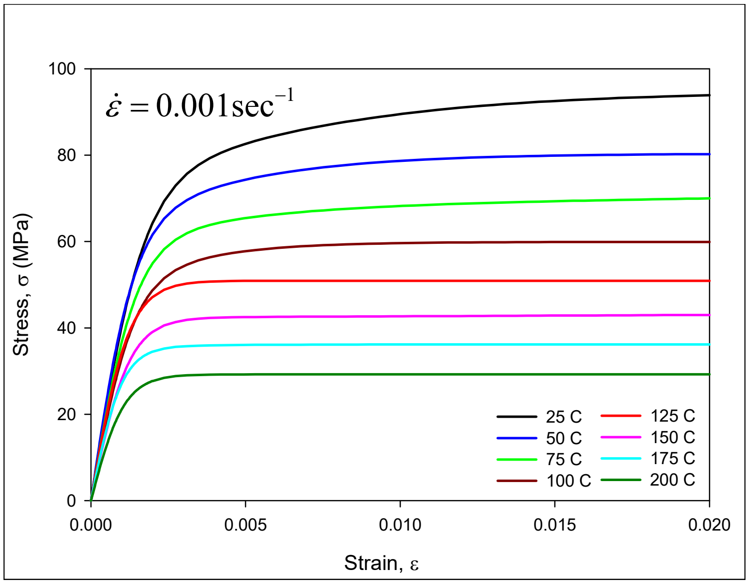

(a)

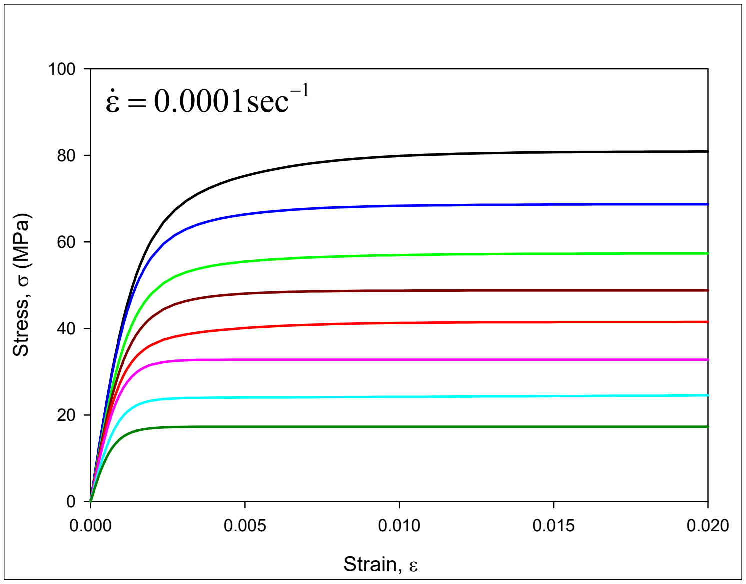

(b)

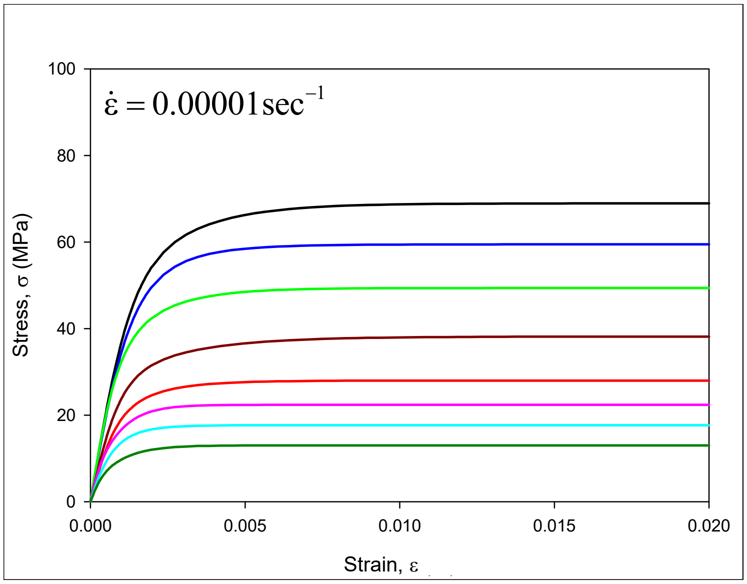

(c)

Figure 4.5 (a-c) Stress-Strain Curves Obtained for SAC_Q (WQ)

4.7 The Anand Parameters for SAC_Q

The Anand model parameters for the SAC_Q lead free solder materials have been determined from the temperature and strain rate dependent stress-strain data in Figures 4.5 (a-c). As discussed previously, a least-squares regression fitting procedure was utilized to extract the optimal set of Anand parameters using the stress-strain curves for each pre-test conditions at 5 different temperatures and 3 different strain rates. The curves in each figure were first processed to extract saturation stress (UTS) vs. strain rate and temperature data for each alloy, as well as stress vs. plastic strain data at several strain rates and temperatures for each alloy. From the extracted data from each Figure, the nine Anand parameters were calculated for each alloy using equations 4.13 and 4.15, and the nonlinear regression analysis procedure discussed in section 4.2.3. The calculated Anand parameters are tabulated in Table 4.3.

Table 4.3 Anand Parameters for SAC_Q

Par. No.	Anand Par.	Units	Temperature Range (25- 125 °C)	Temperature Range (25- 200 °C)
1	s_o	MPa	32.95	46.134
2	Q/R	1/K	10742	10506
3	A	sec^{-1}	7000	2000
4	ξ	-	6	6
5	m	-	0.35	0.35
6	h_o	MPa	284026	238625
7	$\hat{S}$	MPa	60.48	72.72
8	n	-	0.0077	0.0033
9	a	-	1.59	1.5

Once the Anand constants are determined for each alloy, it is possible to predict the stress (σ) vs. plastic strain (ε_p) curve at a particular set of temperature, strain rate, and alloy using equation 4.11. This result can be adjusted to a stress (σ) vs. total strain curve (ε) by adding the elastic strain to the plastic strain:

$$\varepsilon = \varepsilon_e + \varepsilon_p \qquad \varepsilon_e = \frac{\sigma}{E} \tag{4.17}$$

Where, E is the initial elastic modulus at the particular temperature, strain rate, and aging conditions.

Figure 4.7 illustrates the correlation between the model predictions and the experimental stress-strain curves for SAC_Q at various temperatures ranging from 25 to 125 °C. In this case, the Anand model constants from Table 4.3 for the alloy SAC_Q were utilized. The curves from experimental data, as shown earlier in Figure 4.2, were in excellent agreement with the predicted stress strain curves.

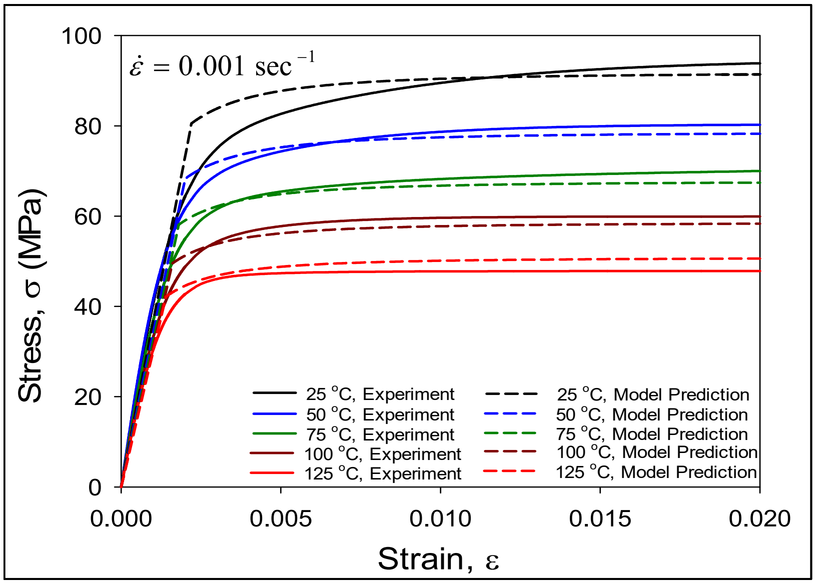
$\dot{\varepsilon} = 0.001\ \text{sec}^{-1}$
Stress, σ (MPa)
Strain, ε
0
20
40
60
80
100
0.000
0.005
0.010
0.015
0.020
25 °C, Experiment
50 °C, Experiment
75 °C, Experiment
100 °C, Experiment
125 °C, Experiment
25 °C, Model Prediction
50 °C, Model Prediction
75 °C, Model Prediction
100 °C, Model Prediction
125 °C, Model Prediction

(a)

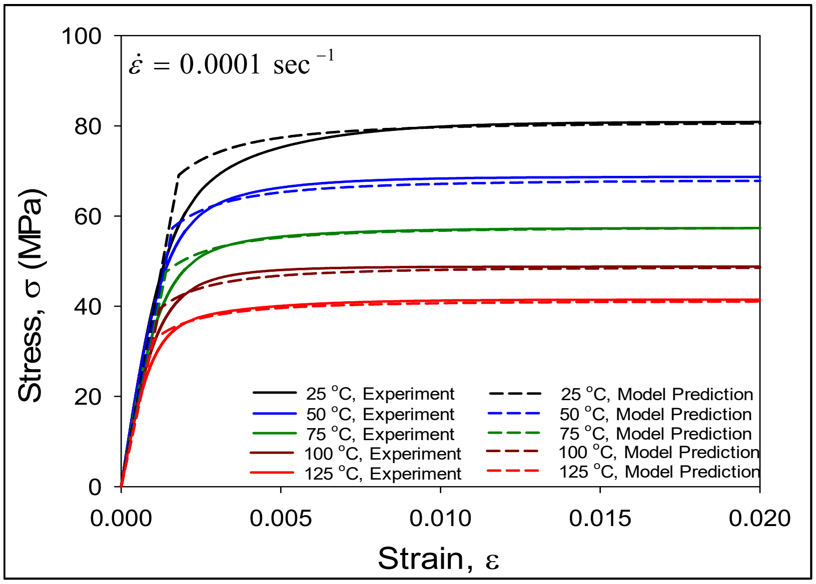
$\dot{\varepsilon} = 0.0001\ \text{sec}^{-1}$
Stress, σ (MPa)
Strain, ε
0
20
40
60
80
100
0.000
0.005
0.010
0.015
0.020
25 °C, Experiment
50 °C, Experiment
75 °C, Experiment
100 °C, Experiment
125 °C, Experiment
25 °C, Model Prediction
50 °C, Model Prediction
75 °C, Model Prediction
100 °C, Model Prediction
125 °C, Model Prediction

(b)

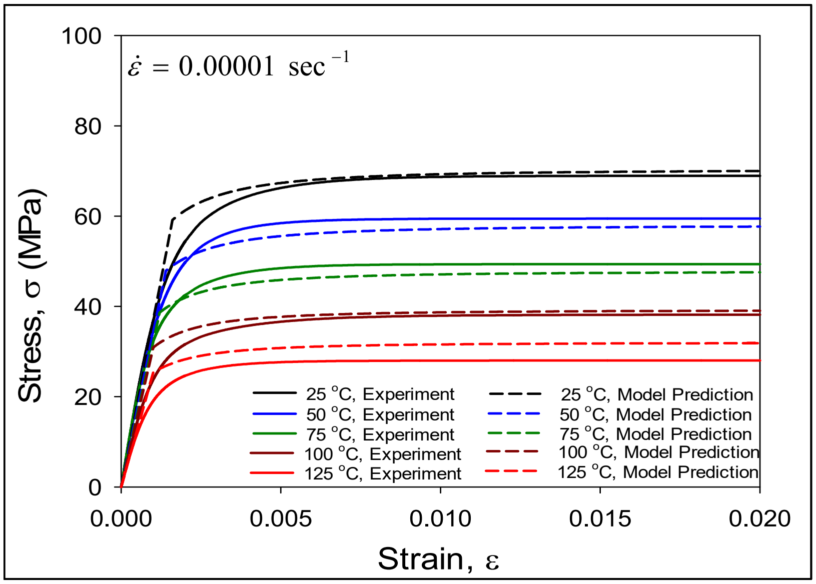

(c)

Figure 4.6 (a-c) Comparison between Experimental Data and Anand Model Predictions for SAC_Q (WQ) at temperatures ranging from 25 to 125 °C

However, the deviation between the experimental results and model prediction increases with the increasing temperatures after 125 °C. Since the Anand parameters were found out based on stress-strain data in the range from 25 to 125 °C, the model might not predict the accurate values at high temperature like 200 °C. In our study, we estimated another set of parameters using Anand model which will be a better fit to the experimental results at the higher range of 25 to 200 °C. Thus, the Anand model will be able to represent the stress-strain curves more accurately over a wide range of temperatures and strain rates.

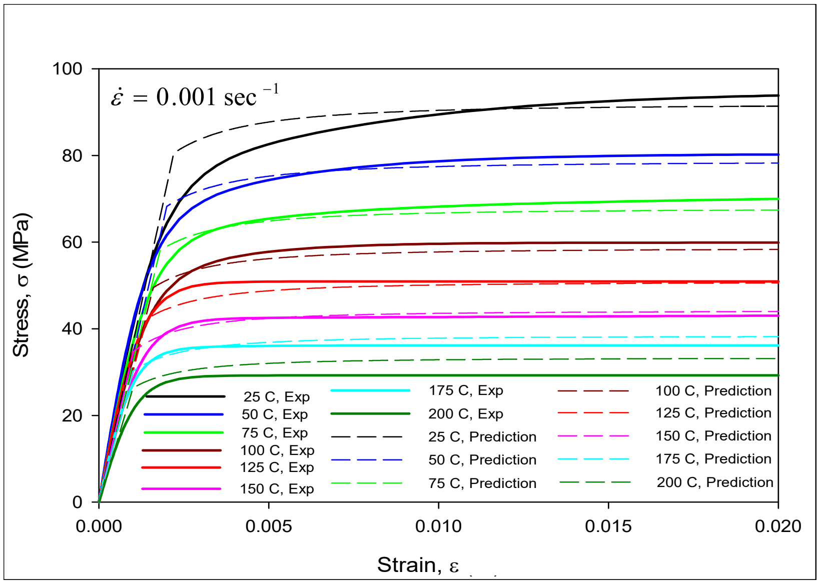
$\dot{\varepsilon} = 0.001\ \mathrm{sec}^{-1}$
Stress, σ (MPa)
Strain, ε
0
20
40
60
80
100
0.000
0.005
0.010
0.015
0.020
25 C, Exp
50 C, Exp
75 C, Exp
100 C, Exp
125 C, Exp
150 C, Exp
175 C, Exp
200 C, Exp
25 C, Prediction
50 C, Prediction
75 C, Prediction
100 C, Prediction
125 C, Prediction
150 C, Prediction
175 C, Prediction
200 C, Prediction

(a)

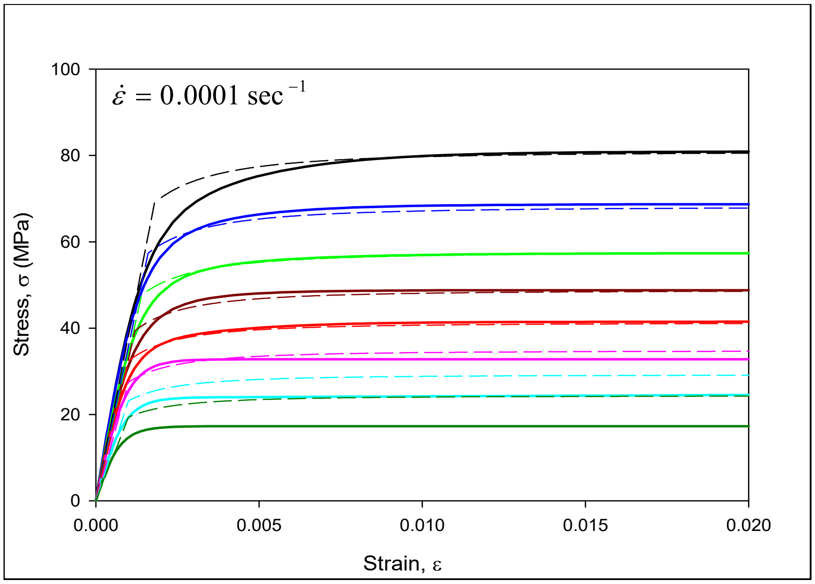
$\dot{\varepsilon} = 0.0001\ \mathrm{sec}^{-1}$
Stress, σ (MPa)
Strain, ε
0
20
40
60
80
100
0.000
0.005
0.010
0.015
0.020

(b)

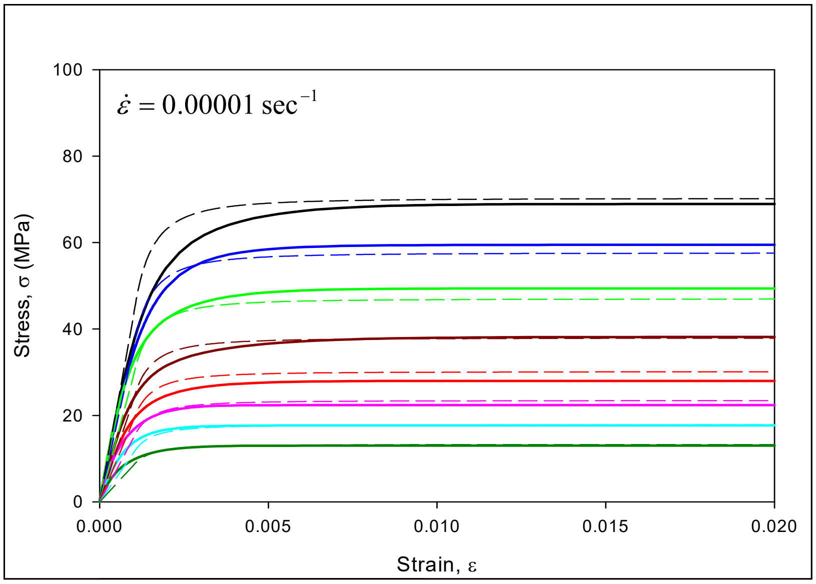

(c)

Figure 4.7 (a-c) Comparison between Anand Model Predictions and Experimental Data for SAC_Q (WQ) temperatures ranging from 25 to 200 °C

4.8 Summary and Discussion

In this chapter, three new SAC-Bi lead free solder materials recommended for high reliability applications have been chemically analyzed and then mechanically tested in order to determine the nine Anand parameters. Test condition includes at a strain rate of 0.001 sec^{-1} and temperatures of 125, 150, 175, and 200 °C for samples SAC_R and Innolot, whereas several sets of constant strain rate and temperature tests were conducted on the SAC_Q samples including strain rates of 0.001, 0.0001, and 0.00001 (sec^{-1}) and temperatures of 100, 125, 150, 175 and 200 °C. For preparing the testing specimens, water quenched (WQ) solidification profile has been used, which is expected to attain the characteristics of fine microstructures and thus lead to the upper limits of the mechanical properties for each alloy. From the experimental results, the effective elastic modulus, yield stress (YS), and ultimate tensile strength (UTS) were found to be decreased monotonically with temperature. The decrease was nearly linear with the testing temperature for all alloys. SAC_Q was also compared with the analogous results for the same temperature but at different strain rates. For different strain rates, as the strain rate decreases, the effective elastic modulus, yield stress (YS) and ultimate tensile strength (UTS) were also decreased. Same trend in case of SAC_R and Innolot was also expected. Moreover, the Innolot and SAC_Q exhibited much higher mechanical properties (stiffness and strength) than SAC_R samples at any specific strain rate and temperature due to the presence of Ag. Although the SAC_R material does not have any silver, it was shown to have better mechanical behavior than SAC 105 due to the presence of Bismuth (Bi) along with a little higher percentage of Copper (Cu). The Innolot and SAC_Q materials were shown to have higher strengths than SAC405.

After completing tensile testing, the Anand parameters were calculated from each set of stress-strain data for SAC_Q using an established procedure that is described earlier. Afterward, the stress-strain curves were plotted using the parameters under various conditions, and an excellent relationship was evident between the predicted results and experimental stress-strain curves.

CHAPTER 5

EFFECTS OF AGING ON CYCLIC STRESS-STRAIN BEHAVIOR OF DOPED SAC SOLDER MATERIALS

5.1 Introduction

Fatigue of solder joints exposed to thermal cycling is a common electronic packaging failure mode. Stresses and strains often result in electronic assemblies exposed to a temperature changing environment due to mismatches in the coefficients of thermal expansion (CTE) of the soldered components and the printed circuit board (PCB). Therefore, cyclic temperature changes can lead to alternating stresses and strains within the solder joints. Such exposures can occur in products that experience power cycling or during accelerated life thermal cycling tests used for qualification. Cyclic loading typically leads to micro cracks forming within the solder material, followed by macro cracks and eventually to fatigue failure. Energy dissipation occurs during cyclic loading due to yielding and occurrence of viscoplastic deformations, and can be quantified using the area of the cyclic stress-strain curve hysteresis loops, which is equal to the strain energy density dissipated per cycle. While effects of aging have been studied in some detail on the solder constitutive behavior such as stress-strain and creep, there have been few prior studies on the effects of aging on solder cyclic stress-strain behavior of Bi-doped lead free solders.

In this chapter, effects of aging on the cyclic stress-strain behavior of Bi-doped lead free solders have been investigated. In this study, we have investigated the aging induced evolution (up to 6 months) of the cyclic stress-strain behavior of three new doped lead free solder materials—referred to as Ecolloy (SAC_R), CYCLOMAX (SAC_Q) and Innolot by vendors. Prior to testing, cylindrical uniaxial lead free solder test specimens were prepared and aged (preconditioned) at 125 °C for various aging times (0, 5, 10, 20, 30, 60, 90, and 180 days). The 0-day aging specimens represented non-aged samples, which were tested within a few minutes after solidification. After aging, the fabricated samples were subjected to strain controlled cyclic stress-strain loading (constant positive and negative strain limits) at room temperature (25 °C). In this chapter, all specimens were tested at a constant strain rate of 0.001 sec-^{1}. The nominal diameter of the uniaxial specimens in this work was 1.2 mm. The applied strain limits were ±0.005, and the gage length was chosen as 10 mm. In addition, at least 5 tests were conducted for each solder alloy and aging condition. For each set of cyclic stress-strain data, the four-parameter hyperbolic tangent empirical models (Eq. 3.4 & 3.5) have been used to fit the entire cyclic stress-strain curve. From the recorded cyclic stress-strain curves, the evolutions of the solder hysteresis loop area, plastic strain range, and peak load with aging have been characterized and empirically modeled. Either the loop area or the plastic strain range is often considered to be the fatigue damage driving force and widely used in fatigue life prediction models. The mechanical behavior of a solder test specimen is closely tied to its microstructure. Therefore, to better understand aging induced evolution of cyclic stress-strain behavior, the effects of aging on solder microstructure of a fixed region have been studied using SEM.

5.2 Cyclic Stress-Strain Response

Lead free solder alloys are used in industry for solder balls in lead free BGAs, CSPs, and flip chip die, as well as for solder pastes used in SMT processes. In this study, strain controlled cyclic testing has been performed on three different doped alloys: SAC_R, SAC_Q, and Innolot. Later, the results were compared with the conventional lead free SAC alloys to investigate the doping effect on cyclic properties. Water quenched (WQ) cooling profile used in the sample preparation. WQ samples have finer microstructures and better mechanical properties because of the fast cooling rate. Cyclic stress-strain curves were developed during the cyclic testing. For Example, figure 5.1 shows the first 10 cyclic stress-strain curves for a non-aged WQ SAC305 test specimen, and it has been found that the hysteresis loop did not change much. Figure 5.2 illustrates and compares how the hysteresis loop area changed with cycles at beginning for 5 non-aged WQ SAC305 samples. For the study of cyclic stress-strain behavior, the hysteresis loops were studied at the 10th cycle, when the loops tend to be more stable from one loop to the next. Figure 5.3 shows the cyclic stress-strain behavior for WQ SAC305 samples at no aging condition, and the plot contains 5 results tested at the same conditions. The results showed a high level of consistency and repeatability from one sample to another.

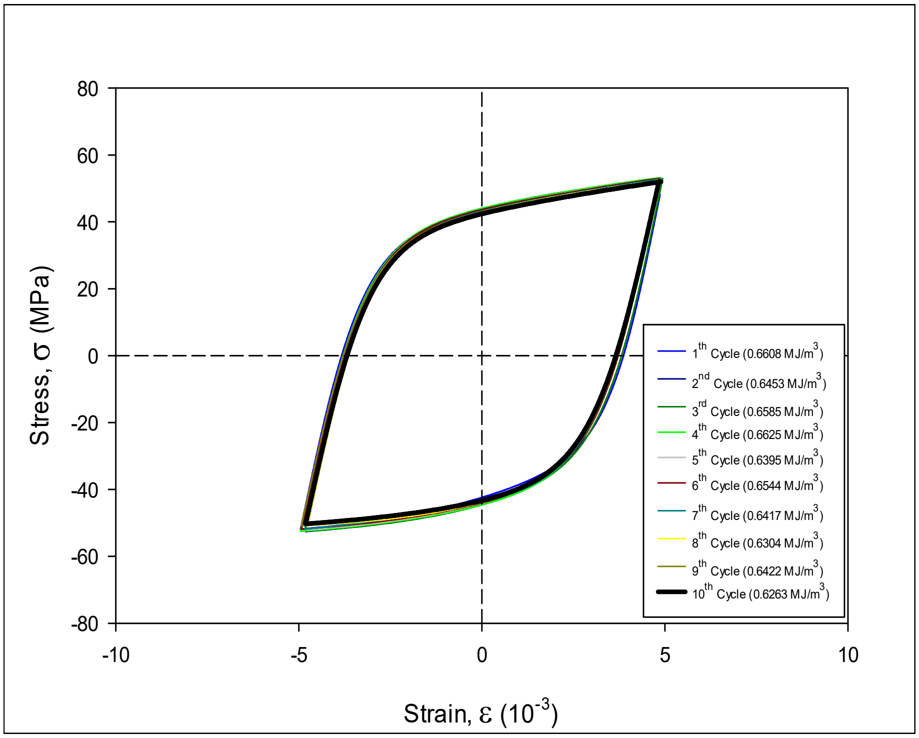

Figure 5.1 The First 10 Hysteresis Loops for a WQ SAC305 Sample (No Aging)

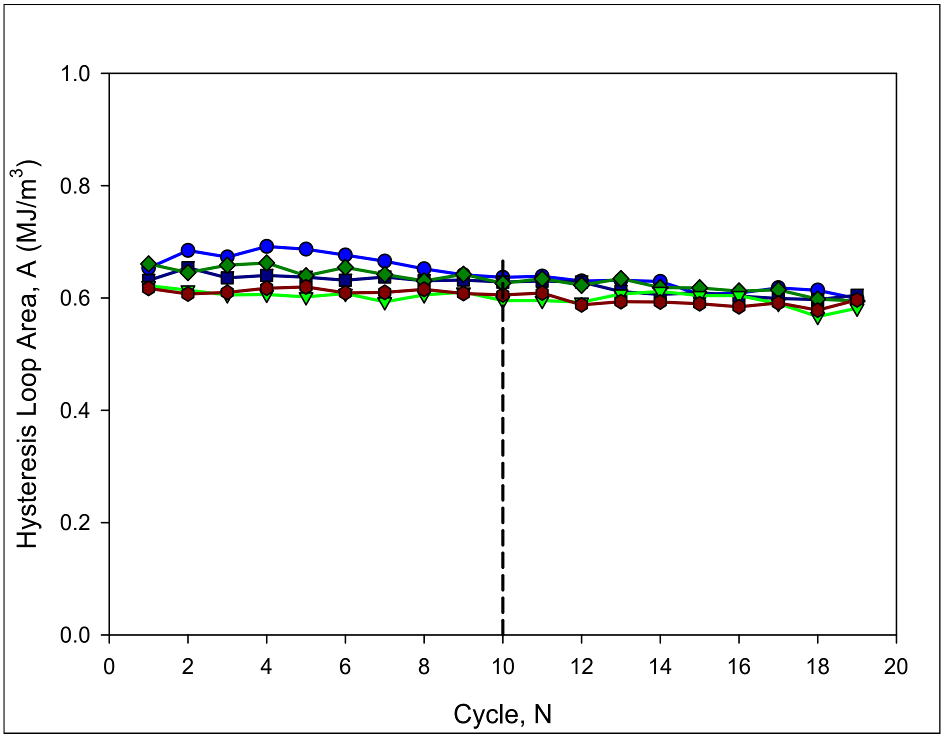

Figure 5.2 The Changes of Loop Area with Cycles for WQ SAC305 from 5 Tests

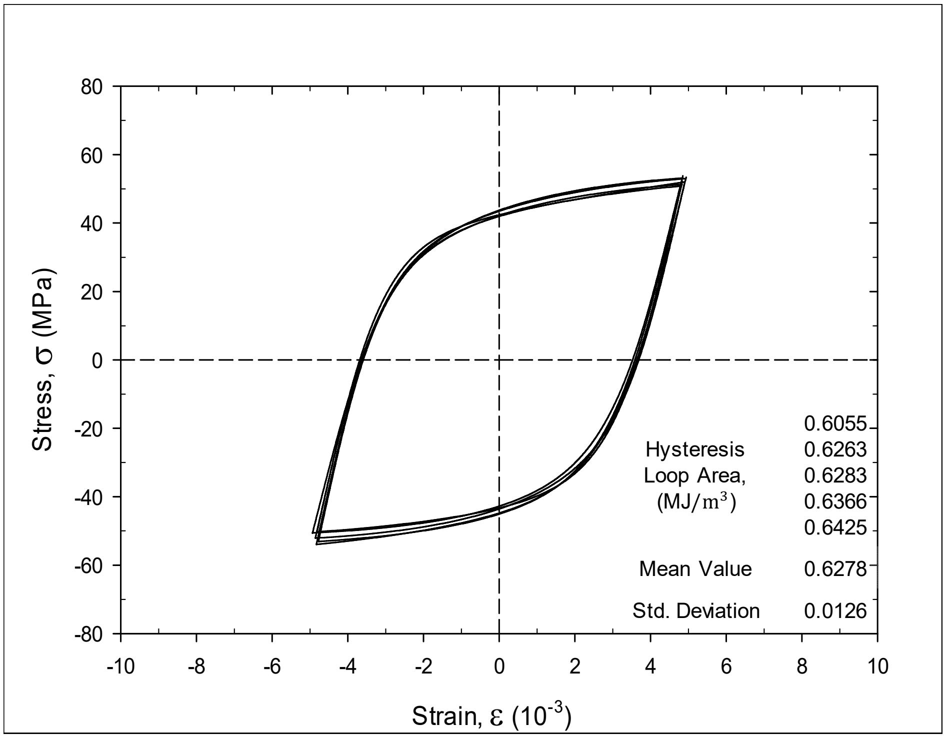

Figure 5.3 The Cyclic Stress-Strain Behavior for WQ SAC305 from 5 Tests (No Aging)

5.3 Cyclic Stress-Strain Behavior of Doped SAC Solder Alloy

In the present study, an initial investigation has been made on various doped SAC alloys subjected to strain limit controlled cyclic loading (no aging). Tests were performed on three different doped alloys: SAC_R, SAC_Q, and Innolot. Later, the results were compared with the conventional lead free SAC alloys to investigate the doping effect on cyclic properties. The strain controlled testing was performed with strain limits of ±0.005 and a strain rate of 0.001 sec^{-1}, and the testing temperature was 25 °C. Figure 5.4 illustrates the cyclic stress-strain plots of the non-aged samples of these doped alloys. From the processed cyclic stress-strain curves, the hysteresis loop areas were computed using the procedure described before in the previous section. Peak stresses and plastic strain ranges were also calculated as depicted in Figure 5.5. The peak stress is defined as the maximum stress during the cycle after reaching a stable condition. In this experiment, we considered the 10th cycle as a stable cycle. Using the same cycle for each case, plastic strain range was determined considering the distance between the two strain-axis intercepts on the graph. This range is actually equal to the total strain range minus the elastic strain range.

It is observed that both SAC305 and SAC_R have almost same hysteresis loop area, plastic strain range, and peak stress. It was experienced that a higher silver content increases the overall cyclic property by decreasing energy dissipation and damage accumulation when subjected to similar cycling conditions. However, there is no measurable silver content present in the SAC_R, yet, they are showing very similar properties like SAC305 because of the presence of Bi. Thus, we are getting the same cyclic stress-strain properties at lower cost.

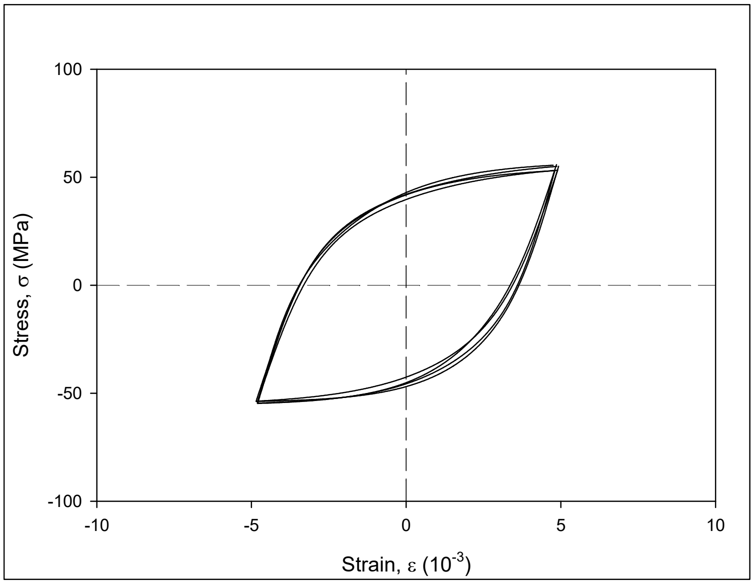
100
50
0
-50
-100
Stress, σ (MPa)
-10
-5
0
5
10
Strain, ε (10^-3)

(a) SAC_R

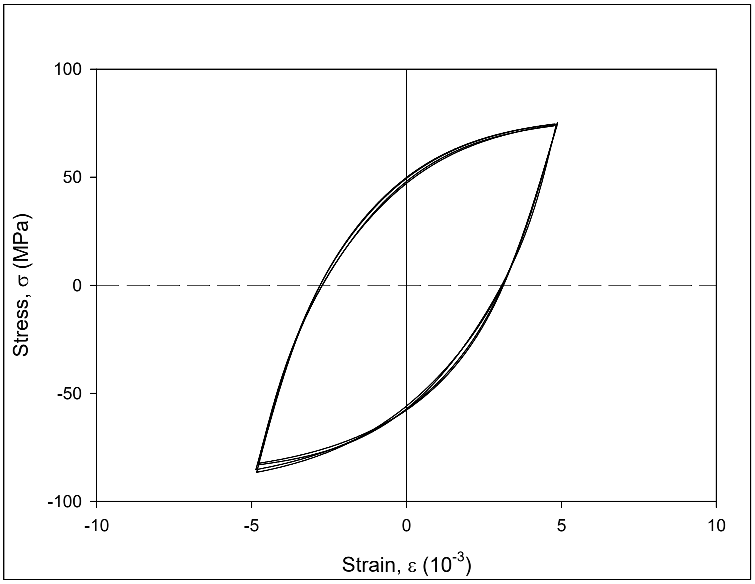
100
50
0
-50
-100
Stress, σ (MPa)
-10
-5
0
5
10
Strain, ε (10^-3)

(b) SAC_Q

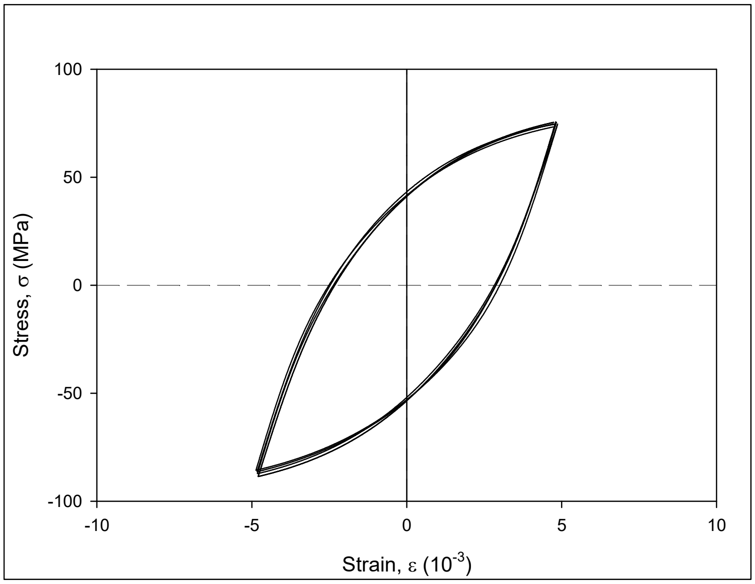

(c) Innolot

Figure 5.4 Hysteresis Loops for Cyclic Stress-Strain Testing of non-aged samples of a) SAC_R, b) SAC_Q, and c) Innolot.

It is also noticeable from figure 5.5 that Innolot has significantly better properties compared to the SAC305 and SAC_R. A six element Sn-Ag-Cu-Bi-Ni-Sb lead free solder alloy referred to as Innolot has been introduced by several solder vendors for enhanced reliability. Similar to the creep response, Innolot has been also proved to have better cyclic stress-strain and fatigue properties. Lastly, a close observation of figure 5.5 presents a significant finding in the case of SAC_Q which shows the superior cyclic properties among all of these lead free solder alloys. It is actually considered a Bi-doped SAC solder alloys where the amounts of Ag and Bi are 3.41 and 3.3 respectively.

Higher silver content alloys have decreased nonlinearity (plasticity) in their regular (non-cyclic) stress-strain curves as well as in cyclic stress-strain curves. Hence, decreasing plastic strain is related to the decreasing movement of dislocations and increasing cyclic stress is related to increasing resistance to dislocation motions. In summary, lower movement of dislocations and higher resistance to dislocation motion also imply higher fatigue properties. Moreover, the improved cyclic stress-strain properties might be attributed to the role of Bi on the morphology of the microstructure and distribution of dominant IMC (Ag_3Sn).

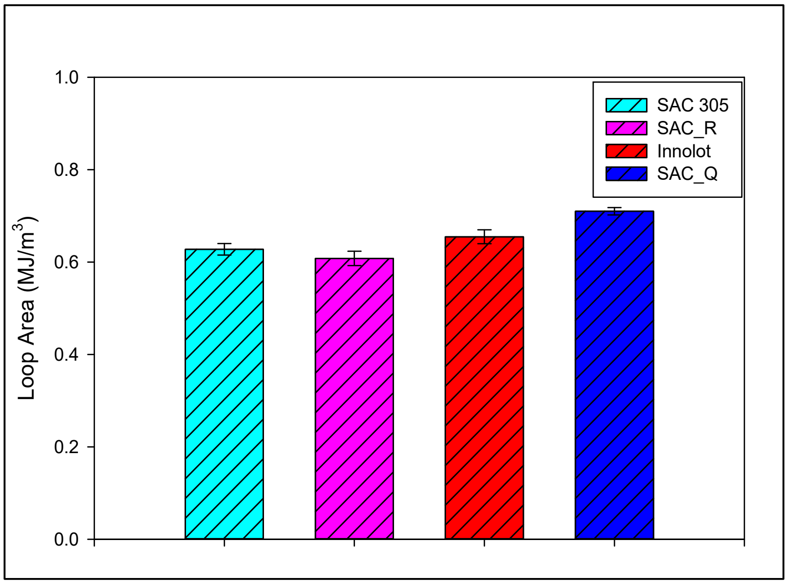

(a) Hysteresis Loop Area

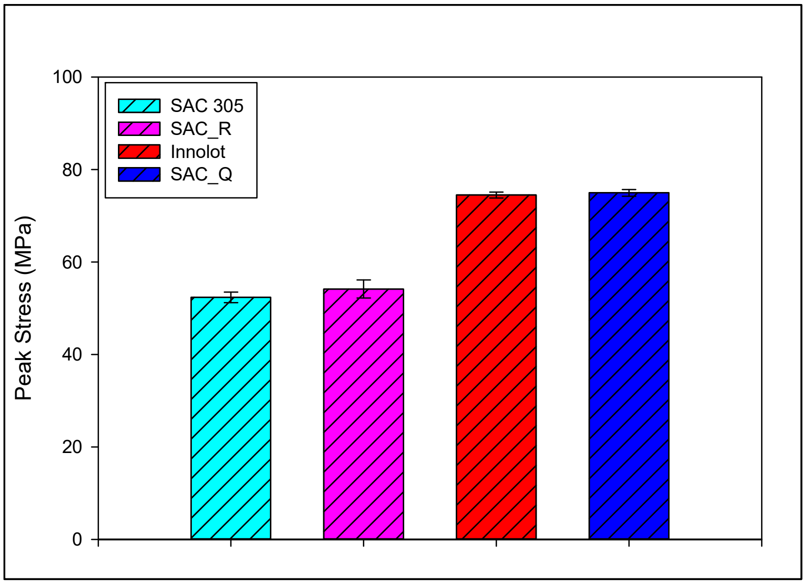

(b) Peak Stress

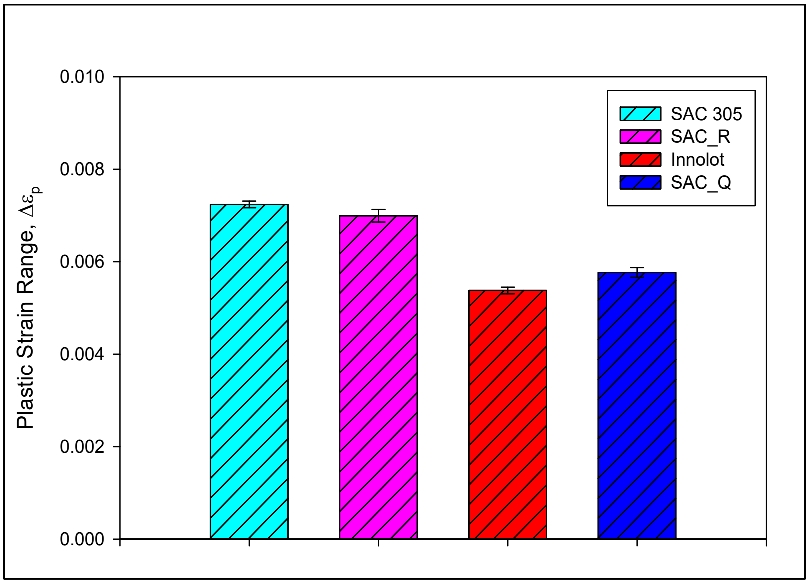

(c) Plastic Strain Range

Figure 5.5 Comparison of Cyclic Properties of Three Different Doped SAC Solder Alloys along with SAC305

5.4 Evolution of the Hysteresis Loop with Aging

Cyclic testing has also been performed on the aged specimens of these doped alloys. Samples were subjected to prior aging to investigate the aging-induced cyclic stress-strain behavior of these doped alloys. Water quenched cooling profile has been used in the sample preparation to yield finer microstructures, thus, we can get the upper limit of mechanical properties. After accomplishing the solidification process, the samples were aged isothermally at 125 °C for various aging durations up to 180 days of aging. In this study, we calculated the hysteresis loop area at the 10th cycle as mentioned earlier, as the loops after some initial cycles tend to be more stable from one loop to the next. Each cyclic stress-strain graph for a particular aging duration consists of at least five different samples tested at the same testing conditions. The results showed a remarkable consistency and repeatability from one sample to another.

From the recorded cyclic stress-strain curves, the areas of the hysteresis loops were calculated using the procedure outlined above. The hysteresis loop area can also be regarded as the plastic strain energy density dissipated per cycle, which is related to the damage accumulation in the specimen at that cycle. In addition, the plastic strain ranges and peak stresses were also determined. The plastic strain range is equal to the total strain range minus the elastic strain range, which is the distance between the two strain axis intercepts on the graph. The peak stress is simply the maximum stress recorded during the cycle. The hysteresis loop area and plastic strain range are typically considered the most two important factors for fatigue damage. Therefore, most of the models predict solders' fatigue life based on either the plastic strain energy density (hysteresis loop area) or the plastic strain range. Morrow model, Syed model, Energy partitioning model, and Darveaux model are the most prominent fatigue models that consider the plastic strain energy density as the fundamental mechanism responsible for inducing damage. These models are typically categorized as energy-based models. On the other hand, some other fatigue life prediction models are based on the plastic strain. Such models have been proposed by Coffin-Manson, Solomon, Engelmaier, and Miner.

Elevated temperature aging (125 °C) induced evolution of the hysteresis loop has been characterized for three lead free solders, i. e., SAC_R, SAC_Q and Innolot. Figure 5.6 illustrates some example plots of the cyclic stress-strain behavior for SAC305 samples that were subjected to elevated temperature aging. Again, each plot contains five results tested at the same conditions for a particular aging duration, and the results were consistent and repeatable. It has been observed that the shape and size of cyclic stress-strain curves changed a lot during aging. The most noticeable changes occurred during the first 5 days of aging, with slower changes occurring for longer aging times. For aging times greater than 30 days, the hysteresis loop changes were very small. The evolution of the hysteresis loop with elevated temperature aging for SAC305 solder is shown on a single plot in Figure 5.7. In this plot, a typical hysteresis loop was chosen to represent the results of five tests for each aging duration. Similar analysis has been done for SAC_R (Figure 5.8 and Figure 5.9), SAC_Q (Figure 5.10 and Figure 5.11) and Innolot (Figure 5.12 and Figure 5.13) with elevated temperature aging.

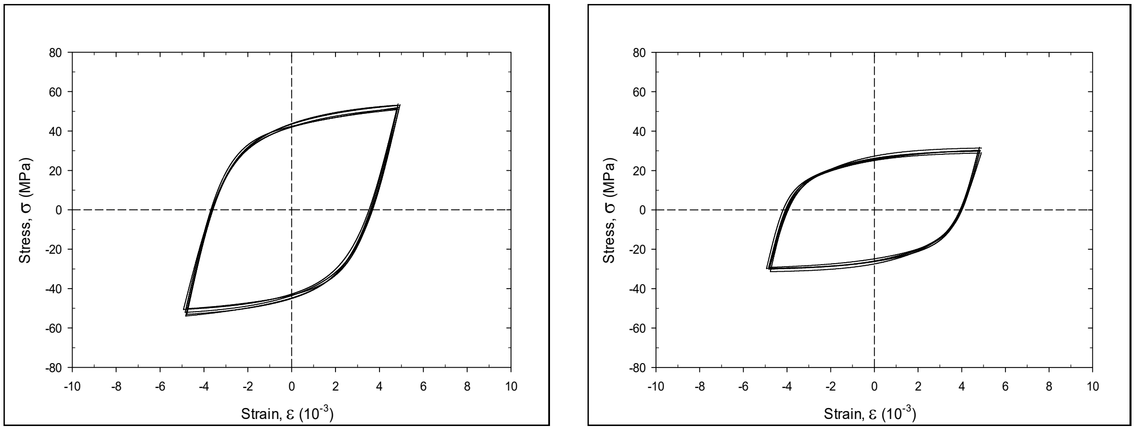

(a) No Aging (b) 5 Days of Aging

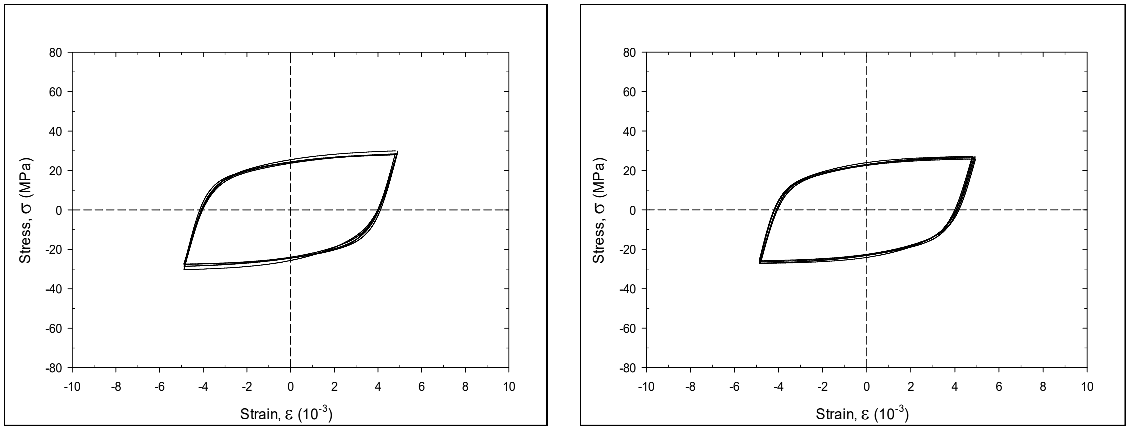

(c) 10 Days of Aging (d) 30 Days of Aging

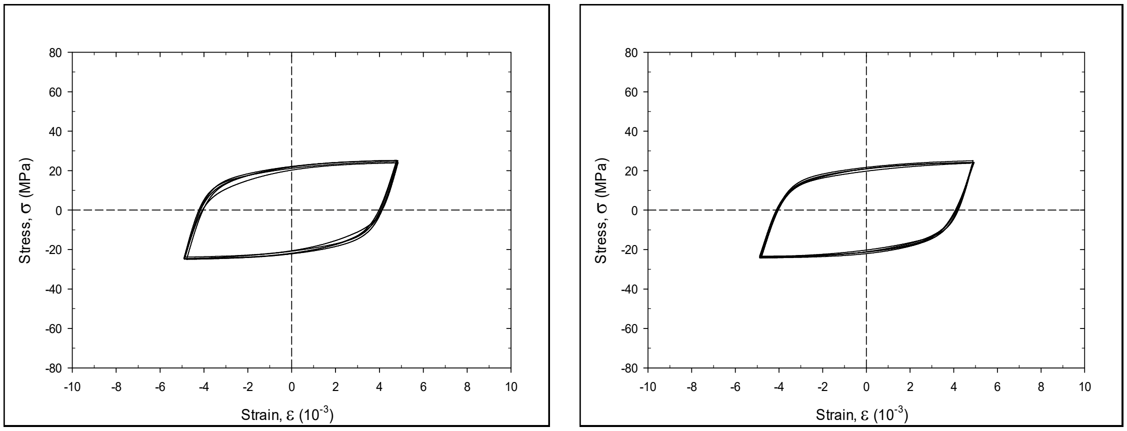

(e) 60 Days of Aging (f) 90 Days of Aging

Figure 5.6 Hysteresis Loops for Cyclic Stress-Strain Testing of SAC305 (Aging at 125 °C)

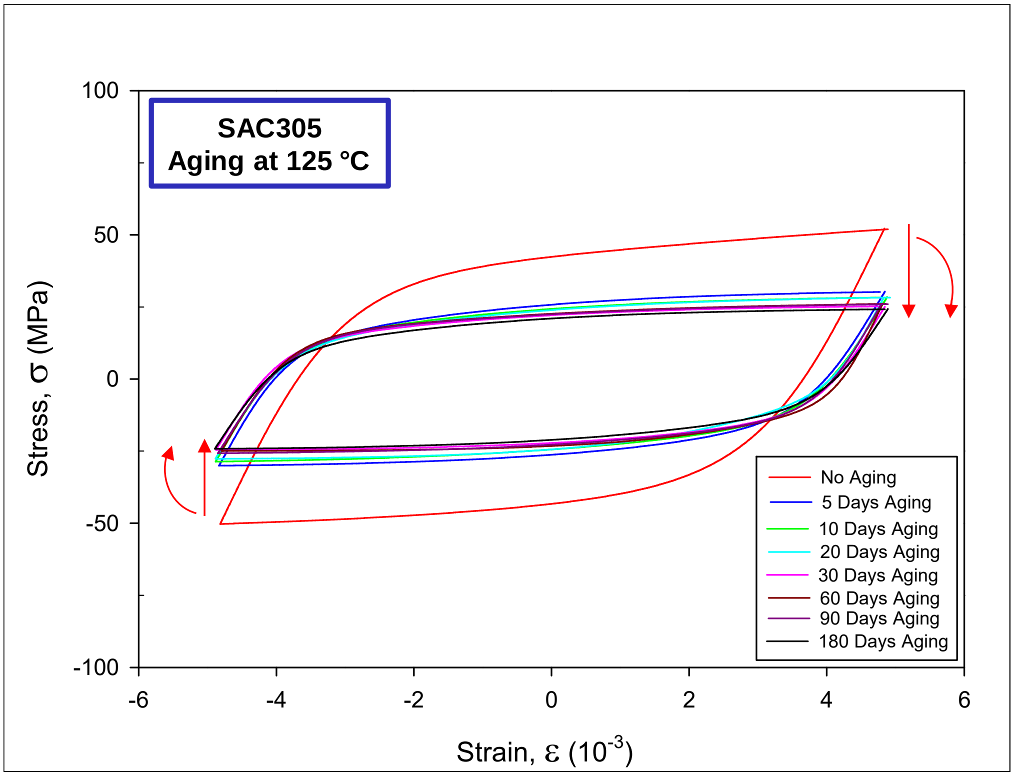

Figure 5.7 Aging Induced Evolution of Hysteresis Loop for SAC305 (Aging at 125 °C)

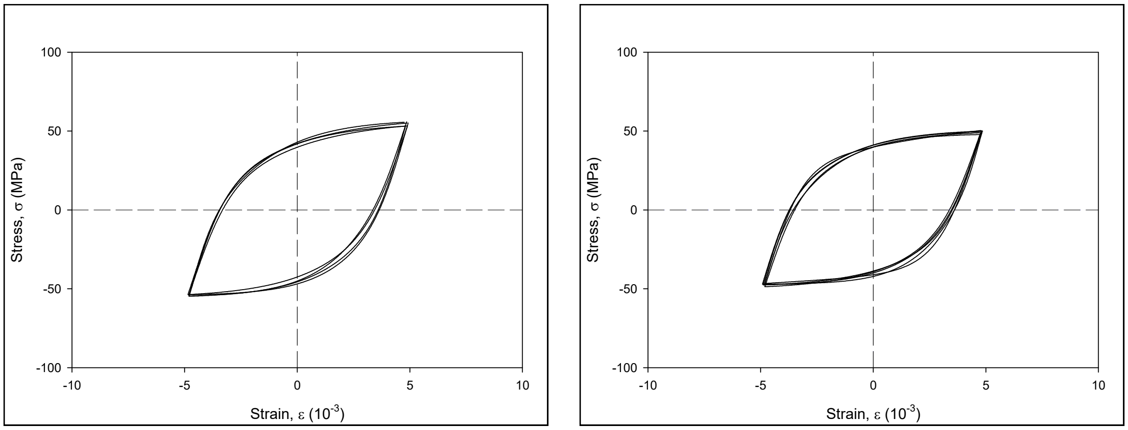

(a) No Aging (b) 5 Days of Aging

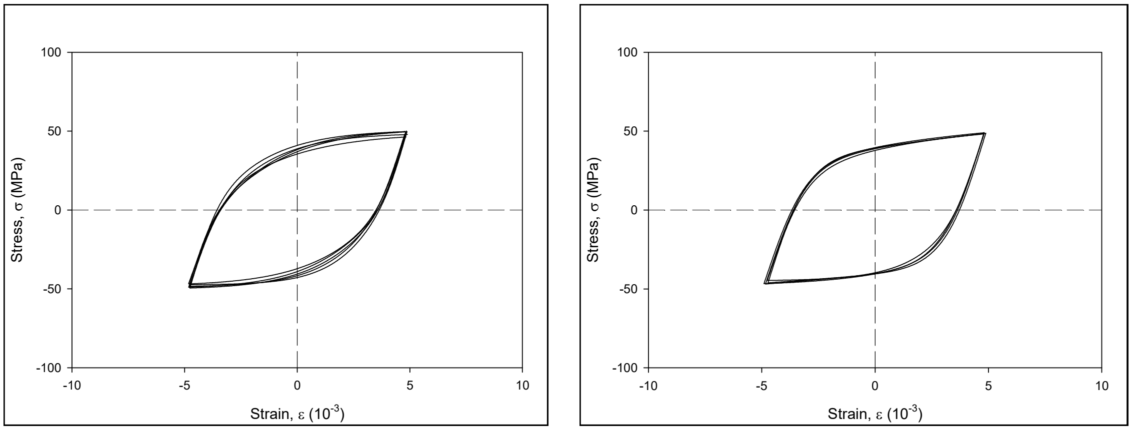

(c) 10 Days of Aging (d) 30 Days of Aging

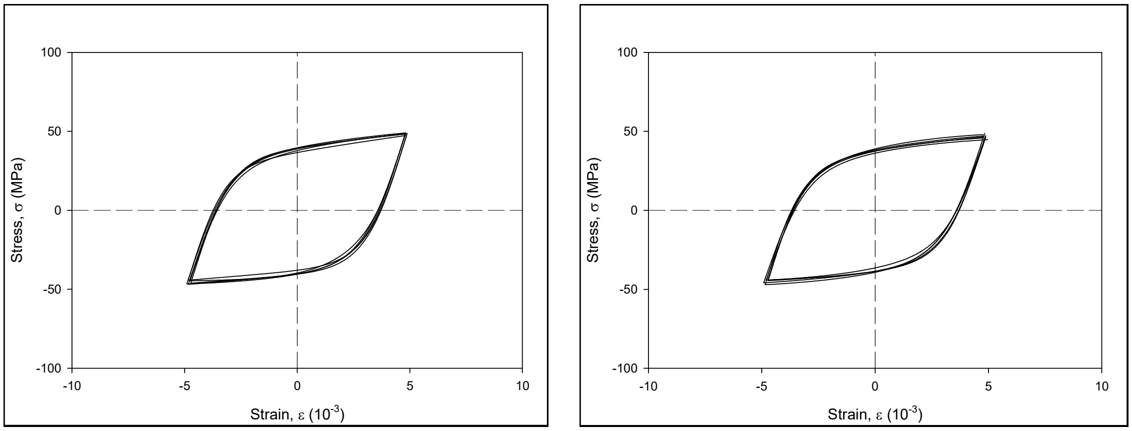

(e) 60 Days of Aging (f) 90 Days of Aging

Figure 5.8 Hysteresis Loops for Cyclic Stress-Strain Testing of SAC_R (Aging at 125 °C)

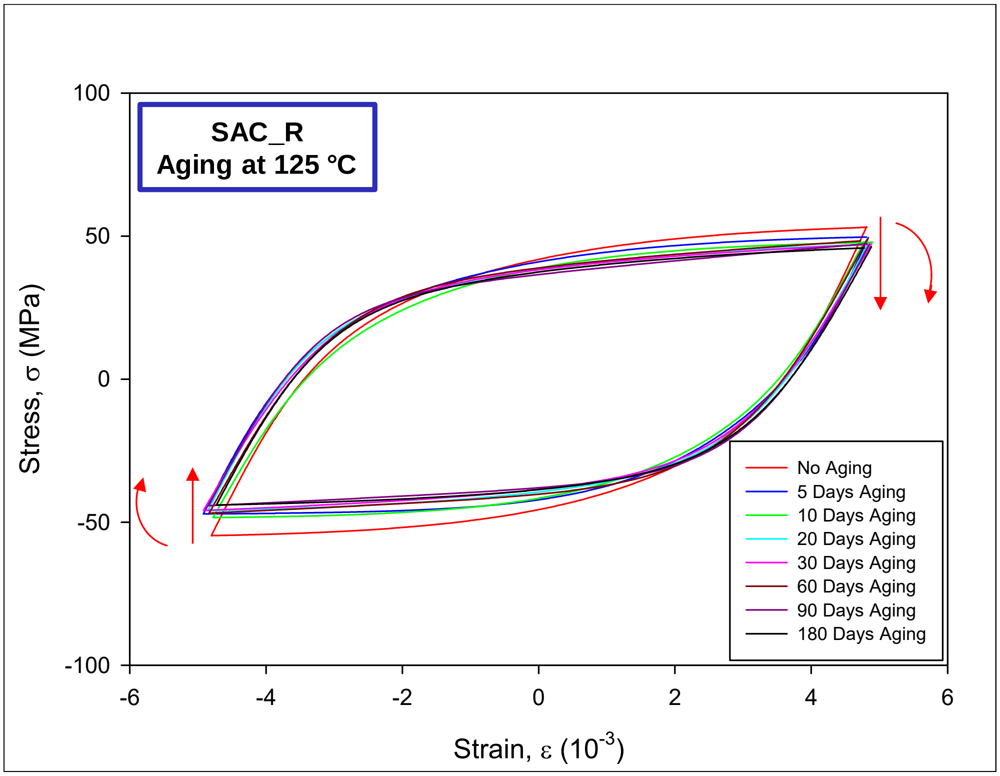

Figure 5.9 Aging Induced Evolution of Hysteresis Loop for SAC_R (Aging at 125 °C)

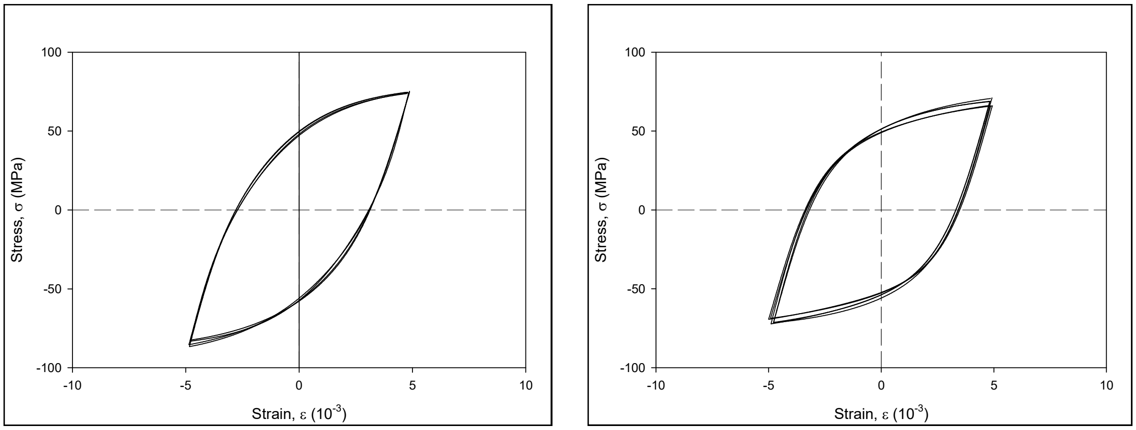

(a) No Aging (b) 5 Days of Aging

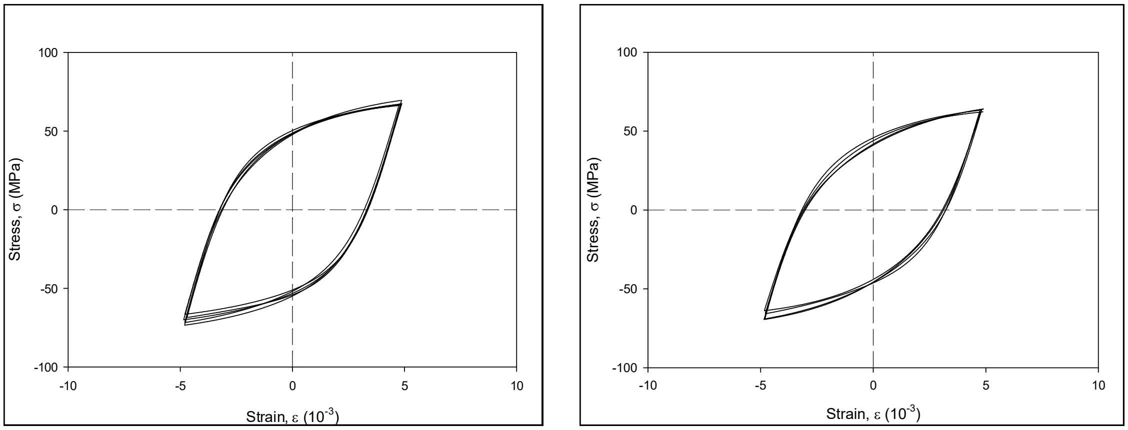

(c) 10 Days of Aging (d) 30 Days of Aging

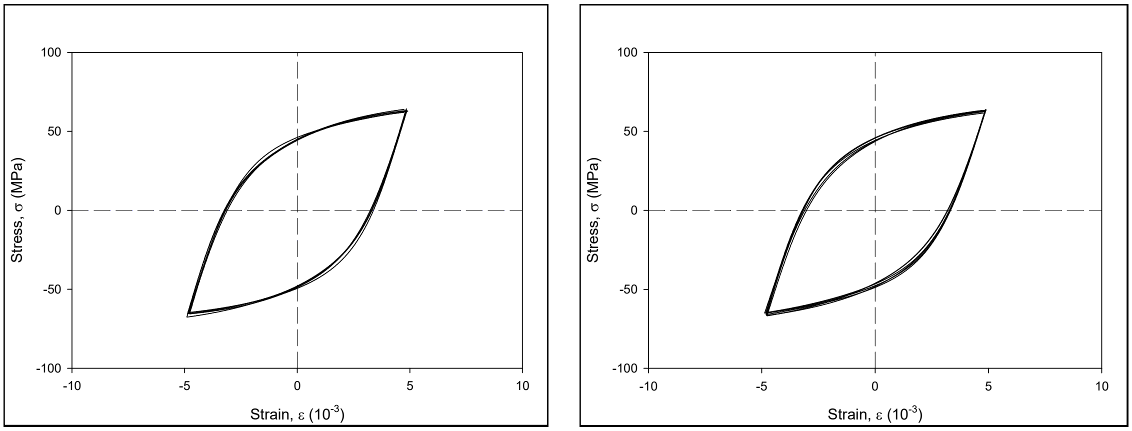

(e) 60 Days of Aging (f) 90 Days of Aging

Figure 5.10 Hysteresis Loops for Cyclic Stress-Strain Testing of SAC_R (Aging at 125 °C)

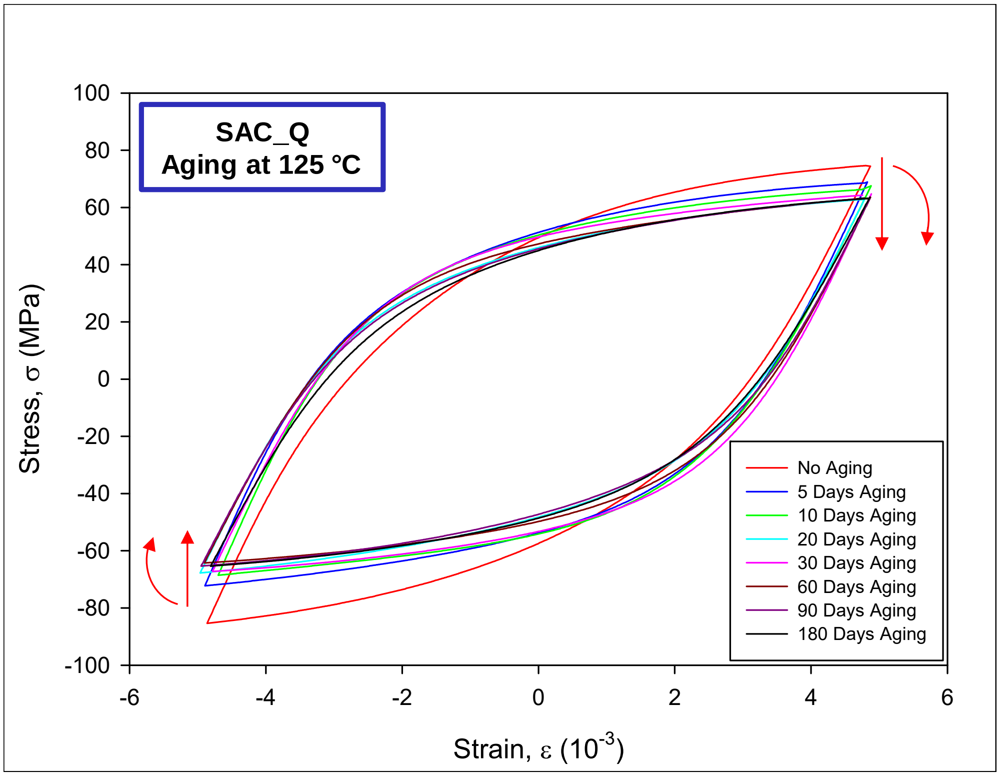

Figure 5.11 Aging Induced Evolution of Hysteresis Loop for SAC_R (Aging at 125 °C)

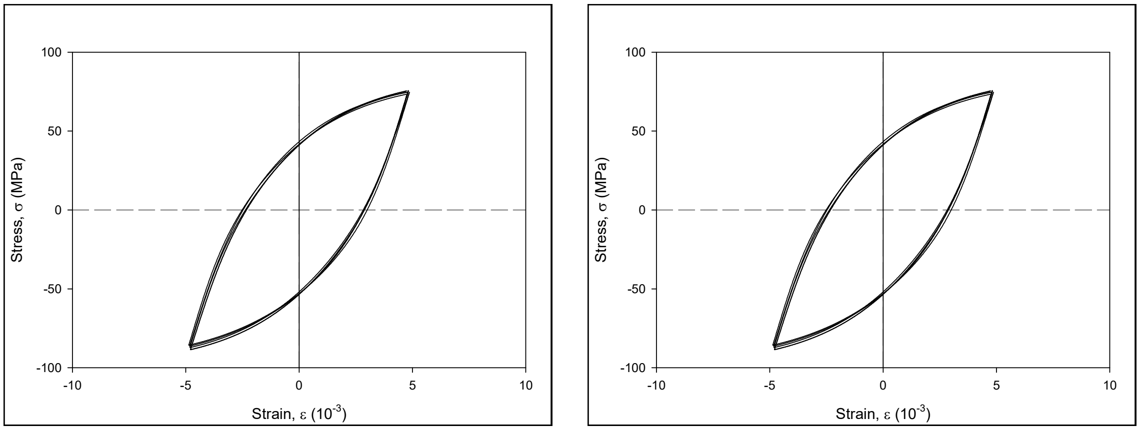

(a) No Aging (b) 5 Days of Aging

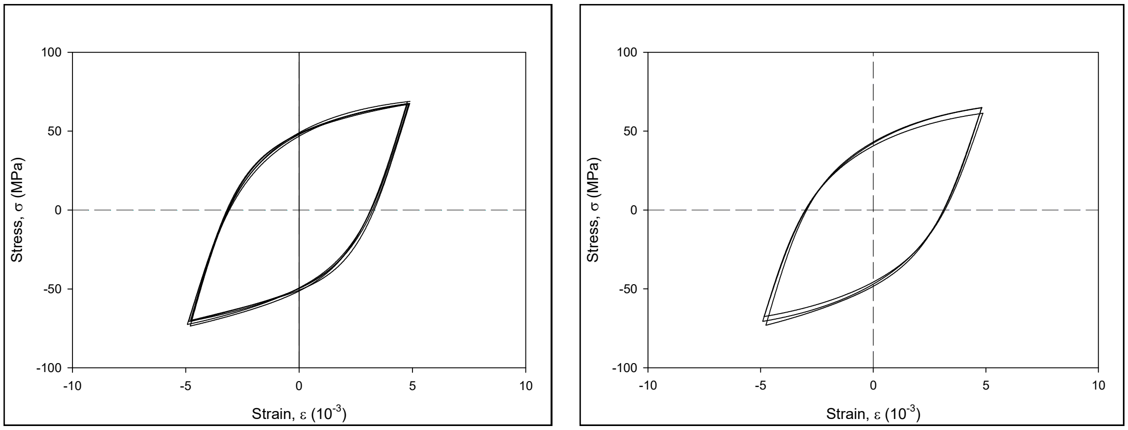

(c) 10 Days of Aging (d) 30 Days of Aging

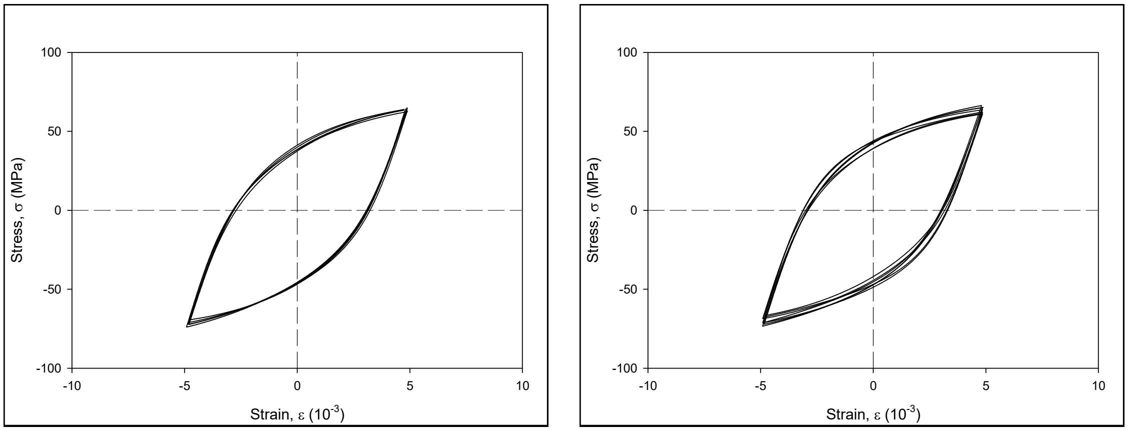

(e) 60 Days of Aging (f) 90 Days of Aging

Figure 5.12 Hysteresis Loops for Cyclic Stress-Strain Testing of Innolot (Aging at 125 °C)

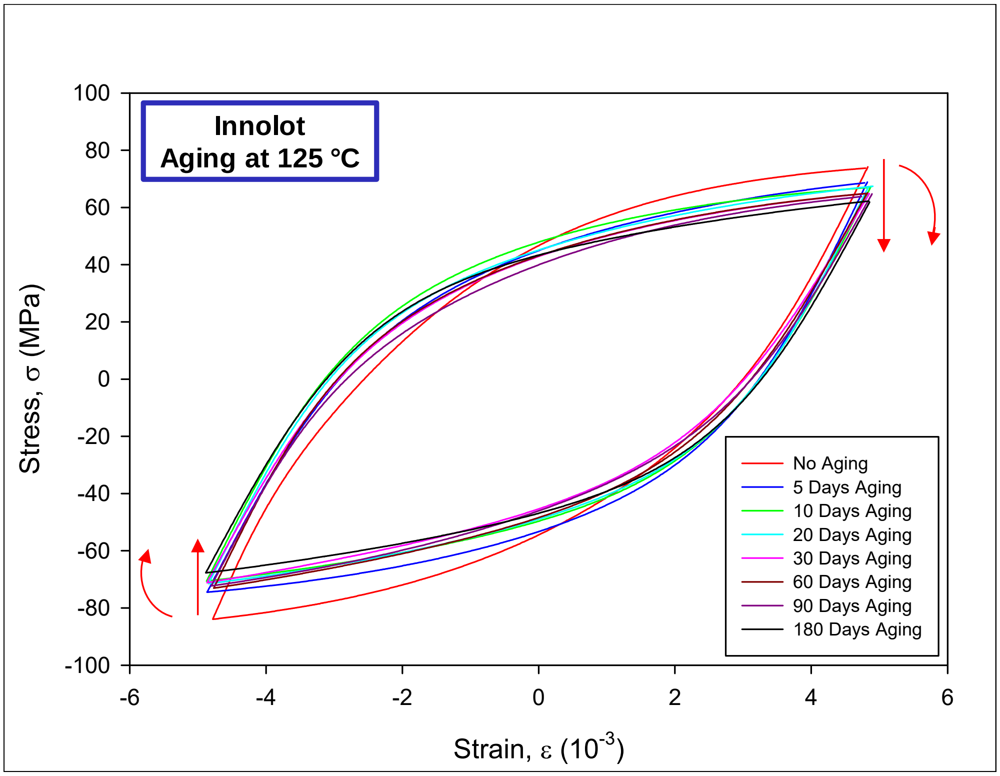

Figure 5.13 Aging Induced Evolution of Hysteresis Loop for Innolot (Aging at 125 °C)

The evolution of the hysteresis loops with aging for SAC_Q, SAC_R, and Innolot solder are shown on a single plot in Figure 5.9, 5.11, and 5.13 respectively. In the case of SAC305, the most notable changes occurred during the first 5 days of aging. And after 10 days of aging, the hysteresis loops were not changing significantly compared with 5 days of aged samples results. After 20 days aging, we got a much stable hysteresis loop indicating very less aging induced evolution. However, In the case of all doped alloys, it has been observed that the cyclic stress-strain curves do not have any significant changes after 5 days of aging. And we got stable hysteresis loops just after the 5 days of aging. We have performed further tests up to 6 months aging to observe the long term aging effect on these doped alloys.

5.5 Breakdown of the Evolution

The aging induced evolutions of the peak stress, hysteresis loop area, and plastic strain range for SAC_Q, SAC_R, and Innolot are illustrated in Figures 5.12, 5.13, and 5.14, respectively. The results of SAC305 have also been included in these figures for comparison purpose. Morrow hypothesized that on the microscopic level, cyclic stress is mostly affiliated to the ability to resist the movements while the cyclic plastic strain is associated with the dislocation movements. From these graphs, it is observed that the hysteresis loop area and peak stress reduced with the increased aging times, whereas the trend is opposite in the case of plastic strain range. The increment of plastic strain range with the increased aging times means more dislocation movements occurred during the test. Aging also caused a decrease of the peak stress, which indicates the specimen was losing the ability to resist the movements of dislocations. The decrease of the hysteresis loop area with increased aging suggests that energy dissipation was mitigated with aging. In the case of all three doped alloys, very little changes of all three parameters occurred within the first 5 days of aging and no significant changes occurred after that period. On the other hand, in the case of SAC305, dramatic changes have been observed in all three parameters just after the 5 days of aging. As there were less significant changes in all three parameters with the increase of aging time, these doped alloys are actually much more resistant to the aging-induced evolution compared to the conventional SAC solder materials.

The effects of the test temperature on the applied stress vs. time curves during the creep deformations are shown in Figure 5.19. Although the applied load was kept constant during the creep tests, the applied stress under the indenter tip decreased with time due to the contact area continually increasing. The applied stresses decreased with increasing temperature, since the indentation depth and thus the contact area increased with test temperature.

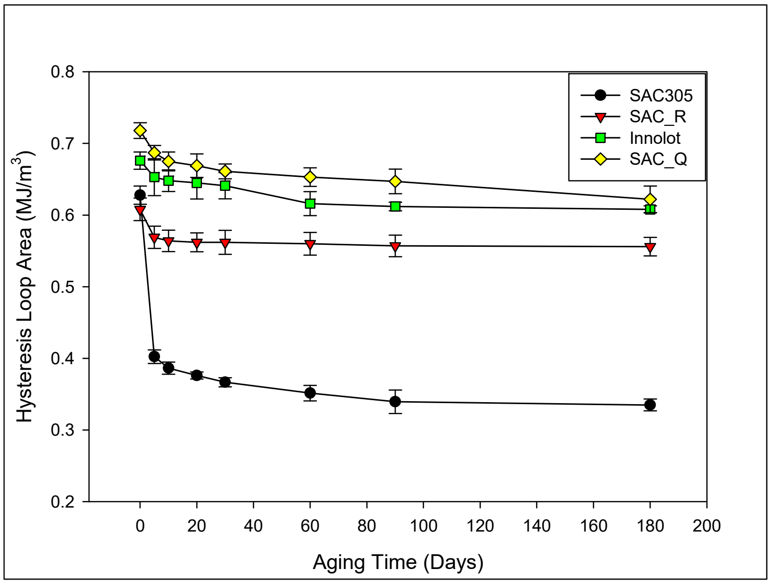

(a) Hysteresis Loop Area

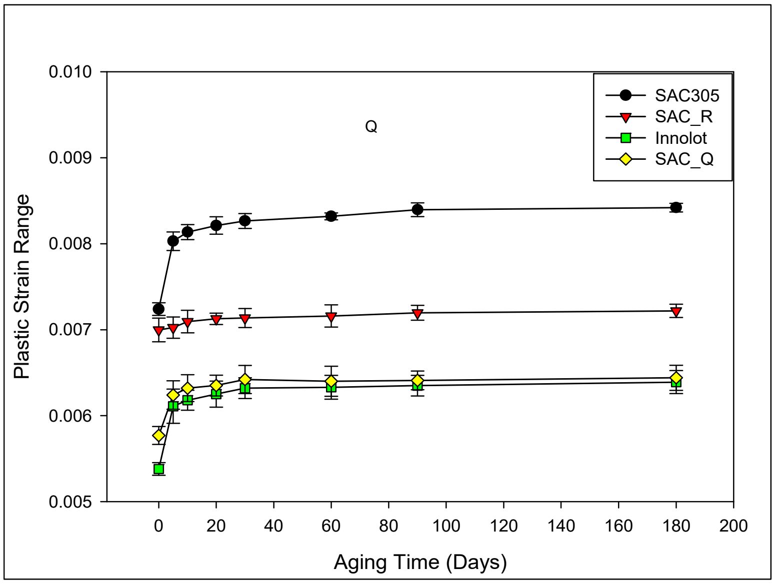

(b) Plastic Strain Range

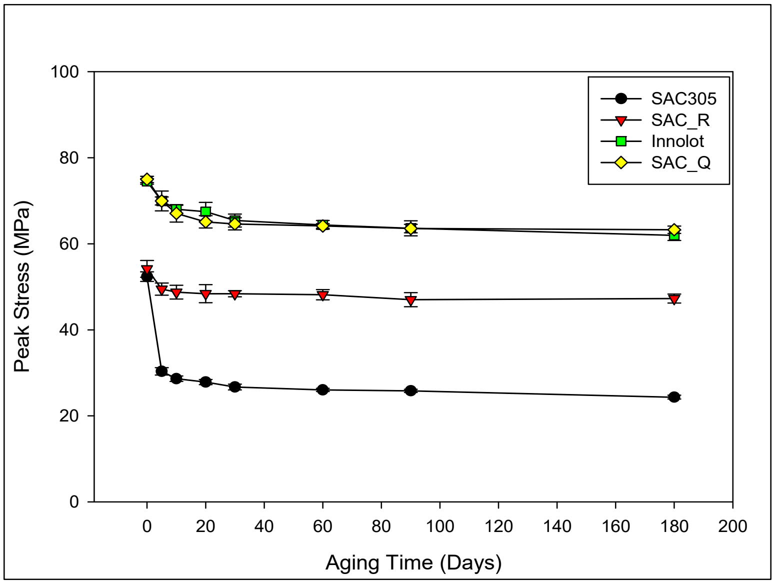

(c) Peak Stress

Figure 5.14 Variation of a) Hysteresis Loop Area, b) Plastic Strain Range, and c) Peak Stress with Aging

5.6 Summary and Discussion

In this chapter, we have conducted an investigation on the effects of aging on the cyclic stress-strain behavior of the doped lead free solders. Using a micro tester machine equipped with a newly designed gripping fixture especially for cylindrical specimen has been used for uniaxial cyclic testing. For preparing the testing specimens, water quenched (WQ) solidification profile has been used, which is expected to attain the characteristics of fine microstructures and thus lead to the upper limits of the mechanical properties of each alloy. Cylindrical uniaxial test specimens of water quenched (WQ) doped solder alloys have been formed in circular cross-section glass tubes using a vacuum suction process. Specimens aged at 125 °C for different aging times (0-6 months) have been subjected to cyclic (tension/compression) mechanical loading at room temperature under strain controlled cycling. After fitting the cyclic stress-strain curves from the machine, the evolution of the cyclic stress-strain behavior with aging has been characterized in terms of peak stress, hysteresis loop, and plastic strain range. The results for the doped solders have also been compared with the standard lead free alloy (e.g. SAC 305).

From the experimental results, we observed that SAC_R showed similar properties as the SAC305 despite the lack of any measurable silver content. Therefore, we are getting the same cyclic stress-strain properties at lower cost. We also found that Innolot has significantly better properties than SAC305 and SAC_R. Similar to the tensile and creep response, Innolot has also been proved to have better cyclic stress-strain and fatigue properties. Lastly, SAC_Q showed the superior cyclic properties among all of these lead free solder alloys. The improved cyclic stress-strain properties might be attributed to the role of Bi on the morphology of the microstructure and distribution of dominant IMC. We also observed that the hysteresis loop area, plastic strain range, and peak stress of conventional SAC alloys dropped while the plastic strain range increased with the increased aging time. All changes were most dramatic within the first 5 days of aging. On the other hand, in case of doped SAC alloys, no significant changes have been noticed during the aging period. In summary, these doped alloys have been proved as promising solder materials for use in thermal and/or mechanical loading not only because of improved cyclic properties but also for being strongly resistant to aging-induced evolution.

CHAPTER 6

EVOLUTION OF MECHANCIAL PROPERTIES IN LEAD FREE SOLDERS DURING CYCLIC LOADING

6.1 Introduction

While it has been known that the reversal of inelastic strain can change the stress-strain behavior of materials (Bauschinger effect), there have been very few prior studies on how the cycling changes the microstructure and degrades the mechanical properties of lead free solders during fatigue testing. In this chapter, we have explored the effects of mechanical cycling on the constitutive behavior (stress-strain and creep) of SAC305 and SAC_Q (SAC+Bi) in lead free solders during fatigue loading. The evolution of the cyclic stress-strain behavior (hysteresis loop area, plastic strain range, and peak stress) during the cycling tests has also been studied. Cylindrical uniaxial SAC305 and SAC_Q lead free solder test specimens have been prepared. The uniaxial specimens had a nominal diameter of 1.2 mm, and the gage length was 5 mm in this work. All the tests were conducted at room temperature (25 ºC) at a strain rate of $\dot{\varepsilon} = 0.002$ sec^{-1}. Strain controlled method has been used in the cyclic testing, and the cyclic strain limits were ±0.01. To study the evolution of the cyclic stress-strain behavior, the specimens have been subjected to cyclic stress/strain loading at room temperature (25 ºC) until fatigue failure. The cyclic stress-strain curves at after various durations of cycling have been examined. From the recorded cyclic stress-strain curves, the evolution of the solder hysteresis loops with number of cycles has been characterized. Also, the duration of cycling on the hysteresis loop area (plastic strain energy density), plastic strain range, and peak load have been studied.

To study the effects of cycling on damage accumulation and degradation of the constitutive behavior of SAC305 and SAC_Q, uniaxial samples have been prepared and subjected to various durations of prior isothermal mechanical cycling (e.g. 0, 50, 100, 300, 600, 900, 1200 cycles) that were below the fatigue life of the material. These various amounts of prior cycling served to impart various levels of fatigue damage to the samples. The same strain ranges of ε = ±0.01 and ε = ±0.005 were used for SAC305 and SAC_Q, respectively. After cycling (damage accumulation), the specimens were subjected to stress-strain or creep testing. After fitting the experimental data from mechanical testing, we have been able to characterize the cycling induced evolution of several mechanical properties of SAC305 and SAC_Q lead free solders. The goal of the study is to explore damage accumulation that occurs during fatigue testing.

6.2 Evolution of Cyclic Stress-Strain Curves

To study the evolution of the cyclic stress-strain behavior with cycling, the specimens have been subjected to cyclic strain loading (±0.01) at room temperature until fatigue failure occurred. Figure 6.1 shows a typical result for a SAC305 sample that was cycled with a total strain range of ε = ±0.01. The hysteresis loops for selected cycles (N = 1, 50, 100, 200, 300…, 1200) are indicated. It is clear that the peak stress and hysteresis loop size evolve dramatically during the test. For example, the fall of the peak stress is shown in Figure 6.2. This response is typically divided up into three regions. Initially, the peak stress drops rapidly (primary region), followed by a steady state (secondary) region of constant slope. The curve then enters a tertiary stage, where specimen fracture occurs. The fatigue life is typically defined as the number of cycles needed to cause a preset drop in the peak stress (preset load drop). In this work, we selected a 50% drop to define failure.

With the selected strain range, the fatigue life of the SAC305 samples was approximately 1200 cycles.

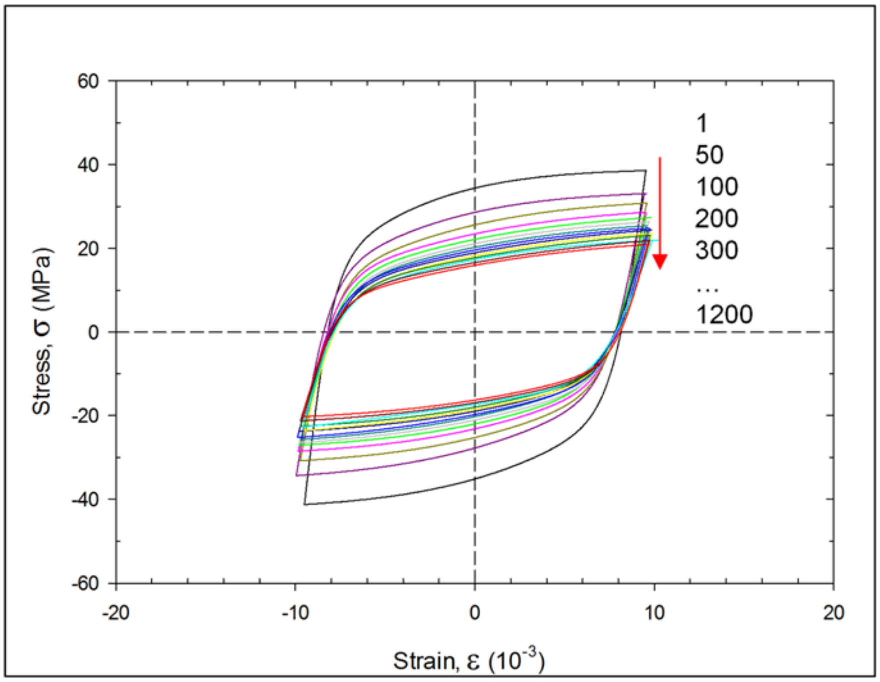

Figure 6.1 Evolution of the cyclic stress-strain curves during a fatigue test (SAC305)

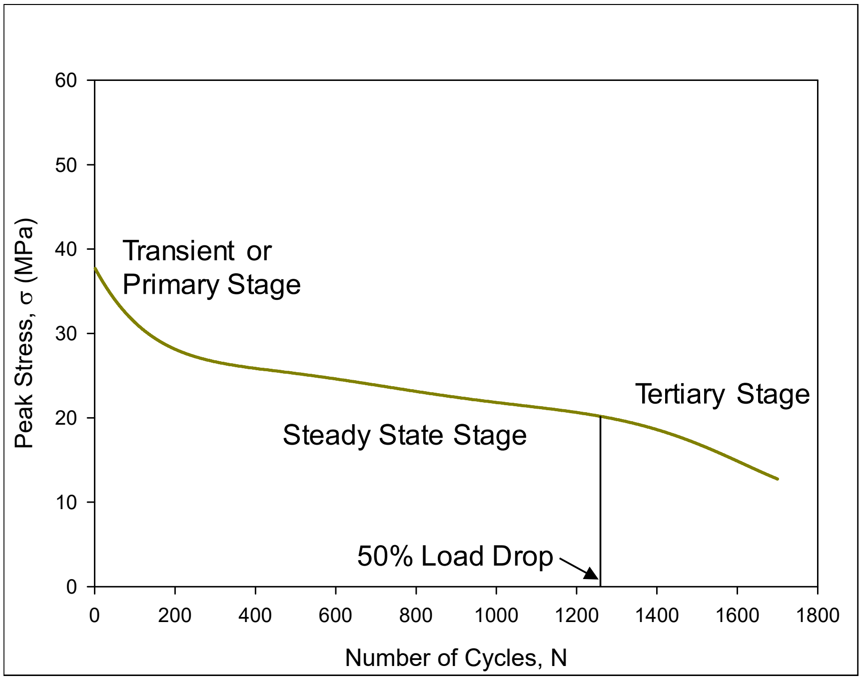

Figure 6.2 Drop of the peak stress during a fatigue test (SAC305)

For each fatigue test, the recorded hysteresis loops were processed at several cycle counts (N = 0, 50, 100, 300, 600, 900, and 1200 cycles) as described above, and hysteresis loop area, peak stress, and plastic strain range were calculated. The numerical results (averages for three tests) are shown in Table 6.1. It can be seen that the plastic strain (distance between horizontal axis intercepts) remains essentially constant during the cycling. Thus, the reduction in loop area is caused mainly by the reduction in peak stress as the strength of the material is degraded by damage accumulation in the specimen. For SAC305, the reductions in peak stress and hysteresis loop area were 48% and 56%, respectively, for the 1200 applied cycles.

Table 6.1 Cyclic Induced Changes of hysteresis loop area, peak stress, and plastic strain range (SAC305)

Cycling Duration (Cycles)	Loop Area (MJ/m3)	Peak Stress (MPa)	Plastic Strain Range (%)
1	1.16	38.65	1.65
50	0.88	33.18	1.63
100	0.80	30.62	1.61
300	0.71	27.28	1.59
600	0.62	24.71	1.59
900	0.57	23.10	1.61
1200	0.51	20.18	1.61

Figure 6.3 shows analogous results for the cyclic stress strain evolution of a typical SAC_Q sample that was cycled with a total strain range of $\varepsilon = \pm 0.005$. Again, it is observed that the peak stress and hysteresis loop size evolve dramatically during the test, while the plastic strain range remains almost constant. The numerical results (averages for three tests) are shown in Table 6.2. For SAC_Q, the reductions in peak stress and hysteresis loop area were both 54%.

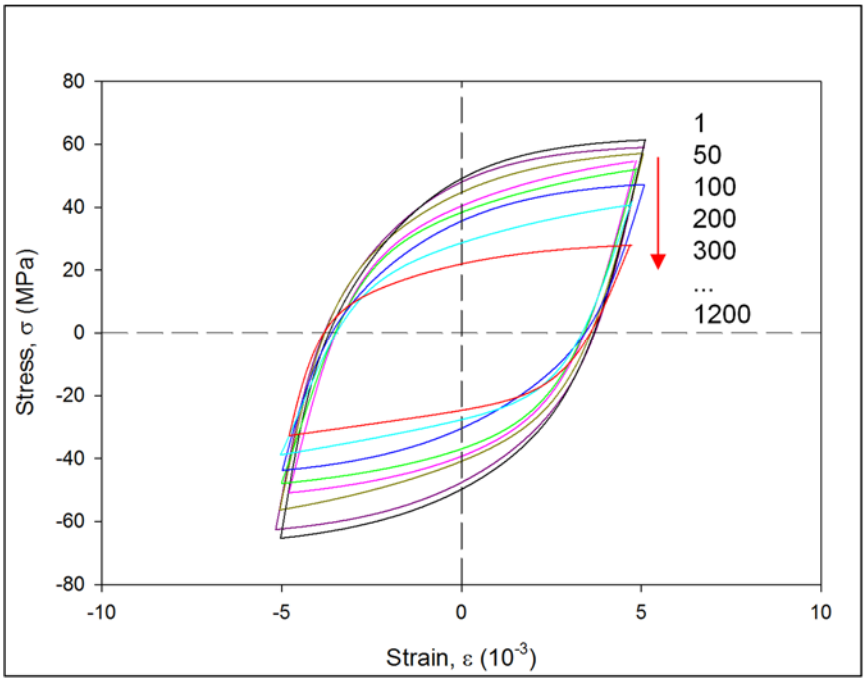

Figure 6.3 Evolution of the cyclic stress-strain curves during a fatigue test (SAC_Q)

The numerical values for SAC305 and SAC_Q in Figs. 9 and 11 cannot be directly compared since different applied strain ranges were used for the two materials resulting in different values of the initial hysteresis loop size and initial plastic strain range during the first cycle. In order to directly compare the performance of the materials, it is necessary to know the controlling parameter for fatigue damage accumulation. The choice of this parameter is still often considered an open question. However, it regularly taken to be the hysteresis loop area (ΔW (Morrow fatigue model) or the plastic strain range (Coffin-Manson fatigue model). In our future work, we are considering additional applied total strain ranges for both materials, and attempting to match the amount of damage applied during the first cycle (as modeled using either ΔW or the plastic strain range). With such an approach, we will be in a better position to compare the observed degradations and damage accumulations for the two materials.

Table 6.2 Cyclic Induced Changes of hysteresis loop area, peak stress, and plastic strain range (SAC_Q)

Cycling Duration (Cycles)	Loop Area (MJ/m3)	Peak Stress (MPa)	Plastic Strain Range (%)
1	0.71	61.39	0.58
50	0.60	57.56	0.59
100	0.54	54.38	0.59
300	0.51	49.27	0.60
600	0.46	46.62	0.61
900	0.40	40.45	0.62
1200	0.33	28.06	0.62

6.3 Evolution of Stress-Strain and Creep Behaviors

The next step of the study was to investigate the effects of the damage accumulation caused by mechanical cycling on the degradations of the tensile stress-strain and creep behaviors of the lead free alloys. Uniaxial samples were prepared as described above, and then subjected to various durations of prior isothermal mechanical cycling (e.g. 0, 50, 100, 300, 600, 900, and 1200 cycles) that were below the fatigue life of the materials. The cycled samples were then subsequently subjected to stress-strain or creep testing.

Figure 6.4 illustrates the degradations occurring in the tensile stress-strain curve of SAC305 solder due to various durations of prior mechanical cycling. The curves in Figure 6.4 are fits of eq. (1) to the data from five experimental tension tests performed for each level of cycling induced damage. It is easily observed that both the modulus (initial slope) and strength (maximum stress) were greatly reduced due to the prior cycling. The extracted values of the initial elastic modulus, Ultimate Tensile Strength (UTS), and yield stress are tabulated in Table 6.3. For SAC305, the reductions in modulus, UTS, and yield stress were 62%, 39%, and 44%, respectively, for the 1200 applied cycles.

Figure 6.5 shows analogous degradations occurring in the tensile stress-strain curve of SAC_Q solder due to various durations of prior mechanical cycling. Again, it is observed that the mechanical properties were all greatly reduced due to the prior cycling. The extracted values of the initial elastic modulus, Ultimate Tensile Strength (UTS), and yield stress are tabulated in Table 6.4. For SAC_Q, the reductions in modulus, UTS, and yield stress were 28%, 37%, and 40%, respectively, for 600 applied cycles.

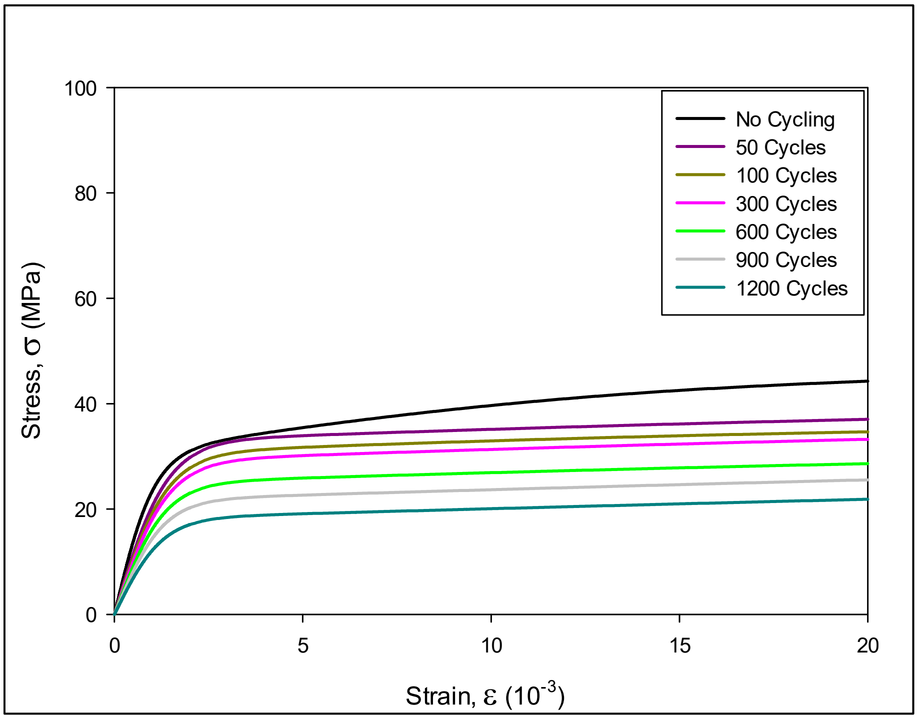

Figure 6.4 Stress-Strain Curve Evolution with Cycling (SAC305)

Table 6.3 Evolution of Material Properties with Cycling (SAC305)

No. of Cycles Prior to Testing	Initial Elastic Modulus (GPa)	Ultimate Tensile Strength (MPa)	Yield Stress (MPa)
0	37.72	48.19	33.09
50	30.35	40.23	32.95
100	23.89	38.22	31.77
300	21.89	37.15	29.23
600	19.06	32.12	25.18
900	18.88	31.03	22.04
1200	14.48	29.46	18.56

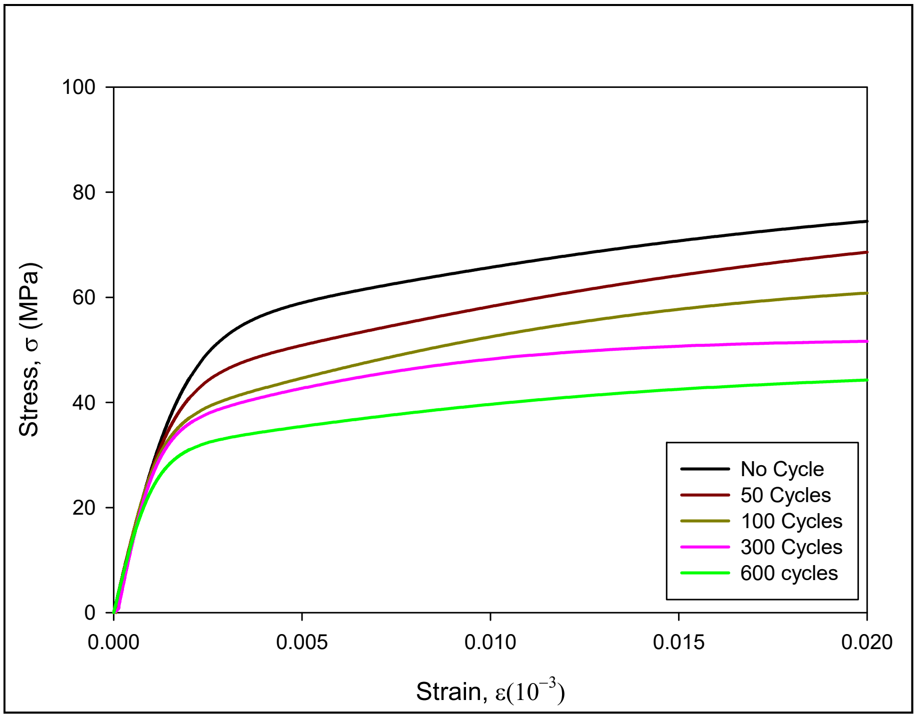

Figure 6.5 Stress-Strain Curve Evolution with Cycling (SAC_Q)

Table 6.4 Evolution of Material Properties with Cycling (SAC_Q)

No. of Cycles	Initial Elastic Modulus (GPa)	Ultimate Tensile Strength (MPa)	Yield Stress (MPa)
0	39.26	74.31	49.63
50	33.14	67.22	41.49
100	32.67	62.16	36.28
300	31.85	55.73	34.15
600	28.44	46.54	29.67

Figs. 6.6 and 6.7 illustrate the observed evolutions of the creep responses of SAC305 and SAC_Q, respectively, with prior mechanical cycling. Similar to aging effects, the creep behavior changed much more significantly than the tensile mechanical properties. In particular, the secondary creep strain rate (steady state slope of curves) is observed to change dramatically as damage accumulates in the specimens, especially for SAC305. The

creep strain rates were extracted from the curves in Figs. 6.6 and 6.7 by fitting eq. (2) to the raw experimental data. The calculated values are listed in Table 6.5.

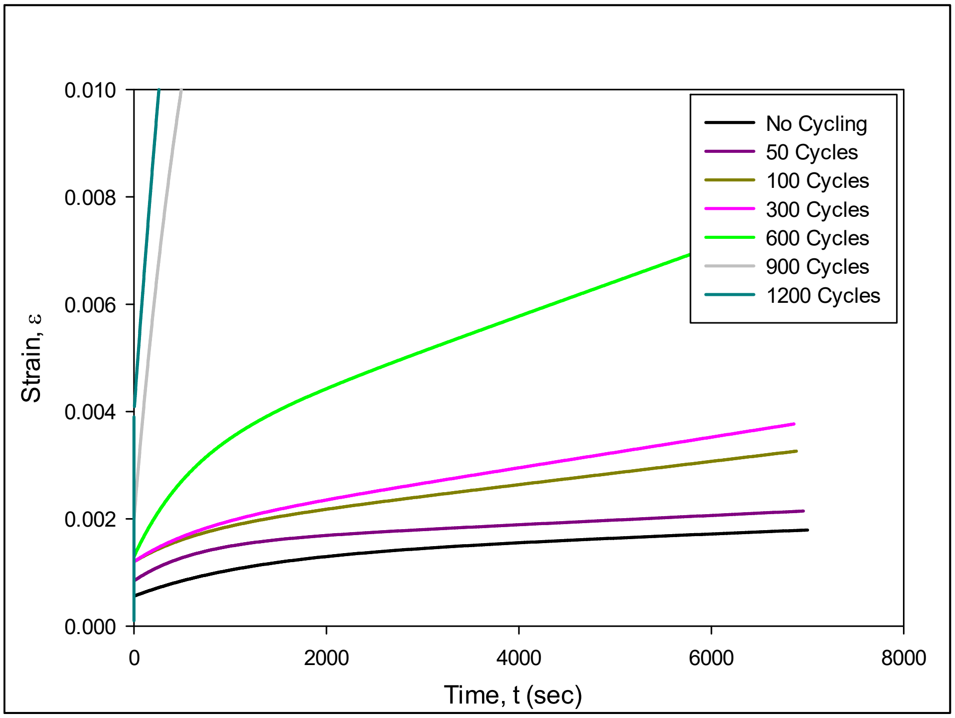

Figure 6.6 Evolution of the Creep Response with Cycling (SAC305)

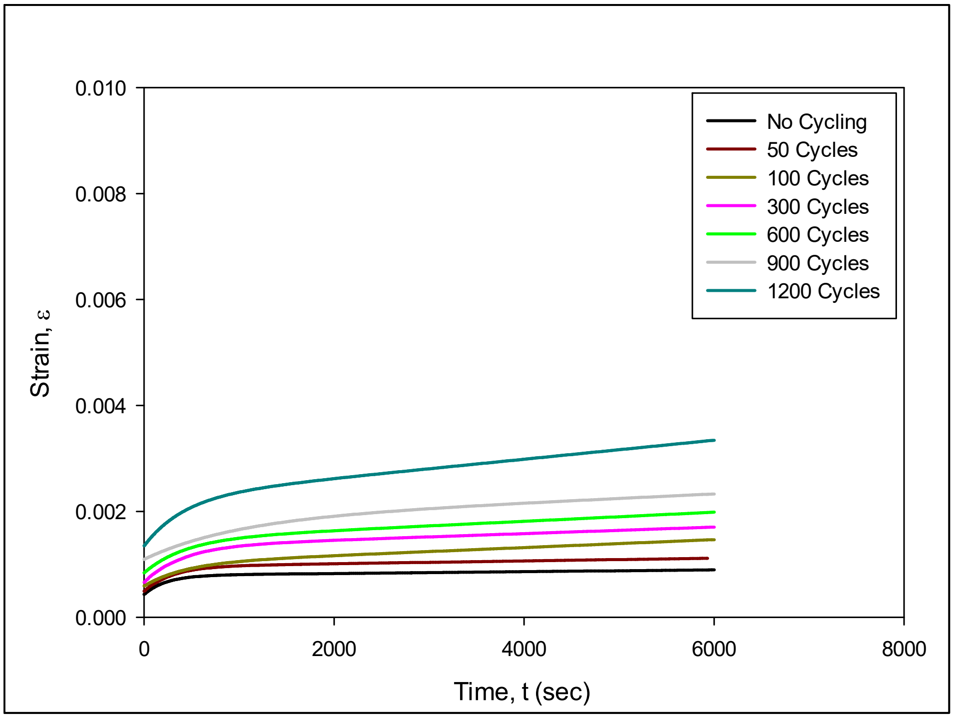

Figure 6.7 Evolution of the Creep Response with Cycling (SAC_Q)

Table 6.5 Evolution of the Creep Strain Rate with Prior Cycling

No. of Cycles Prior to Testing	Secondary Creep Strain Rate ($\times 10^{-8}$ sec^{-1})	
	SAC305	SAC_Q
0	7.14	1.73
50	8.61	2.62
100	21.6	11.26
300	28.5	12.96
600	64.5	16.90
900	227	19.13
1200	335	30.54

The results in Table 6.5 show that the creep rate of SAC305 increased 46.9X (4590%), while the creep rate of SAC_Q increased 17.6X (1660%). Mechanical cycling caused the initiation and growth of intergranular cracks at the sub-grain boundaries. This results in exacerbated grain boundary sliding and highly accelerated creep.

6.4 Summary and Discussion

In this chapter, the effects of isothermal mechanical cycling on damage accumulation in lead free SAC305 and SAC_Q (SAC+Bi) solder joints have been explored. In particular, we have examined both the degradations occurring in the solder constitutive behavior (stress-strain and creep) as cycling progresses during fatigue testing. Such knowledge is necessary to develop accurate fatigue criteria for lead free solder alloys. In addition to quantifying damage accumulation during cyclic testing, we have also measured the evolution of the cyclic stress-strain behavior (hysteresis loop area, plastic strain range, and peak stress) during single fatigue tests run to failure.

For the mechanical cycling experiments, cylindrical uniaxial SAC305 and SAC_Q lead free solder test specimens have been prepared using a vacuum suction reflow process within glass tubes. To study the evolution of the cyclic stress-strain behavior during a single fatigue test, the uniaxial specimens have been subjected to cyclic stress/strain loading at constant temperature until fatigue failure. The cyclic stress-strain curves after various durations of cycling have been extracted, and a four-parameter hyperbolic tangent empirical model has been used to fit the entire cyclic stress-strain curve at each chosen increment of cycling.

From the recorded cyclic stress-strain curves, the evolution of the solder hysteresis loops with number of cycles has been characterized. Also, the dependencies of the hysteresis loop area (plastic strain energy density), plastic strain range, and peak stress on the duration of cycling have been studied. The first two parameters are often considered to be driving forces for fatigue damage, and used in fatigue life prediction models, such as Morrow model and Coffin-Manson model. Near fatigue failure, the decreases in loop area

(56%, 54%) and peak stress (48%, 54%) were similar for the two materials. The plastic strain range remained essentially constant during the cycling for both materials.

To study the effects of cycling on damage accumulation and degradation of the constitutive behavior of SAC305 and SAC_Q, uniaxial samples have been prepared and subjected to various durations of prior isothermal mechanical cycling (e.g. 0, 50, 100, 300, 600, 900, 1200 cycles) that were below the fatigue life of the materials. Thus, the prior cycled samples contain different amounts of cycling induced material damage.

The cycled samples were then subsequently subjected to stress-strain or creep testing. Using the data from the various tests, we have been able to characterize and quantify the cycling induced damage through the observed degradations of several mechanical properties (elastic modulus, yield strength, ultimate strength, and creep strain rate) with the amount of prior cycling. The degradations in the creep strain rate were especially significant for both materials due to exacerbated grain boundary sliding from intergranular fatigue cracking.

CHAPTER 7

AGING INDUCED MICROSTRUCTURE EVOLUTION IN LEAD FREE SOLDERS DUE TO CYCLIC LOADING

7.1 Introduction

The changes in solder mechanical behavior that occur during fatigue testing as well as isothermal aging are a result of the evolution of the SAC solder microstructure. When exposed to an external temperature changing environment or a frequent power switching, these solder joints experience a thermal cyclic loading because of the differences in coefficients of thermal expansion of the various components of the package. This thermal cycling induces both a mechanical cycling loading and a temperature induced aging, the latter mainly occurring due to a high temperature dwell. Cycling of this nature subsequently causes thermomechanical fatigue damage to be accumulated within the sample. Evidence of this damage is observed by recrystallization of grains, and the onset and propagation of cracks, which ultimately leads to failure of the solder joints. Similar effects also occur in lead free solder uniaxial samples subjected to tension and compression cyclic loading, when they are exposed to isothermal repetitive mechanical cycling between two fixed strain extremes. The material damage that occurs during cyclic loading becomes immediately evident through the “load drop” and “widening” that occurs in the cyclic stress-strain curves as cycling progresses. Eventually, this damage leads to micro crack formation, crack growth, and failure.

Previous chapter included studies of cyclic induced damage accumulation in both lead free and doped solder alloys, changes in the constitutive properties due to mechanical cycling of SAC305 and SAC_Q solder alloys. In this study, we have investigated the microstructural evolution occurring in fixed regions of cycled SAC305 and SAC_Q samples due to the cyclic loading. Later, we have also examined the effects of prior aging on damage accumulation occurring in SAC305 and SAC_Q solder materials subjected to mechanical cycling (fatigue testing). Uniaxial samples have been prepared and polished so that the microstructural changes could be tracked after the initial aging, and then subsequently with mechanical cycling. In particular, we examined the microstructural changes that occurred in small fixed regions in the solder samples, rather than using several different regions. Regions of interest near the center of the sample were marked using small indents formed with a nanoindentation system. Samples were then subjected to aging at 125 °C for various durations to produce several different initial microstructures. Scanning electron microscopy (SEM) were used to investigate the aging induced microstructural changes in the regions of interest in the solder sample.

After aging, the samples were then subjected to mechanical cycling. After various durations of cycling (e.g. 0, 10, 25, 50, 75, 100, 200, 300 cycles) that were below the fatigue life of the materials, the regions of interest were again examined using SEM. Using the recorded images, the microstructural evolutions in the fixed regions were observed, and the effects of the initial aging on the results were determined.

7.2 Microstructure Evolution with Cycling

To observe microstructural evolution due to mechanical cycling, special rectangular cross-section uniaxial test specimens were prepared and polished. The vacuum suction approach discussed above was again utilized with glass tubes with rectangular cross-sections, and the final specimen dimensions were 30 x 3 x 0.5 mm. After visually inspecting a sample, it was temporarily attached to an epoxy preform/carrier using double stick tape, so that a 30 x 3 mm flat surface of the solder sample was exposed. The exposed surface was then polished using standard procedures until the microstructures were clearly visible under an optical microscope. Several fixed square regions with dimensions of approximately 90 x 90 μm were then selected in the polished region of each sample for subsequent SEM observations. To locate and track the selected fixed regions, they were demarcated using four nanoindentation marks placed at their corners using a Hysitron TI 950 nanoindentation system as shown in Figure 7.1.

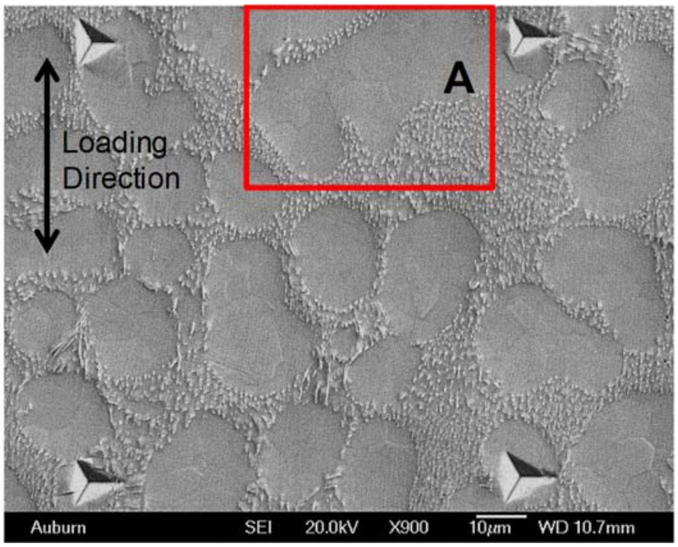

Figure 7.1 Microstructure in region of interest demarcated using nanoindentations

After polishing and applying the nanoindentation marks, the specimens were carefully removed from the temporary carriers. The microtester was used to mechanically cycle the prepared specimens at room temperature, and a total strain range of $\varepsilon = \pm 0.005$ was used per cycle for both SAC305 and SAC_Q materials. A gage length of 5 mm was again used for the tests, as well as a strain rate of $\dot{\varepsilon} = 0.002 \text{ sec}^{-1}$. After various durations of cycling (e.g. 0, 25, 50, 75, 100, 200, 300 cycles), the specimens were removed from the testing machine and SEM observations were made of the microstructures in the fixed regions of interest. The nanoindentation marks facilitated in relocating the fixed regions of interest after various durations of mechanical cycling. As seen in the figure, β-Sn dendrites are surrounded by eutectic regions of IMC particles. The brittle IMC particles were mostly Ag_3Sn and Cu_6Sn_5 and provided pinning points that helped mitigate and formed barriers against dislocation movements.

Our initial analysis on the changes in microstructure has been focused on the specimen surface, as damage induced by fatigue has been found to be primarily a surface phenomenon. Regions close to and near the surface are typically observed to be sites of nucleation for fatigue cracks resulting from the growth of slip line steps in the form of extrusions and intrusions, and the relative ease of inelastic deformation. The region A have been marked with a red box in Figure 7.1. This region was magnified and closely observed for changes in microstructure during the mechanical cycling. The corresponding micrographs depicting the cyclic induced damage in this region are shown in Figure 7.2. Microstructural observations were recorded with the SEM after the specimens were cycled for 0, 10, 25, 50, 75, 100, 200, and 300 loading cycles.

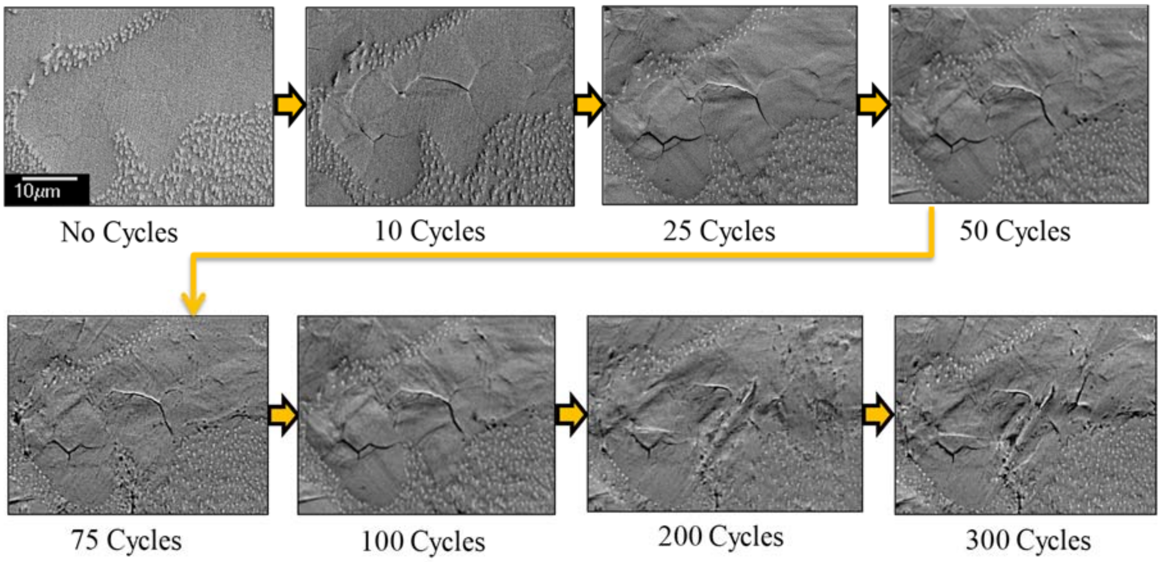

No Cycles 10 Cycles 25 Cycles 50 Cycles

75 Cycles 100 Cycles 200 Cycles 300 Cycles

Figure 7.2 Evolution of Microstructure with Mechanical Cycling (Region A, SAC305)

From the initial micrographs for both regions, we can see the formation of microcracks originating in the β-Sn phase especially along the subgrain boundaries. These cracks grew in length as the number of cycles increased, propagated along the maximum tensile stress plane and in the process weakening the β-Sn dendrites. The cracks began to then coalesce and subsequently created larger transgranular cracks. Another observation was that not all cracks resulting from this fatigue induced damage nucleated from slip bands. The observation of peaks and valleys formed in the dendrite structure provides evidence of the creation of extrusions and intrusions. The formation of microvoids was evident after the 100 cycle loading period. No such changes (in size or distribution) or development of microcracks were noticed in the intermetallic or eutectic region. One can thus infer that this region does not play a major part in the development of the microcracks.

Figure 7.3 shows typical non-cycled microstructures for the SAC_Q specimen. β-Sn dendrites were surrounded by eutectic regions containing Ag_3Sn and Cu_6Sn_5 IMC particles. However, the dendrites in the SAC_Q samples were somewhat larger than those in the SAC305 samples. In addition, the addition of Bi in SAC_Q led to a dispersion of Bi rich IMC particles, which appeared white in SEM micrographs using back scattered electrons. Bismuth has a high solid solubility in Sn, which leads to an improved strength of the Sn matrix by the solid solution strengthening (SSS) mechanism.

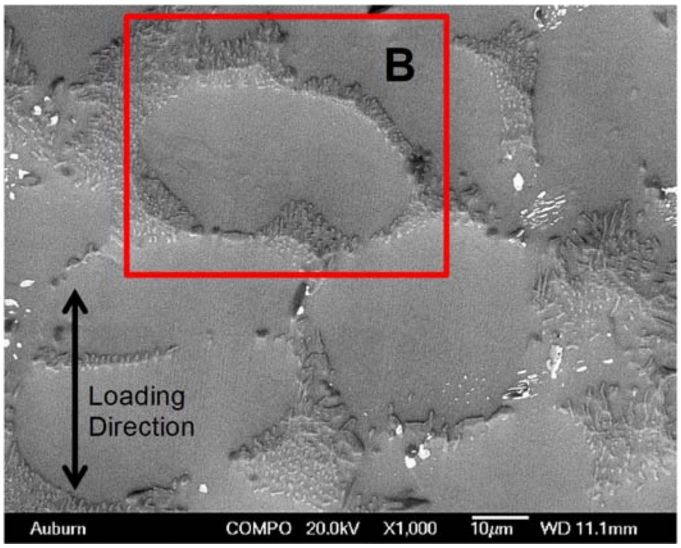

Figure 7.3 Typical Microstructure of SAC_Q Specimen

For the SAC_Q specimens, intergranular cracking was also observed, but to a lesser extent. There were also abundant slip lines visible within the dendrites of the SAC_Q specimens (see Figure 7.4). In particular, slip lines (intrusions and extrusions) that look like material wrinkles/ripples formed at the surface of the dendrites. As cycling progressed, these slip lines became more visible within the specimen and slip line steps were acting as one of the sources of crack nucleation. Example micrographs illustrating the evolution of damage during cyclic loading are shown in Figure 7.4 for SAC_Q specimen. The region B that was monitored (red box) shown in Figure 7.3. For this fixed region, the microstructures are shown for 0, 25, 50, 75, 100, 200, and 300 loading cycles. The initial micro cracks formed within the first 50 loading cycles. These cracks continued to grow as the cycling continued, resulting in a weakening of the dendrite structure, and eventually to the formation of large transgranular cracks. Similar like SAC305, no major changes were observed in the eutectic region or the IMCs, suggesting that they do not play significant roles in the propagation of the microcracks. Significant numbers of slip lines were visible in the SAC_Q microstructure after 25 cycles, while they became prominently visible after 100 cycles for SAC305.

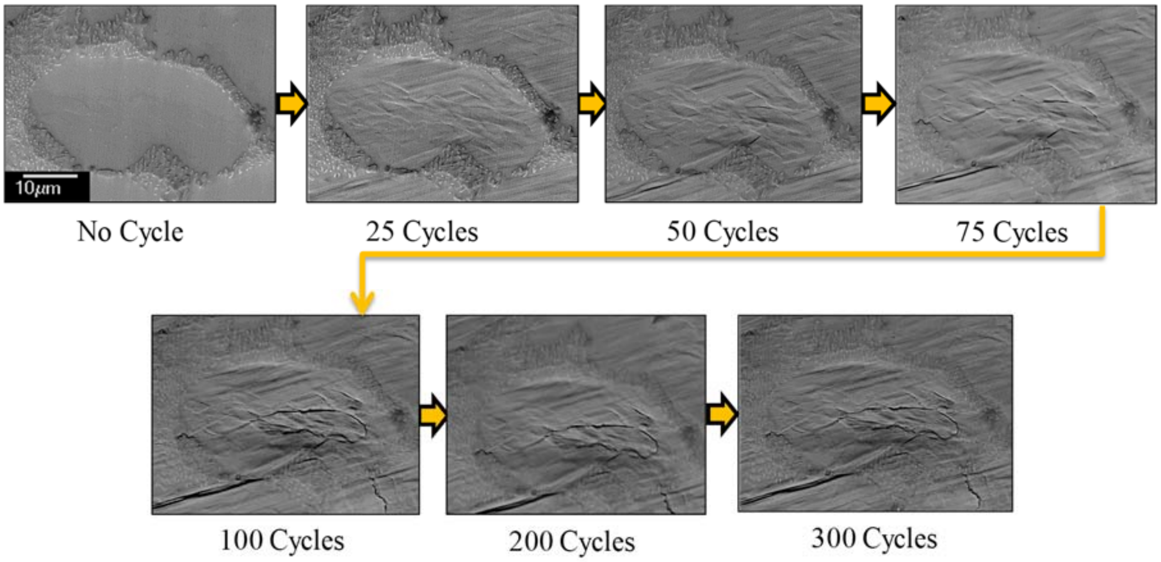

Figure 7.4 Evolution of Microstructure with Mechanical Cycling (Region B, SAC_Q)

7.3 Microstructure Evolution in Aged Samples with Cycling

The experiments discussed in the last section were repeated with samples subjected to prior aging before they were cycled. As discussed above, significant changes in the cyclic stress-strain properties occur within 10 days of aging at 125 °C. Thus, this was selected as the aging condition. After completing the sample preparation and polishing, the test specimens were viewed under the SEM to record the microstructure of the non-cycled and non-aged samples. Examples are illustrated in Figure 7.5, along with selected region of interest C that was tracked using nanoindentation marks. The samples were then aged under no mechanical loading, and the microstructures were recorded again in the SEM. Finally, the samples were mechanically cycled with the same total strain range of $\varepsilon = \pm 0.005$, and additional microstructural observations were made after the specimens were cycled for 0, 10, 25, 50, 75, 100, 200, and 300 loading cycles.

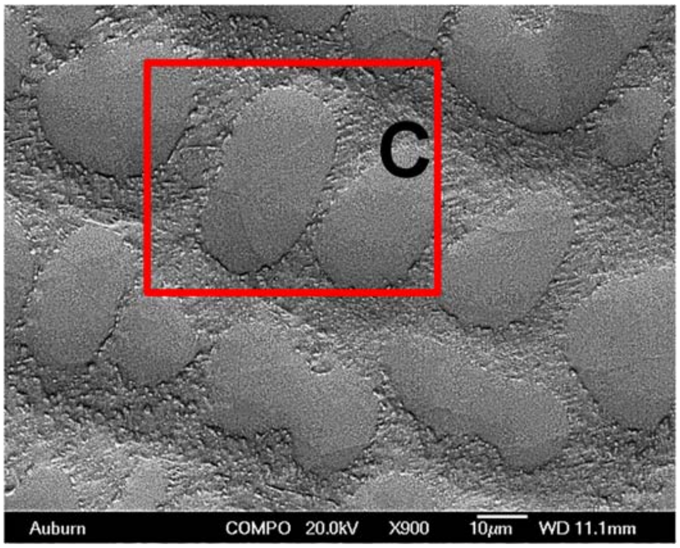

Figure 7.5 Region of Interest for Cycling Tests with Aged SAC305 Specimen

Figure 7.6 illustrated the microstructural and damage evolutions for the fixed region C. During the aging before cycling, the most obvious changes were the coarsening of IMC particles (e.g. differences between Figure 7.6 (a) and Figure 7.6 (b). In particular, the number of IMC particles decreased, while the average size of the particles and average particle separation distance increased significantly with aging. A common observation is that larger particles are produced at the expense of smaller particles. This IMC coarsening phenomenon is also known as Ostwald Ripening.

According to the Gibbs-Thompson effect, an increase in particle size is accompanied by a decrease of the solute concentration in the matrix surrounding the particle. This leads to a concentration gradient, and solute atoms near smaller particles will diffuse towards the larger particles where the reductions in solute concentration has occurred. In addition, atoms from the smaller particles will go back into solution. The overall effects are shrinkage of smaller particles, and growth of larger particles. Since Ostwald Ripening is a diffusion-based process, use of higher aging temperatures will increase the rate of coarsening significantly.

The coarsening and coalescing of IMC particles during aging play a significant role in the degradations of solder mechanical properties. Usually IMC particles facilitate to pin and block the dislocation movement. However, due to aging, we observed that there are a smaller number of larger IMC particles and increased spacing between the IMC particles. Orowan proposed a mechanism that when a dislocation crosses incoherent precipitate particles (like the IMC particles in present case), it will bow and leave a loop of stress field around the particle [61]. The yield stress and strength of a material depends on the shear stress (also known as the Orowan stress) that is required for a dislocation to pass through the particles. This shear stress will decrease as the inter-particle spacing increases during aging. Therefore, the yield stress and strength of a material will decrease with the coarsening and coalescing of IMC particles.

In case of aged samples, it was observed that the cycling induced damage consisted primarily of small intergranular cracks forming within dendrites just after the 10th cycles. These cracks continued to grow as the cycling continued, resulting in a weakening of the dendrite structure. In addition, the IMC region became weaker due to the coarsening and coalescing of IMCs during the prior aging. Hence, there are some tiny cracks visible in the IMC region even after 25 cycles in case of region C (Figure 7.6 (d)). These cracks eventually helped the transgranular cracks develop more quickly. In comparison to the non-aged SAC305 samples, the IMC region was less effective pinning and blocking the intergranular cracks. Therefore, it has been found that aged SAC305 samples exhibited more damage compared to the non-aged samples after the same cycling duration. Isothermal aging leads to the degradation of the microstructure of SAC305, which increase the rate of damage accumulation and eventually decreases the fatigue life.

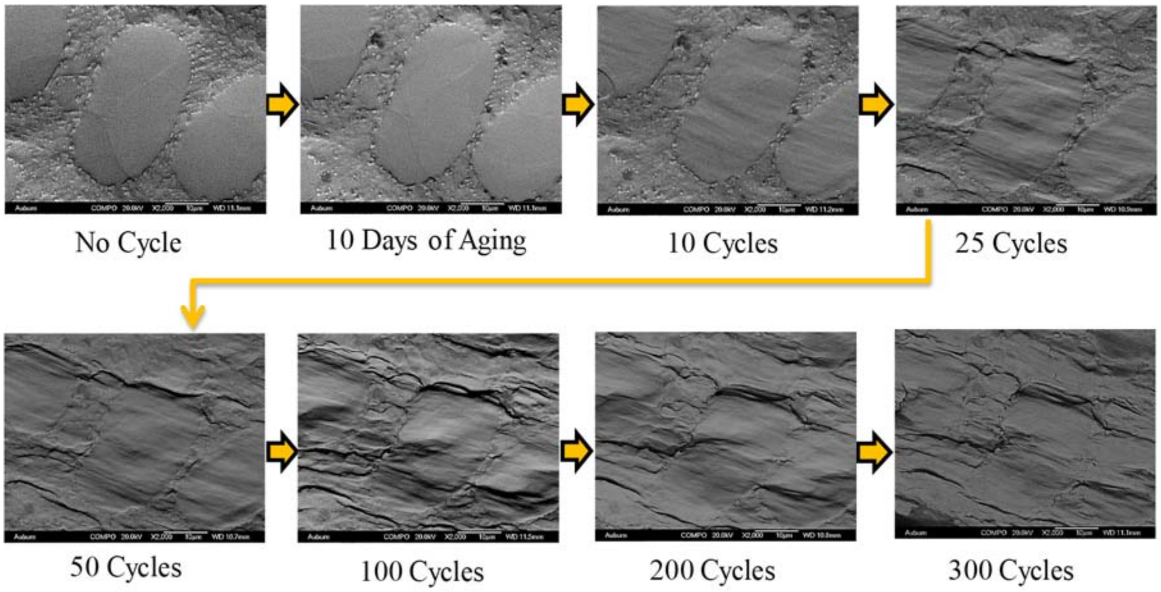
No Cycle
10 Days of Aging
10 Cycles
25 Cycles
50 Cycles
100 Cycles
200 Cycles
300 Cycles

Figure 7.6 Aging Induced Evolution of Microstructure with Mechanical Cycling (Region C, SAC305)

The aging effects on the Bi-doped SAC solder microstructure were also studied using SEM. Figure 7.7 shows typical microstructures of SAC_Q before aging.

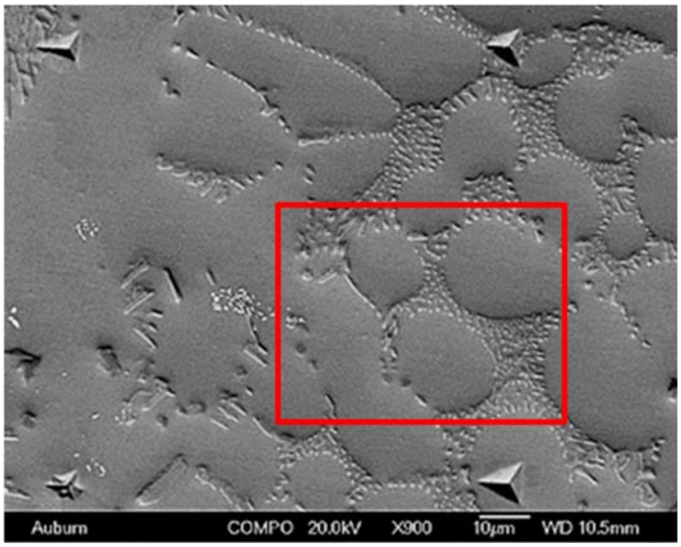

Figure 7.7 Region of Interest for Cycling Tests with Aged SAC_Q Specimen

From Figure 7.7, the BSE images exhibit traces of white particles in the microstructure. This is also evident at higher magnification (Figure 7.8 (a)). EDS analysis of these white particles has confirmed that they are Bi-rich phases/regions with more that 80% Bi. After aging, these particles are not evident (Figure 7.8 (b)), suggesting that the Bi has completely dissolved into the β-Sn matrix providing solid solution strengthening. From the Sn-Bi phase diagram, we found that Bi has about 1.8% solid solubility in Sn at room temperature. Hence Bi contributes to some enhancement in strength of the doped alloy before aging by the solid solution strengthening mechanism. The solid solution solubility of Bi increases from 1.8% at T = 25 °C, to about 18% at 125 °C. Thus, the Bi present in the as solidified microstructure of SAC_Q as a separate Bi- phase will have the tendency to go into the solution with the β-Sn matrix during aging. This will lead to additional solid solution strengthening of the SAC-Bi alloy.

During aging, intermetallic coarsening effects in SAC_Q are less significant compared to SAC305 because of the addition of bismuth. Under similar aging conditions, the microstructure of SAC305 in Figure 7.6(b) coarsened significantly relative to the initial reflow microstructure, while that for SAC_Q showed only slight changes with aging as shown in Figure 7.8 (b). For both alloys, the major changes in particle diameter occurred within the first 10 Days of aging. After that point, the particle size was seen to increase at a slow but steady state rate. Because they were formed using the same reflow profile, the initial IMC particles sizes were almost the same for the SAC305 and SAC_Q joints. After aging, the average SAC305 particle diameter was almost twice that of SAC_Q.

Hence, we found a correlations between the reductions in ultimate tensile strength and the increase in IMC particle size. It is clear that the evolution of the mechanical strength of the solder alloys is closely linked to variation in IMC particle diameter, and that the effects of aging are much greater for SAC305 than SAC_Q. The bismuth present as a dopant in SAC_Q made it relatively insensitive to aging induced degradations by a combination of the solid solution strengthening mechanism and a slower coarsening of the Ag3Sn IMC particles. The aging induced presence of bismuth in solution within the β-Sn matrix provided an increased resistance to the Ostwald ripening diffusion process that coarsens the IMC particles.

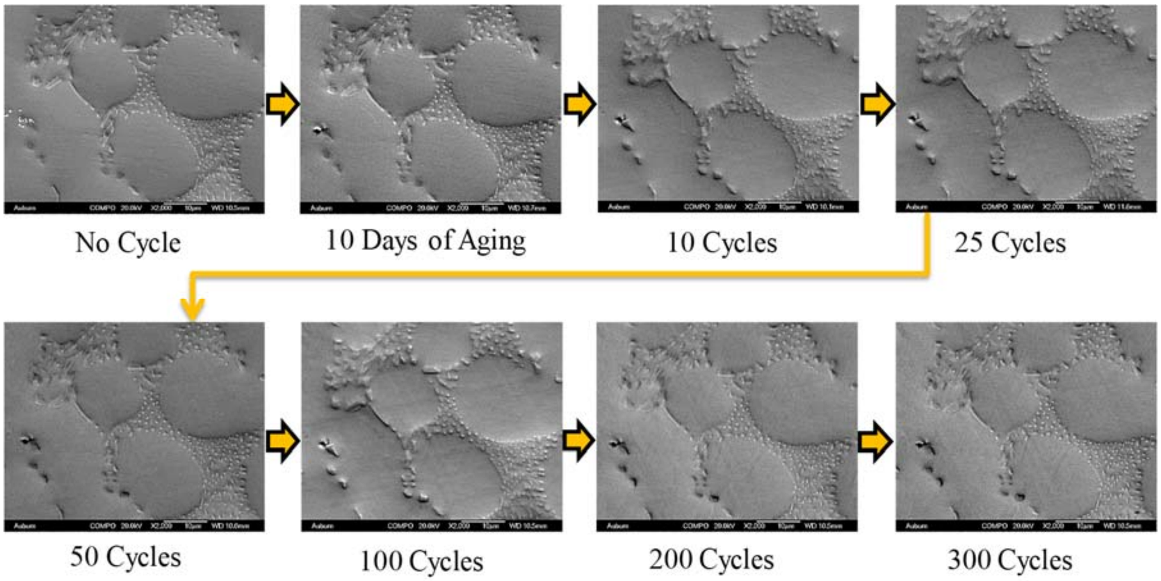

Figure 7.8 Aging Induced Evolution of Microstructure with Mechanical Cycling (Region D, SAC_Q)

7.4 Discussion of IMC Evolution during Aging

The reduction of strength of SAC305 after aging can be attributed to 2 major facts. First, aging causes coarsening of the Ag_3Sn and Cu_6Sn_5 intermetallic compounds and hence reduces their ability to block dislocation movements. Second, the β-Sn phase also coarsens/grows with aging, and hence reduces the strength of the alloy. For the SAC_Q alloy, Bi doesn't form any IMC with Sn. Therefore, the IMC's that should present in microstructure of SAC_Q are same as SAC305 (i.e. Ag_3Sn and Cu_6Sn_5). From the Sn-Bi phase diagram (see Figure 7.9), it is observed that Bi has a good (~1.8%) solid solubility in Sn at room temperature. Hence Bi contributes to some enhancement in strength of the doped alloy before aging by the solid solution strengthening mechanism. As seen in Figure 7.9, the solid solution solubility of Bi increases from 1.8% at T = 25 °C, to about 18% at 125 °C. Thus, the Bi present in the as solidified microstructure of SAC_Q as a separate Bi- phase will have the tendency to go into the solution with the β-Sn matrix during aging. This will lead to additional solid solution strengthening of the SAC-Bi alloy. The increases in strength from solid solution strengthening nullify any reductions in strength caused by IMC and β-Sn phase coarsening. As a result, no significant difference was evident in stress-strain behavior, before and after aging.

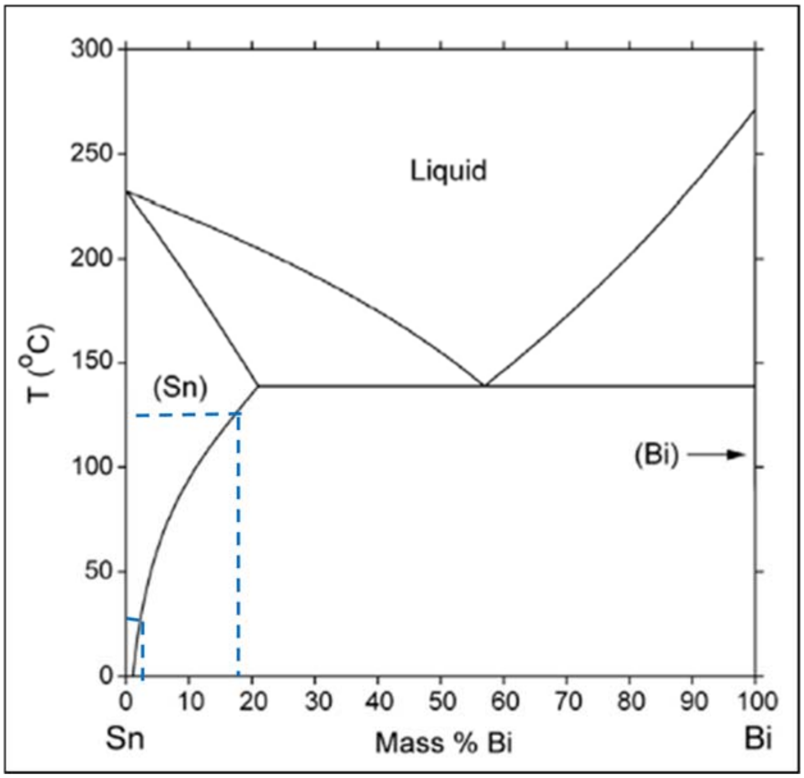

Figure 7.9 Sn-Bi Phase Diagram
(http://www.metallurgy.nist.gov/)

To support the proposed mechanism for mitigation of aging effects in SAC-Bi alloys, a study on the microstructure of SAC_Q was performed as shown in the backscattered electron (BSE) imaging in Figure 7.10. From this micrograph we noticed that the BSE image exhibits traces of white particles in the microstructure. EDS analysis of these white particles has confirmed that they are Bi rich phases/regions with more that 80% Bi. After aging, these particles are not evident, suggesting that the Bi has complete dissolved into the β-Sn matrix providing solid solution strengthening. Thus, the microstructure results strongly support the hypothesis for aging mitigation.

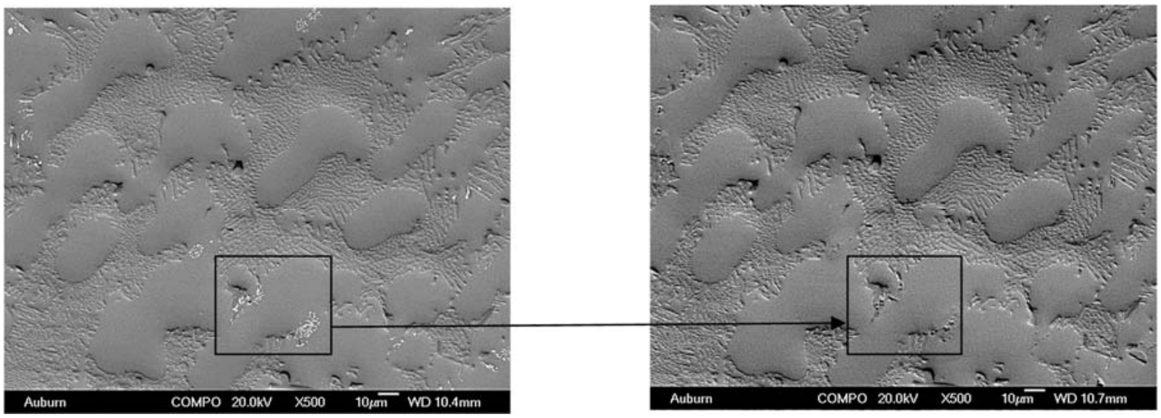

Figure 7.10 Backscattered electron imaging of SAC_Q a) before aging, b) after aging

Typically, IMC particles tend to become more round (spherical) with aging. Atoms on the surface of a particle have higher energy than the atoms inside a particle due to unsatisfied bonds in the surface atoms. A cylindrical or elongated particle has a higher fraction of surface atoms (or higher surface to volume ratio) compared to a spherical (round) particle with the same volume. As a result, the free energy per atom of an elongated particle or several small particle is higher than a big round particle with equal volume. This free energy difference is the driving force that causes the transition of IMC particles from smaller to a bigger size. This IMC coarsening phenomenon is also known as Ostwald Ripening. According to the Gibbs-Thompson effect [139-141], an increase in particle size is accompanied by a decrease of the solute concentration in the matrix surrounding the particle. This leads to a concentration gradient, and solute atoms near smaller particles will diffuse towards the larger particles where the reductions in solute concentration has occurred. In addition, atoms from the smaller particles will go back into solution. The overall effects are shrinkage of smaller particles, and growth of larger particles. A schematic of the variation of solute concentration around a small and a large particles is shown in Figure 7.11. Since Ostwald Ripening is a diffusion-based process, use of higher aging temperatures will increase the rate of coarsening significantly.

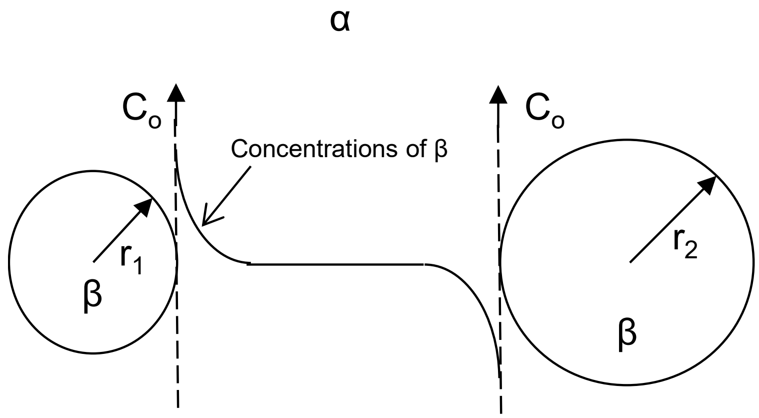

Figure 7.11 Schematic of Solute Concentration in Front of A Small and a Large Particle [141].

The coarsening and coalescing of IMC particles during aging is known to play a critical role in the degradations of solder mechanical properties. IMC particles will pin and block the movement of dislocations. However, aging leads to both a smaller number of larger IMC particles and increased spacing between the IMC particles. The interparticle spacing λ can be calculated from the following equation:

$$\lambda = \frac{4(1-f)r}{3f} \tag{7.1}$$

Where f is the volume fraction of the particles and r is the particle radius. Hence for a fixed volume fraction of the IMC particles, spacing between the particles increases with increasing particle diameter. Orowan proposed a mechanism that when a dislocation crosses incoherent precipitate particles (like the IMC particles in present case), it will bow and leave a loop of stress field around the particle [140-142]. A schematic of the interaction between a dislocation and IMC particles is shown in Figure 7.12.

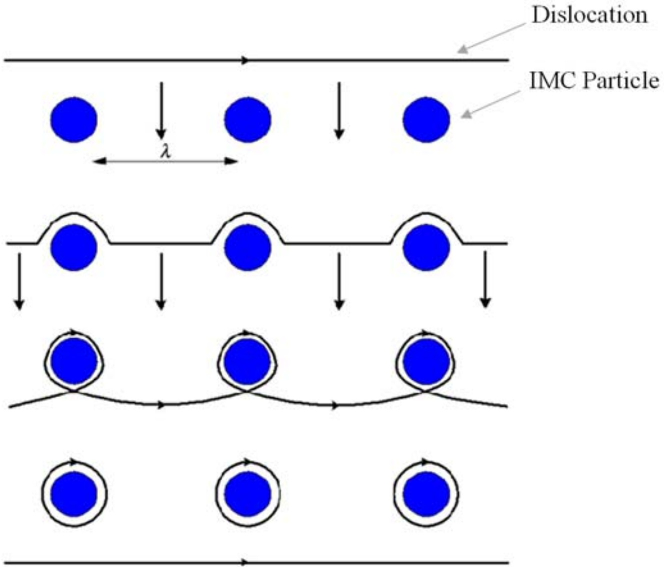

Figure 7.12 Schematic Representation of a Dislocation Passing IMCs (Orowan Looping) [142]

The yield stress and strength of a material depends on the shear stress (also known as the Orowan stress) that is required for a dislocation to pass through the particles. This shear stress will decrease as the inter-particle spacing increases during aging as shown in equation 7.2 [113, 114, 116]

$$\tau_o = \frac{Gb}{\lambda} \tag{7.2}$$

Where τ_o is the shear stress required for a dislocation to pass through the particles, G is the shear modulus, and b is the magnitude of the burgers vector. Therefore, aging leads to the coarsening of the IMC particles which causes to increase the interparticle spacing. Thus, the yield stress and strength of a material decrease after aging due to the increased interparticle spacing.

7.5 Summary

In this study, we have examined the effects of prior aging on damage accumulation occurring in SAC305 and SAC_Q solder materials subjected to mechanical cycling (fatigue testing). Uniaxial samples have been prepared and polished so that the microstructural changes could be tracked after the initial aging, and then subsequently with mechanical cycling. In particular, we examined the microstructural changes that occurred in small fixed regions in the solder samples, rather than using several different regions. Regions of interest near the center of the sample were marked using small indents formed with a nanoindentation system. Samples were then subjected to aging at 125 °C for various durations to produce several different initial microstructures. Scanning electron microscopy (SEM) were used to investigate the aging induced microstructural changes in the regions of interest in the solder sample. After aging, the samples were then subjected to mechanical cycling. After various durations of cycling (e.g. 0, 10, 25, 50, 75, 100, 200, 300 cycles) that were below the fatigue life of the materials, the regions of interest were again examined using SEM. Using the recorded images, the microstructural evolutions in the fixed regions were observed, and the effects of the initial aging on the results were determined. It was found that the number of IMC particles decreased while the average diameter of the particles increases significantly due to the initial aging.

After the cyclic loading was performed on the sample, for both SAC305 and SAC_Q solder alloys, it was observed that the cycling induced damage consisted primarily of small intergranular cracks forming along the sub-grain boundaries within the β-Sn dendrites. These cracks continued to grow in size as the cycling continued, resulting in a weakening of the dendrite structure, and eventually resulting in the formation of large transgranular cracks. The distribution and size of the intermetallic particles in the inter-dendritic regions were observed to remain essentially unchanged with the application of the mechanical cyclic load.

Relative to the non-aged samples, there were significant differences observed in the rate and intensity of the micro crack growth occurring in the heavily aged samples that began with much coarser microstructures. In particular, there were tiny cracks visible in the eutectic regions even after a small number of loading cycles (e.g. 25-50 cycles). These cracks eventually helped the transgranular cracks develop more quickly. In comparison to the non-aged SAC305 samples, the IMC region was less effective pinning and blocking the intergranular cracks. Therefore, it has been found that aged SAC305 samples exhibited more damage compared to the non-aged samples after the same cycling duration. In case of SAC_Q, we also observed that no significant changes have been noticed during the aging period. The observed increase of resistance against aging is due to the increase in strength from solid solution strengthening exceeding any reduction in strength caused by IMC and β-Sn phase coarsening. In summary, the doped SAC_Q alloy appears to be a promising solder material for use in thermal and/or mechanical loading not only because of improved cyclic properties but also for being strongly resistant to aging-induced evolution.

CHAPTER 8

EVOLUTION OF THE MECHANCIAL PROPERTIES OF INDIVUDUAL LEAD FREE SOLDER JOINT SUBJECTED TO CYCLIC LOADING

8.1 Introduction

Previous studies conducted on the effect of mechanical cycling on the material behavior of lead free solders have been performed on bulk samples subjected to tension and compression. Our goal in this study was to determine the evolution of the mechanical properties of doped lead free solder joints when subjected to mechanical shear cycling. Experiments conducted on actual solder joints would help us gain a better understanding on the real life effects of shear cycling. In this study, we have characterized the mechanical cyclic induced evolution of mechanical properties of individual solder joints. The testing of individual joints is important because there are significant variations of properties between actual joints and conventional bulk samples (e.g. dog-bone, rectangular, or lap shear samples). The test assemblies in this study were (3X3) BGA packages composed of total nine 0.75 mm diameter lead free solder balls which were formulated by reflowing solder spheres soldered onto 0.55 mm diameter Cu pads on FR4 coupons. The solder balls were cycled using an Instron Micromechanical tester along with a newly designed fixture which facilitates the tester to cycle a solder ball individually. The solder balls tested were of different alloys thus also giving an idea of the effect of the addition of various dopants on the mechanical cyclic properties. The balls were cycled for various durations including to failure. Nanoindentation tests were performed on the specimens to study the evolution in mechanical properties (e.g. elastic modulus, hardness and creep strain rate) of the solder balls as a function of duration of cycling. The prime objective of this study was to better understand the damage accumulation and evolution of a specific solder joint due to mechanical cyclic fatigue loading.

In this chapter, effects of shear mechanical cycling on SAC305 and SAC_Q solder ball joints was investigated. This would help us to understand the effects of fatigue cycling on solder joints in electronic packages and give us an idea of the role played by the effect of added bismuth on the mechanical cycling properties. The evolution of elastic modulus, hardness and creep resistance with various durations of shear mechanical cycling was evaluated with the help of a nanoindentation machine. The change in properties were then compared between the two lead free alloys.

8.2 Experimental Procedure

For this study, SAC305 (96.5Sn-3.0Ag-0.5Cu) and SAC_Q (92.7Sn-3.4Ag-0.5Cu-3.3Bi) lead free solder joints were tested. The joints had a diameter of about 30mils (762 μm). Figure 8.1 shows an example of the test joints used for the experiments. The samples consisted of a 3 x 3 Ball Grid Array (BGA) of the lead free alloys to be tested. The substrates used in the specimens were FR-4 PCBs. Samples which had an Immersion Silver (ImAg) surface finish on the copper pads were chosen as they produced the best shear strength when compared with other surface finishes [143]. Flux was deposited on the pads using a stencil. A reflow profile with a maximum temperature of 245 °C was obtained with the help of a Vitonics-Soltec convection oven. The profile also ensured that the assembly was kept above the liquidus temperature for about 45-60 seconds. The samples were then cleaned, dried and stored in a freezer at -40 °C to hinder any aging effects.

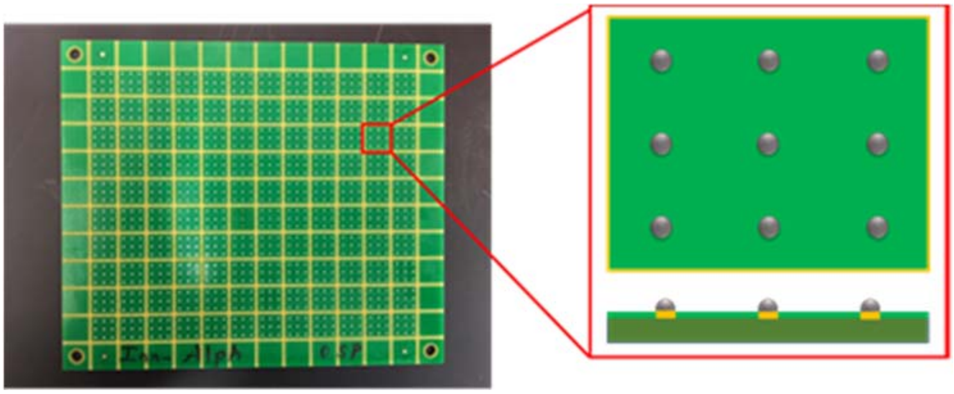

Figure 8.1 3x3 BGA Specimen Sample

Samples were covered with a tape and then confined in epoxy resin. The tape was used to prevent epoxy from entering the space between the individual joints which allows the cycling of each joint separately. The tape from these samples were removed by coarse grinding using a 320 grit SiC paper. Grinding papers up to 1200 grit were then used to reduce the scratches on the samples. The samples were then finally polished a 0.02 μm colloidal silica suspension to flatten the top surface of the solder joints and making the joints suitable for nanoindentation tests. A polished sample encapsulated in epoxy is shown in Figure 2. All the polished joints were viewed under a Polarized Light Microscope to verify that all experiments were conducted on single grain joints.

The Micromechanical Tester shown in Figure 3.20 was used to cycle the individual solder joints. The cyclic mechanical shear loading was conducted with a peak load of 600 gf (equivalent to a stress of about 24MPa). The joints were individually cycled in the shear direction for various durations of 50, 100, 150, 200 and 300 cycles. After every selected cyclic condition, the sample was removed and the degradation in Elastic Modulus, Hardness and Creep Strain Rate of each joint was characterized using the nanoindentation machine.

The nanoindentation machine utilized a probe with a Berkovich geometric tip to record the changes in load against indentation displacement. The recorded data was measured in the direction normal to the polished face. At least 5 indents were made on every solder joint for each set of conditions. Through trial and error, it was observed that a peak holding load of 30 mN was ideal for the nanoindentation tests. Using this high load not only prevented creep effects but also ensured that the indents made were deep enough to prevent surface effects while also ensuring these large indents covered all the solder phases present. A schematic depicting all the experimental techniques described above and used for this study has been presented in Figure 8.2.

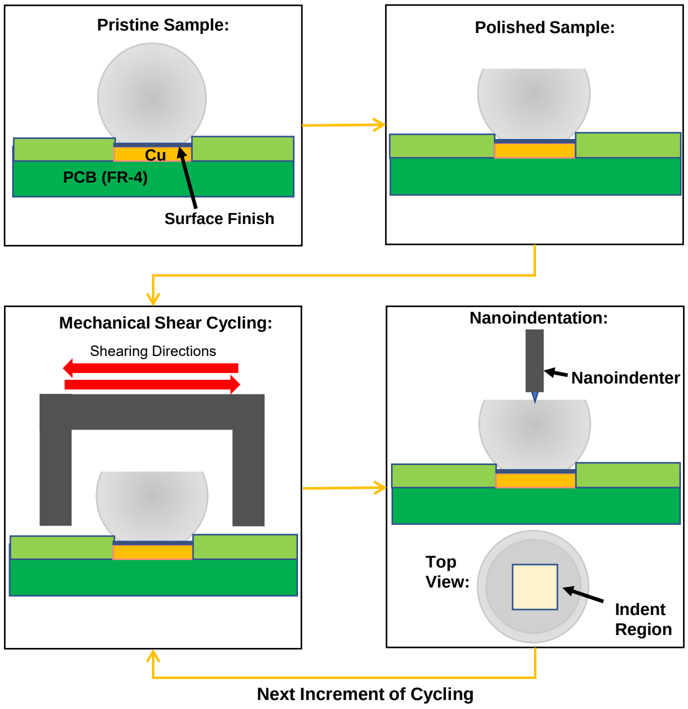

Figure 8.2 Schematic showing the experimental procedure

A trapezoidal loading profile with a peak load of 30 mN held for 30 seconds was used to determine the study the changes in elastic modulus and hardness with mechanical cycling. The hardness was evaluated by dividing the peak load applied by the contact area of the indenter. Oliver and Pharr proposed a method to obtain the reduced modulus from the slope of the unloading curve of the nanoindentation experiment [133]. A loading profile with a loading rate of 30 mN/s followed by a steady load of 30 mN (reference segment) was used for the creep nanoindentation tests. The 30 mN load was held for 900 seconds at the holding stage of the profile. The probe was then unloaded at a rate of -6 mN/s.

8.3 Evolution of Elastic Modulus and Hardness

Once the SAC305 BGA assembly was polished, the trapezoidal loading profile was utilized to obtain the elastic modulus and hardness of the SAC305 joints at the no-cycle condition. The indents were done in a column to keep track of the indents. Once the indentation tests were performed, the samples were mechanically cycled in shear up to 50 cycles using the Instron Micromechanical tester with a constant peak load of 600 gf. Each joint had to be individually cycled. Once the 50 cycles were completed, the sample was then indented to check for variations in the elastic modulus and hardness due to the cycling. This process was then repeated for 100, 150, 200 and 300 cycles. The results of two different solder balls will be presented here.

It was seen that with cycling of the SAC305 solder balls, there was a continuous drop in both elastic modulus and hardness. Table 8.1 represents the changes in elastic modulus of the two balls with mechanical cycling. Ball 1 exhibited a drop from 35.45 GPa to 25.74 GPa while Ball 2 exhibited a drop from 30.32 GPa to 20.45 GPa in elastic modulus after 300 cycles. This corresponds to a drop of 27.39% and 32.55% respectively for balls 1 and 2. Figs. 8.3 a) and b) illustrate this evolution in elastic modulus with shear mechanical cycling.

Table 8.1 Cycling Induced Changes of Elastic Modulus of SAC305

Cycling Duration (Cycles)	Elastic Modulus (GPa)	
	Ball 1	Ball 2
0	35.45	30.32
50	31.39	28.96
100	30.02	27.12
150	29.89	26.83
200	29.03	25.42
300	25.74	20.45

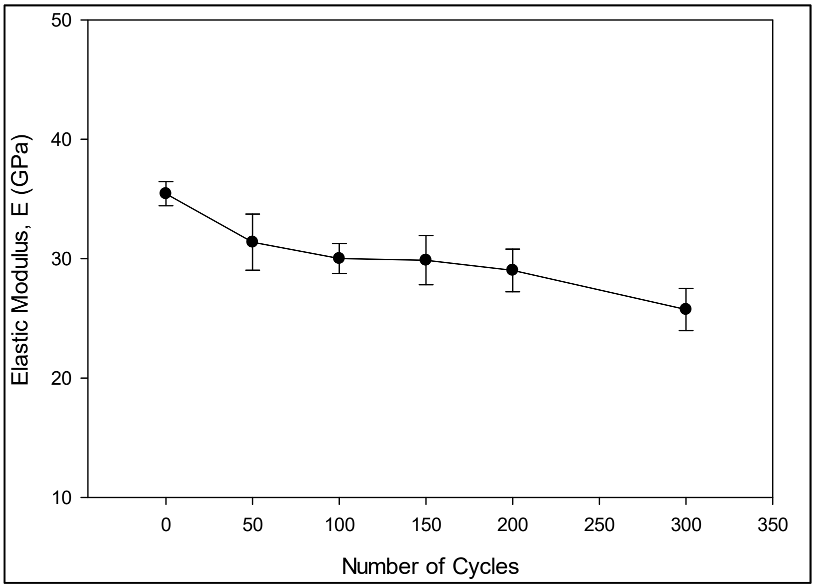

a) Joint 1

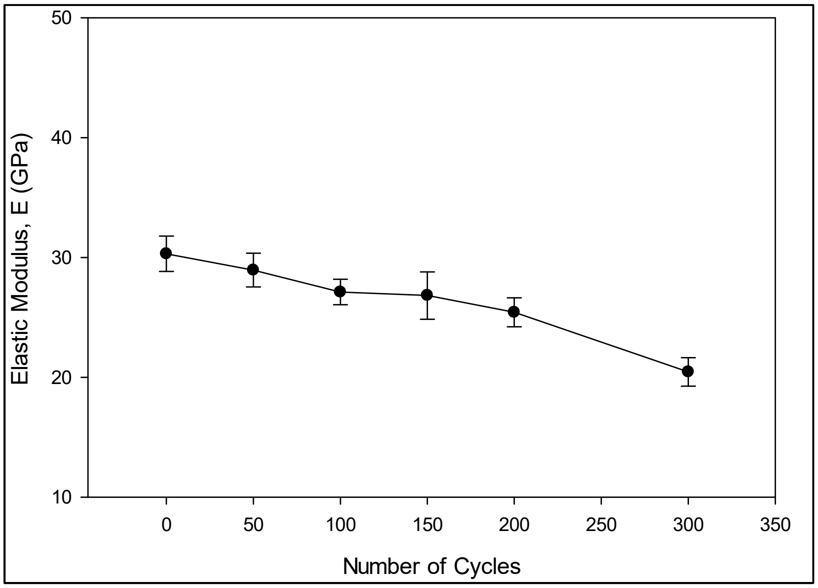

a) Joint 2

Figure 8.3 Variation of Elastic Modulus of SAC305 Joints with Shear Cycling

The evolution in hardness of the SAC305 joints with mechanical cycling has been summarized in Table 8.2. A 16.29% drop in hardness was observed for Joint 1 while a 12.04% drop in hardness was observed for Joint 2 after 300 cycles. These evolutions in hardness with mechanical cycling have been presented in Figs. 8.4 for SAC305.

Table 8.2 Cycling Induced Changes of Hardness of SAC305

Cycling Duration (Cycles)	Hardness (MPa)	
	Ball 1	Ball 2
0	270.91	285.32
50	249.87	279.19
100	245.94	272.05
150	243.34	259.53
200	234.15	257.71
300	226.79	250.98

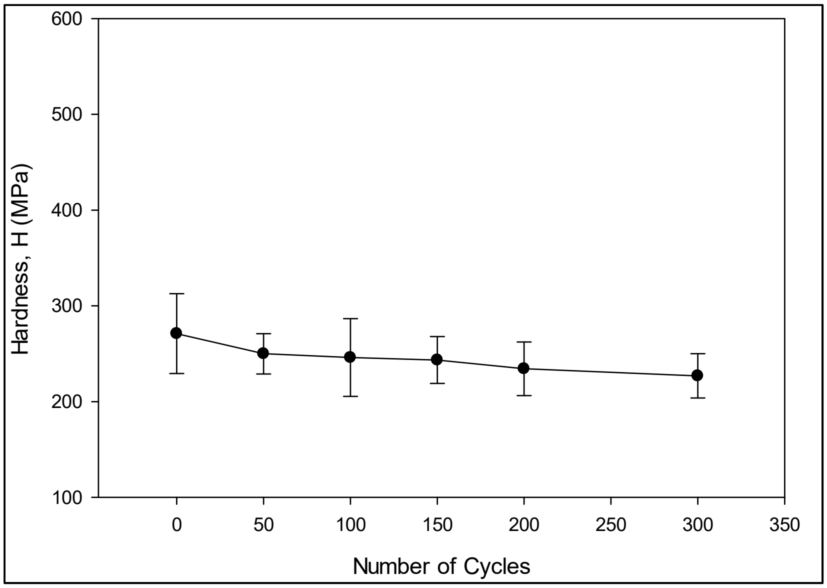

a) Joint 1

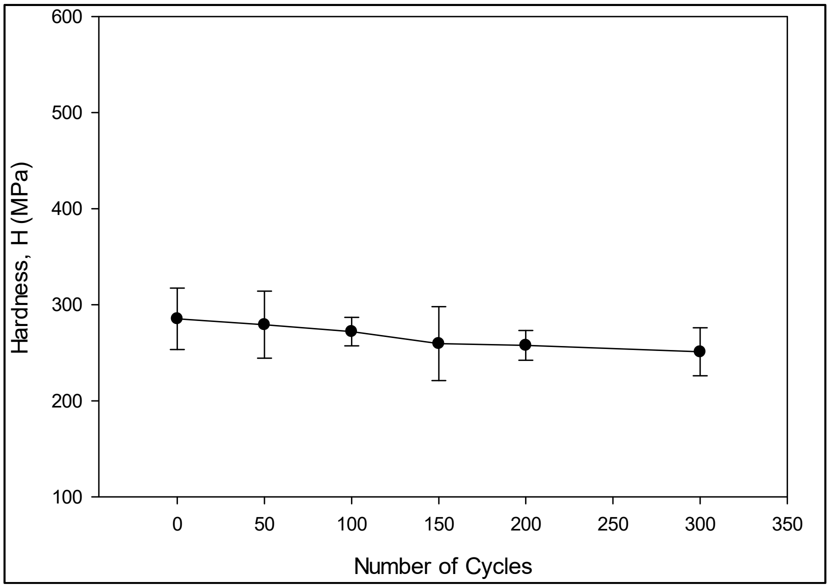

b) Joint 2

Figure 8.4 Variation of Hardness of SAC305 Joints with Shear Cycling

8.4 Evolution of Creep Properties

A different set of solder joints were used to investigate the creep resistance change due to shear mechanical cycling for SAC305. A constant 30 mN load with a dwell time of 900 seconds was used to conduct the nanoindentation creep tests. After initial testing (0 cycles), the samples were then cycled for various durations (e.g. 50, 100, 150, 200 and 300 cycles) with a maximum peak force of 600 gf. After each cycling duration, nanoindentation creep testing was performed. Similar to the previous section, only the results of two different joints for both alloys will be presented.

Figure 8.6 illustrates the creep displacement vs. time curves for each duration of prior shear cycling of SAC305. The averaged creep data for both cases were fit with a log hyperbolic tangent model to obtain the indentation depth vs time curve for each duration of cycling. It was recorded that the nanoindentation creep displacement and the total displacement both lead free alloys joints increased with increased number of prior shear cycling. This was observed to be a common trend for all the joints presented in this paper.

In addition, the method for calculating the creep strain rate proposed by Mayo and Nix [144, 145] has been adopted in this study. According to the method, creep strain rate can be determined from instantaneous creep deformation and deformation rate using the following equation:

$$\dot{\varepsilon} = \frac{1}{h}\frac{dh}{dt} \tag{8.1}$$

As stated earlier, the Tabor relationship [134] was used to approximately evaluate the yield stress by dividing the hardness by 3. Figure 8.5 shows the variation of creep strain rate with the applied stress for each duration of prior cycling. From the graphs, it is understood that the creep strain rate at a fixed stress level increased with the increased duration of prior mechanical shear cycling for both materials. These increases were approximately 32X for SAC305 joint 3 and 24X for SAC305 joint 4 after 300 cycles for a stress level of 100 MPa.

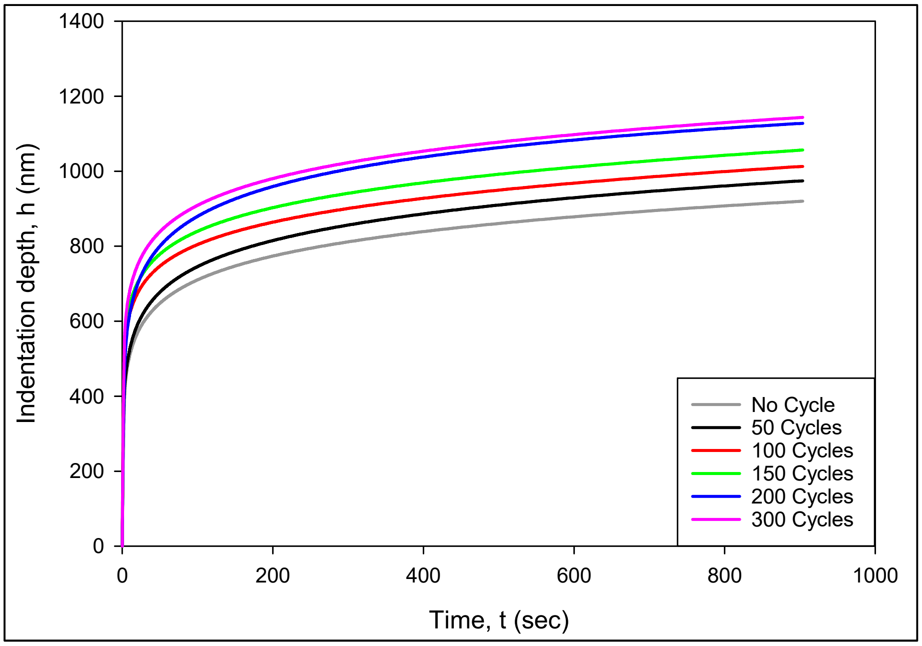

a) Joint 3

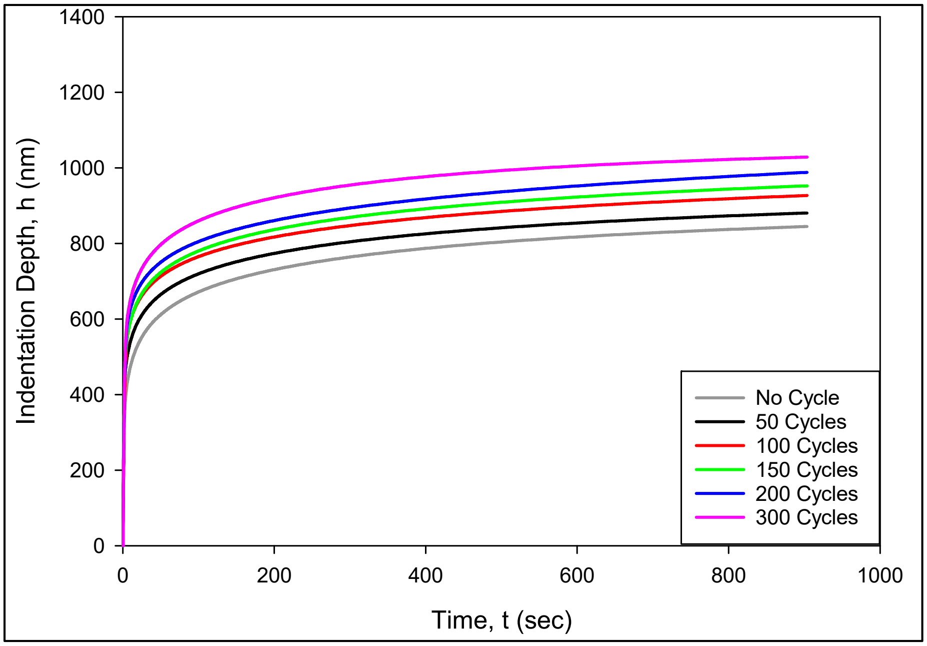

b) Joint 4

Figure 8.5 Creep Displacement vs. Time Curves for SAC305 Joint

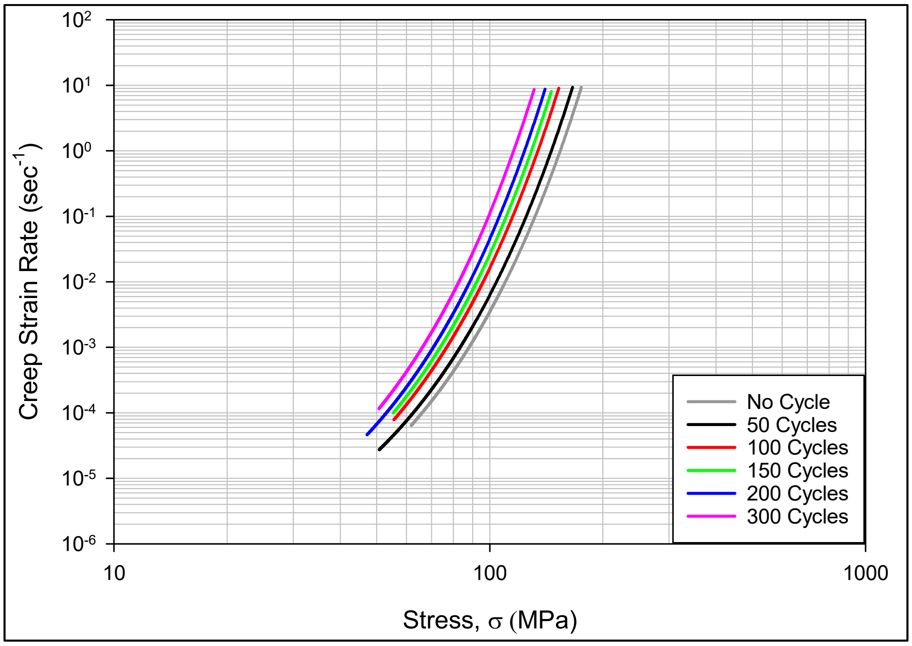

a) Joint 3

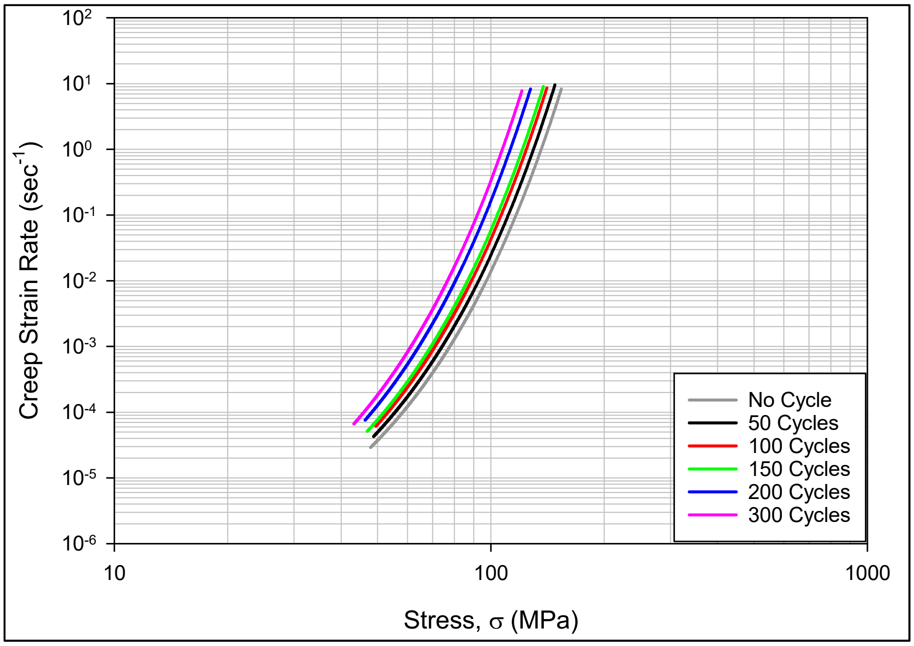

b) Joint 4

Figure 8.6 Creep Strain Rate vs. Stress curves for SAC305 Joint

It can be inferred from all the above results that mechanical cycling degrades the elastic modulus, hardness and creep strain rate. The mechanical behavior of a solder test can be closely attributed to its microstructure. Any changes in the microstructure of

SAC305 solder with cycling can give us an indication as to why we observe a degradation in its mechanical properties. In previous chapter, we observed that changes in microstructure of SAC305 solder uniaxial samples of a fixed region with mechanical cycling. As the cycling progressed, microcracks began developing along the subgrain boundaries of the β-Sn dendrites. With cycling, these cracks grew in length subsequently leading to the creation of larger transgranular cracks. It can thus be deduced that the degradation of the above measured mechanical properties were due to this sort of damage accumulation.

8.5 Summary

In this investigation, we have explored the effect of shear mechanical cycling on damage accumulation in SAC305 solder joints in a 3x3 BGA sample. Such studies are needed to help improve fatigue models for lead free solders. The mechanical cycling performed was done directly on the solder balls with a maximum peak load of 600 gf using an Instron Micromechanical tester. The samples were cycled for various durations (50, 100, 150, 200, 300 cycles) which were below the fatigue life of these joints. After each cyclic duration, the samples were either tested for changes in elastic modulus and hardness or creep by performing nanoindentation experiments on the sample. It was observed that the elastic modulus dropped by about 27-32% while the hardness dropped by about 12-16% after 300 cycles. The creep properties of the lead free solder joints also decreased with shear mechanical cycling. It was seen that for the same stress level, the creep strain rate increased by about 20X to 28X after the end of 300 cycles. We have also seen that with the cycling of lead free solder samples, small intergranular cracks form. These cracks tend to grow along the subgrain boundaries and increase in length with cycling, thus weakening the β-Sn dendrites and finally leading to the creation of larger transgranular cracks. One can thus infer that the degradation of the mechanical properties measured in this study can be attributed to the formation of these cracks.

.

CHAPTER 9

CONCLUSIONS

9.1 Literature Review

Literature review has been done on conventional and doped lead free solders, cyclic stress-strain behavior of these alloys, effects of thermo-mechanical cycling on solder microstructure, and effects of aging on solder fatigue properties and microstructure.

The mechanical properties of a solder are strongly influenced by its microstructure, which is controlled by its thermal history including its solidification rate and thermal exposures after solidification. Aging of lead free solders leads to degradations in their constitutive and failure behaviors. For example, research in the literature has shown that aging leads to large reductions in solder material properties including shear strength, elastic modulus, nanoindentation joint modulus and hardness, high strain rate mechanical behavior, creep response, and Anand model parameters. Other studies have shown that aging causes severe degradations in uniaxial cyclic stress-strain curves and fatigue life, shear cyclic stress-strain curves and fatigue life, fracture behavior, drop reliability, and thermal cycling reliability.

Dopants have been found to strongly influence the properties and behaviors of lead free solders. For Example, Bi helps to reduce solidification temperature, increases strength by means of precipitation hardening, helps to reduce IMC (Intermetallic Compound) layer thickness, and also reduce aging induced degradation of mechanical properties in lead free solder materials. Ni helps to improve thermal fatigue life and drop test performance by refining Sn grain size and reducing the IMC layer formation near the Cu pad. The effects of rear earth (RE) elements and nanoparticle addition on the properties of lead free solder was also discussed in this chapter.

The changes in solder mechanical behavior are a result of the evolution of the solder microstructure that occurs during aging. The most well-known and widely observed changes are coarsening of the Ag_3Sn and Cu_6Sn_5 intermetallic compounds (IMCs) present in the eutectic regions between beta-Sn dendrites. Several researchers have proposed empirical models to describe the growth of these secondary phase particles as a function of aging temperature and aging time, and related this growth to mechanical property changes.

9.2 Experimental Procedure

All the experimental procedures and the data processing steps were presented in chapter 3. For uniaxial tensile testing, micro-scale tensile specimens were prepared in a rectangular shaped hollow glass tube using a vacuum suction method. Typical dimension of the uniaxial tensile specimens were 80 (length) X 3 (width) X 0.5 (height) mm. Uniaxial tensile tests were performed using a micro tension torsion testing system.

For cyclic stress-strain testing, newly designed micro-cylinder shaped uniaxial lead free solder test specimens have been prepared in glass tubes using the same vacuum suction process. The cylindrical specimens were introduced to solve the buckling problem during compression in the cyclic or fatigue testing. The cyclic testing was performed using a tension/torsion thermo-mechanical test system. Gripping fixtures were designed and added to the test system to grip the cylindrical specimens. After introducing the cylindrical specimens and gripping fixtures, we have solved many problems such as buckling during compression, specimen breaks in the grip, and slippage during testing. After testing, empirical models were utilized to represent the stress-strain, creep, and cyclic stress-strain experimental data. To process the cyclic stress-strain data and calculate the areas of the associated hysteresis loops, a pair of hyperbolic tangent empirical models has been used to represent the tension portion and the compression portion of the stress-strain behavior in each cycle. Then, hysteresis loop area (plastic strain energy density), plastic strain range and peak stress can be determined for each cycle.

To study the solder microstructural changes subjected to both cyclic loading and aging, SAC305 and SAC_Q solder samples were formed with Reflow cooling profiles, and then microscopy cross-sections were prepared. After polishing, small indentation marks were added to the cross-sections to facilitate locating the identical regions of interest. Then the microstructural changes in the fixed regions during aging were examined using SEM. To study the effects of mechanical cycling on the solder microstructure, uniaxial samples with various durations of prior mechanical cycling have been prepared. The cycled microstructures were then examined using SEM.

To study the evolution of mechanical properties at joint level, we have explored the effect of shear mechanical cycling on damage accumulation in SAC305 solder joints in a 3x3 BGA sample. Nanoindentation experiments were performed using Hysitron TI950 TriboIndenter.

9.3 High Temperature Mechanical Behavior and Anand Parameters of Bi-Doped SAC Alloys

In this work, the mechanical behavior of several SAC+X lead free solder alloys at extreme high temperatures up to 200 °C has been investigated. The studied alloys included SAC_R (96.6Sn-0.9Cu-2.5Bi), SAC_Q (92.8Sn-3.4Ag-0.5Cu-3.3Bi), and Innolot (90.95Sn-3.8Ag-0.7Cu-3.0Bi-0.15Ni-1.4Sb). The solder uniaxial test specimens were formed in high precision rectangular cross-section glass tubes using a vacuum suction process. For each of 4 elevated temperatures (T = 125, 150, 175, and 200 °C), tensile stress-strain tests were performed at the strain rate of 0.001 sec^{-1}. For each alloy and testing temperature, the stress-strain curve shape and high temperature tensile properties (initial modulus, yield stress, and ultimate tensile strength) of the solders were measured and compared. As expected, the results have shown significant degradations of the mechanical properties of lead-free solders at higher temperatures. However, it was found that the addition of dopants (e.g. Bi, Ni, and Sb) in the SAC+X alloys improved their high temperature properties significantly. Both SAC_Q and Innolot alloys significantly outperformed SAC305 and SAC_R at all temperature levels.

SAC_Q lead free solder materials recommended for high reliability applications have been chemically analyzed and then mechanically tested in order to determine the nine Anand parameters. Test specimens were initially solidified with water quenched cooling profile. Results from the uniaxial tensile test, performed at three different strain rates (0.001, 0.0001 and 0.00001 sec-^{1}) and four different test temperatures (125, 150, 175, and 200 °C) were used to determine the Anand parameters for all the alloys mentioned before. These parameters were used to predict the stress-strain behavior of the corresponding solder alloy. The experimental results and the model predicted results were compared. A good correlation was found between Anand model predicted and experimentally obtained results. The correlation of experimental results with Anand model prediction shows a very small difference (< 10% in most conditions), thus, confirming the applicability of the model for a wide range of temperatures and strain rates.

9.4 Aging Induced Evolution of Cyclic Stress-Strain Behavior of Doped SAC Solder Alloys

In this study, three new SAC-Bi lead free solder materials recommended for high reliability applications have been subjected to cyclic in order to determine the cyclic stress-strain behavior and compared the results with conventional lead free solder alloys. Although the SAC_R material does not have any silver, it was shown close cyclic stress-strain properties to SAC305 due to the presence of Bismuth (Bi) along with a little higher percentage of Copper (Cu). The Innolot and SAC_Q materials were shown to have higher strengths than SAC305.

Later, the effects of aging on the cyclic stress-strain behavior of doped lead free solders have also been investigated. The evolution of hysteresis loop with aging has been characterized for the studied lead free solders. Prior to testing, cylindrical uniaxial lead free solder test specimens were prepared and aged (preconditioned) at 125 °C for various aging times (0, 5, 10, 20, 30, 45, 60, 90, and 180 days). After aging, the fabricated samples were subjected to strain controlled cyclic stress-strain loading (constant positive and negative strain limits) at room temperature (25 °C). For each set of cyclic stress-strain data, the four-parameter hyperbolic tangent empirical model has been used to fit the entire cyclic stress-strain curve. For conventional SAC305 lead free solder alloy, it has been found that the size and shape of the hysteresis loop changed dramatically during the first few days of aging, with slower changes occurring for longer aging times. It has been also observed that increased aging led to the drop of loop area and peak stress and the increase of plastic strain range, which indicates the increased ability of dislocation movement. For SAC_Q solder alloy, less significant changes of all the three parameters occurred within the first few days of aging. The evolutions of hysteresis loop area with long term aging have been also found close to stable. Therefore, SAC-Bi Alloy has been found to be highly resistant to aging induced degradations. Microstructural analysis has shown that the improved aging resistance is due to solid solution strengthening where the Bi-phases go into the solution in the β-Sn matrix during aging and enhance strength.

9.5 Evolution of Solder Mechanical Properties due to Cyclic Loading

To better understand the damage accumulation during fatigue testing, we have studied cycling induced evolution of mechanical behavior of SAC305 and SAC_Q lead free solders. Particularly, the evolutions of cyclic stress-strain curve, stress-strain curve and creep curve have been characterized and quantified. To study the evolution of the cyclic stress-strain behavior, the specimens have been subjected to cyclic stress/strain loading at room temperature (25 ºC) until fatigue failure. The cyclic stress-strain curves at after various durations of cycling have been examined. To study the effects of cycling on solder constitutive behavior, uniaxial samples with various durations of prior mechanical cycling have been prepared. The cycled samples were then subjected to stress-strain or creep testing. With increased mechanical cycling, damage accumulated in the specimen and its various mechanical properties degraded.

9.6 Aging Induced Microstructural Evolution in Lead Free Solders due to Mechanical Cycling Loading

The evolution of mechanical properties has been correlated with the observed microstructural changes caused by fatigue cycling. SEM has been utilized to examine the changes that occurred for each cycling condition. For both SAC305 and SAC_Q solder alloys, it has been found that the cycling induced damage consisted primarily of small intergranular cracks forming along the sub-grain boundaries within the β-Sn dendrites. These cracks continued to grow in size as the cycling continued, resulting in a weakening of the dendrite structure, and eventually resulting in the formation of large transgranular cracks. The distribution and size of the intermetallic particles in the inter-dendritic regions were observed to remain essentially unchanged with the application of the mechanical cyclic load.

New technique was developed using Scanning Electron Microscopy (SEM) to capture aging induced microstructural changes occurring within lead free solders. Unlike many prior studies, fixed regions in the solder joint cross-sections were monitored throughout the aging process, rather than examining different samples and/or different regions after the various aging exposures. Nanoindentation marks were added to the cross-sections at certain locations to facilitate locating the fixed regions of interest. After preparation of suitable cross-sectional samples, the samples were then aged at T = 125 °C, and the microstructures were observed and recorded in the selected regions after various prior cycled sample with and without aging using SEM. With this approach, microstructure evolution in a particular region of a solder alloy has been recorded as a function of number of cycles. For aged SAC305 solder alloy, IMC particles decreases during aging, while the average diameter of the particles increases significantly. In case of SAC_Q, we also observed that no significant changes have been noticed during the aging period. The observed increase of resistance against aging is due to the increase in strength from solid solution strengthening exceeding any reduction in strength caused by IMC and β-Sn phase coarsening. In summary, the doped SAC_Q alloy appears to be a promising solder material for use in thermal and/or mechanical loading not only because of improved cyclic properties but also for being strongly resistant to aging-induced evolution.

9.7 Evolution of the Mechanical Properties of Individual Lead Free Solder Joint Subjected to Mechanical Cycling

In this investigation, we have explored the effect of shear mechanical cycling on damage accumulation in SAC305 solder joints in a 3x3 BGA sample. Such studies are needed to help improve fatigue models for lead free solders. The mechanical cycling performed was done directly on the solder balls with a maximum peak load of 600 gf using an Instron Micromechanical tester. The samples were cycled for various durations (50, 100, 150, 200, 300 cycles) which were below the fatigue life of these joints. After each cyclic duration, the samples were either tested for changes in elastic modulus and hardness or creep by performing nanoindentation experiments on the sample. It was observed that the elastic modulus dropped by about 27-32% while the hardness dropped by about 12-16% after 300 cycles. The creep properties of the lead free solder joints also decreased with shear mechanical cycling. It was seen that for the same stress level, the creep strain rate increased by about 20X to 28X after the end of 300 cycles. We have also seen that with the cycling of lead free solder samples, small intergranular cracks form. These cracks tend to grow along the subgrain boundaries and increase in length with cycling, thus weakening the β-Sn dendrites and finally leading to the creation of larger transgranular cracks. One can thus infer that the degradation of the mechanical properties measured in this study can be attributed to the formation of these cracks.

9.8 Recommendation of Future Work

Following future work can be performed to extend the findings of this dissertation:

- Characterize and quantify the effects of aging on grain size and grain orientation of lead free solders in the same region using polarized light microscope and EBSD.
- Use the same procedures and methods to study the effects of aging and cycling on the microstructure of other doped lead free solders, such as Innolot.
- Quantitatively analyze the aging induced evolution of IMC particles in fixed regions due to mechanical cyclic loading.
- Study the changes of solder microstructure and recrystallization due to pure mechanical cyclic loading and thermo-cyclic loading using polarized light microscopy and compare the results.
- The experimental procedure to evaluate the mechanical properties evolution of individual solder joint presented in this dissertation can be used to perform creep testing under shear loading. Anand parameters can also be evaluated using these experimental results.
- Explore the effects of mechanical cycling on mechanical properties of lead sandwich samples using nanoindentation. The sandwich samples will be cycled for various cycles, and then use the nanoindentation system to determine the mechanical properties of the cycled sample for each cycling condition.

REFERENCES

[1] M. Abtew and G. Selvaduray, "Lead-free solders in microelectronics," *Materials Science and Engineering: R: Reports,* vol. 27, no. 5, pp. 95-141, 2000.

[2] P. T. Vianco, "Development of alternatives to lead-bearing solders," Proceeding of the Technical Program on Surface Mount International, San Jose, CA, 1993.

[3] N. C. Lee, "Getting Ready for Lead-free Solders," *Soldering & Surface Mount Technology,* vol. 9, no. 2, pp. 65-69, 1997.

[4] G. Zeng, S. D. McDonald, Q. Gu, K. Sweatman, and K. Nogita, "Effects of element addition on the β→ α transformation in tin," *Philosophical Magazine Letters,* vol. 94, no. 2, pp. 53-62, 2014.

[5] W. J. Plumbridge, "Tin pest issues in lead-free electronic solders," *Lead-Free Electronic Solders*, Springer, 2006, pp. 307-318.

[6] S. Cheng, C.-M. Huang, and M. Pecht, "A review of lead-free solders for electronics applications," *Microelectronics Reliability,* vol. 75, pp. 77-95, 2017.

[7] Q. B. Tao, L. Benabou, L. Vivet, V. N. Le, and F. B. Ouezdou, "Effect of Ni and Sb additions and testing conditions on the mechanical properties and microstructures of lead-free solder joints," *Materials Science and Engineering: A,* vol. 669, pp. 403-416, 2016.

[8] M. Hasnine, B. Tolla, and M. Karasawa, "Effect of Ge addition on wettability, copper dissolution, microstructural and mechanical behavior of SnCu–Ge solder alloy," *Journal of Materials Science: Materials in Electronics,* vol. 28, no. 21, pp. 16106-16119, 2017.

[9] J. S. Hwang, Implementing Lead-Free Electronics. McGraw-Hill, New York, 2005.

[10] Q. Zhang, A. Dasgupta, and P. Haswell, "Creep and High-Temperature Isothermal Fatigue of Pb-Free Solders," Proceedings of ASME InterPACK, no. 36908a, pp. 955-960, 2003.

[11] NCMS, "Lead-Free Solder Project Final Report," NCMS Report 0401RE96, 1997.

[12] K. S. Kim, S. H. Huh, and K. Suganuma, "Effects of Intermetallic Compounds on Properties of Sn–Ag–Cu Lead-Free Soldered Joints," Journal of Alloys and Compounds, vol. 352, no. 1, pp. 226-236, 2003.

[13] J.-W. Yoon, S.-W. Kim, and S.-B. Jung, "IMC Morphology, Interfacial Reaction and Joint Reliability of Pb-Free Sn–Ag–Cu Solder on Electrolytic Ni BGA Substrate," Journal of Alloys and Compounds, vol. 392, no. 1, pp. 247-252, 2005.

[14] D. Q. Yu and L. Wang, "The Growth and Roughness Evolution of Intermetallic Compounds of Sn–Ag–Cu/Cu Interface During Soldering Reaction," Journal of Alloys and Compounds, vol. 458, no. 1, pp. 542-547, 2008.

[15] C. M. L. Wu, D. Q. Yu, C. M. T. Law, and L. Wang, "Properties of Lead-Free Solder Alloys with Rare Earth Element Additions," Materials Science and Engineering: R: Reports, vol. 44, no. 1, pp. 1-44, 2004.

[16] Y. C. Chan and D. Yang, "Failure Mechanisms of Solder Interconnects under Current Stressing in Advanced Electronic Packages," Progress in Materials Science, vol. 55, no. 5, pp. 428-475, 2010.

[17] C. H. Wang and S. W. Chen, "Sn–0.7wt.%Cu/Ni Interfacial Reactions at 250°C," Acta Materialia, vol. 54, no. 1, pp. 247-253, 2006.

[18] K. S. Kim, S. H. Huh, and K. Suganuma, "Effects of intermetallic compounds on properties of Sn–Ag–Cu lead-free soldered joints," *Journal of Alloys and Compounds,* vol. 352, no. 1, pp. 226-236, 2003.

[19] D. Q. Yu and L. Wang, "The growth and roughness evolution of intermetallic compounds of Sn–Ag–Cu/Cu interface during soldering reaction," *Journal of Alloys and Compounds,* vol. 458, no. 1, pp. 542-547, 2008.

[20] M. McCormack, S. Jin, G. W. Kammlott, and H. S. Chen, "New Pb - Free Solder Alloy with Superior Mechanical Properties," Applied Physics Letters, vol. 63, no. 1, pp. 15-17 1993.

[21] H. Ma, J. C. Suhling, Y. Zhang, P. Lall, and M. J. Bozack, "The influence of elevated temperature aging on reliability of lead free solder joints," *Proceeding of the 57th Electronic Components and Technology Conference,* pp. 653-668, 2007.

[22] K. Nogita, "Stabilisation of Cu6Sn5 by Ni in Sn-0.7 Cu-0.05 Ni Lead-Free Solder Alloys," Intermetallics, vol. 18, no. 1, pp. 145-149, 2010.

[23] F. X. Che, J. E. Luan, and X. Baraton, "Effect of Silver Content and Nickel Dopant on Mechanical Properties of Sn-Ag-Based Solders," Proceedings of the 58th IEEE Electronic Components and Technology Conference, pp. 485-490, 2008.

[24] F. Guo, J. Lee, S. Choi, J. P. Lucas, T. R. Bieler, and K. N. Subramanian, "Processing and Aging Characteristics of Eutectic Sn-3.5 Ag Solder Reinforced with Mechanically Incorporated Ni Particles," Journal of Electronic Materials, vol. 30, no. 9, pp. 1073-1082, 2001.

[25] Z. G. Chen, Y. W. Shi, Z. D. Xia, and Y. F. Yan, "Study on the Microstructure of a Novel Lead-Free Solder Alloy SnAgCu-Re and Its Soldered Joints," Journal of Electronic Materials, vol. 31, no. 10, pp. 1122-1128, 2002.

[26] Z. G. Chen, Y. W. Shi, Z. D. Xia, and Y. F. Yan, "Study on the Microstructure of a Novel Lead-Free Solder Alloy SnAgCu-Re and Its Soldered Joints," Journal of Electronic Materials, vol. 31, no. 10, pp. 1122-1128, 2002.

[27] C. M. T. Law and C. M. L. Wu, "Microstructure Evolution and Shear Strength of Sn-3.5 Ag-Re Lead-Free BGA Solder Balls," Proceedings of the 6th IEEE CPMT Conference on High Density Microsystem Design and Packaging and Component Failure Analysis, pp. 60-65, 2004.

[28] N. C. Lee, "Lead-Free Soldering-Where the World Is Going," Advancing Microelectronics, vol. 26, no. 5, pp. 29-35, 1999.

[29] B. Z. Lee, D. N. Lee, "Spontaneous Growth Mechanism of Tin Whiskers," Acta Materialia, Vol. 46(10), 1998.

[30] W. B. Pearson, A Handbook of Lattice Spacings and Structure of Metals and Alloys, Vol.
2, Pergamon Press, London, 1958.

[31] P. T. Vianco, "Fatigue and creep of lead-free solder alloys: Fundamental properties," *ASM International,* pp. 67-106, 2005.

[32] S. Wiese *et al.*, "Constitutive behaviour of lead-free solders vs. lead-containing solders-experiments on bulk specimens and flip-chip joints," *Proceeding of the 51st Electronic Components and Technology Conference,* pp. 890-902, 2001

[33] R. J. McCabe and M. E. Fine, "Athermal and thermally activated plastic flow in low melting temperature solders at small stresses," *Scripta Materialia(USA),* vol. 39, no. 2, pp. 189-195, 1998.

[34] H. Ma and J. C. Suhling, "A review of mechanical properties of lead-free solders for electronic packaging," *Journal of Materials Science,* vol. 44, no. 5, pp. 1141-1158, 2009.

[35] J. H. Lau and Y.-H. Pao, *Solder joint reliability of BGA, CSP, flip chip, and fine pitch SMT assemblies*, McGraw-Hill, New York, 1997.

[36] R. W. Hertzberg, R. P. Vinci, and J. L. Hertzberg, *Deformation and Fracture Mechanics of Engineering Materials,* Wiley New York, 1996.

[37] W. Engelmaier, "Surface Mount Solder Joint Reliability: Issues, Design, Testing, Prediction," Workshop Notes, Engelmaier Associates, Inc., Mendham, NJ, 1995.

[38] T. J. Kilinski, J. R. Lesniak, B. I. Sandor, "Modern Approaches to Fatigue Life Prediction of SMT Solder Joints," Solder Joint Reliability Theory and Applications, Edited by J. H. Lau, Chapter 13, Van Nostrand Reinhold, 1991.

[39] J. Bauschinger, "On the Change of the Position of the Elastic Limit of Iron and Steel under Cyclic Variations of Stress," Mitt Mech-Tech Lab, Munich, Vol. 13, No. 1, 1886.

[40] J. Morrow, "Cyclic Plastic Strain Energy and Fatigue of Metals," Internal Friction, Damping and Cyclic Plasticity, STP 378, ASTM, West Conshohocken, PA, pp. 45, 1965.

[41] M. Hongtao, J. C. Suhling, P. Lall, and M. J. Bozack, "Reliability of the Aging Lead Free Solder Joint," Peoceedings of the 56th IEEE Electronic Components and Technology Conference, pp. 849-864, 2006.

[42] Z. Yifei, C. Zijie, J. C. Suhling, P. Lall, and M. J. Bozack, "The Effects of Aging Temperature on SAC Solder Joint Material Behavior and Reliability," Proceedings of 58th IEEE Electronic Components & Technology Conference, pp. 99-112, 2008.

[43] Z. Cai, Y. Zhang, J. C. Suhling, P. Lall, R. W. Johnson, and M. J. Bozack, "Reduction of Lead Free Solder Aging Effects Using Doped SAC Alloys," Proceedings of the 60th IEEE Electronic Components and Technology Conference, pp. 1493-1511, 2010.

[44] F. Che, W. Zhu, E. S. Poh, X. Zhang, and X. Zhang, "The study of mechanical properties of Sn–Ag–Cu lead-free solders with different Ag contents and Ni doping under different strain rates and temperatures," *Journal of Alloys and Compounds,* vol. 507, no. 1, pp. 215-224, 2010.

[45] F. Zhu, H. Zhang, R. Guan, and S. Liu, "Effects of temperature and strain rate on mechanical property of Sn96. 5Ag3Cu0. 5," *Journal of Alloys and Compounds,* vol. 438, no. 1-2, pp. 100-105, 2007.

[46] Y. Zhang, Z. Cai, J. C. Suhling, P. Lall, and M. J. Bozack, "The effects of SAC alloy composition on aging resistance and reliability," *Proceedings of the 59th Electronic Components and Technology Conference,* pp. 370-389, 2009.

[47] Y. Zhang, K. Kurumaddali, J. C. Suhling, P. Lall, and M. J. Bozack, "Analysis of the mechanical behavior, microstructure, and reliability of mixed formulation solder joints," *Proceedings of the 59th Electronic Components and Technology Conference,* pp. 759-770, 2009.

[48] M. Mustafa, Z. Cai, J. C. Suhling, and P. Lall, "The effects of aging on the cyclic stress-strain behavior and hysteresis loop evolution of lead free solders," *Proceedings of the 61st Electronic Components and Technology Conference,* pp. 927-939, 2011.

[49] M. Mustafa, J. C. Roberts, J. C. Suhling, and P. Lall, "The effects of aging on the fatigue life of lead free solders," *Proceedings of the 64th Electronic Components and Technology Conference,* pp. 666-683, 2014.

[50] J. Zhang, Thirugnanasambandam, S., Evans, J. L., Bozack, M. J., Zhang, Y., Suhling, J. C., "Correlation of aging effects on the creep rate and reliability in lead free solder joints," *SMTA Journal,* vol. 25(3), pp. 19-28 2012.

[51] J. Zhang *et al.*, "Thermal aging effects on the thermal cycling reliability of lead-free fine pitch packages," *IEEE Transactions on Components, Packaging and Manufacturing Technology,* vol. 3, no. 8, pp. 1348-1357, 2013.

[52] Z. Hai *et al.*, "Reliability comparison of aged SAC fine-pitch ball grid array packages versus surface finishes," *IEEE Transactions on Components, Packaging and Manufacturing Technology,* vol. 5, no. 6, pp. 828-837, 2015.

[53] M. Motalab *et al.*, "Improved predictions of lead free solder joint reliability that include aging effects," *Proceedings of the 62nd Electronic Components and Technology Conference,* pp. 513-531, 2012.

[54] M. Motalab *et al.*, "Correlation of reliability models including aging effects with thermal cycling reliability data," *Proceedings of the 63rd IEEE Electronic Components and Technology Conference,* pp. 986-1004, 2013.

[55] L. Anand, "Constitutive equations for the rate-dependent deformation of metals at elevated temperatures," *Journal of Engineering Materials and Technology,* vol. 104, no. 1, pp. 12-17, 1982.

[56] F. X. Che, H. L. J. Pang, W. H. Zhu, W. Sun, and A. Y. S. Sun, "Modeling constitutive model effect on reliability of lead-free solder joints," in *Proceedings of the 7th International Conference on Electronics Packaging Technology*, pp. 1-6, 2006.

[57] M. Pei and J. Qu, "Constitutive modeling of lead-free solders," *Proceedings of the International Symposium on Advanced Packaging Materials,* pp. 45-49, 2005.

[58] K. Mysore, G. Subbarayan, V. Gupta, and R. Zhang, "Constitutive and aging behavior of Sn3. 0Ag0. 5Cu solder alloy," *Electronics Packaging Manufacturing, IEEE Transactions on,* vol. 32, no. 4, pp. 221-232, 2009.

[59] M. Motalab, Z. Cai, J. C. Suhling, and P. Lall, "Determination of Anand constants for SAC solders using stress-strain or creep data," *Proceedings of ITherm,* pp. 910-922, 2012.

[60] N. Bai, X. Chen, and H. Gao, "Simulation of uniaxial tensile properties for lead-free solders with modified Anand model," *Materials & Design,* vol. 30, no. 1, pp. 122-128, 2009.

[61] M. Amagai, M. Watanabe, M. Omiya, K. Kishimoto, and T. Shibuya, "Mechanical characterization of Sn–Ag-based lead-free solders," *Microelectronics Reliability,* vol. 42, no. 6, pp. 951-966, 2002.

[62] Y. Kim, H. Noguchi, and M. Amagai, "Vibration fatigue reliability of BGA-IC package with Pb-free solder and Pb–Sn solder," *Microelectronics Reliability,* vol. 46, no. 2, pp. 459-466, 2006.

[63] M. Basit, M. Motalab, J. C. Suhling, P. Lall, "Viscoplastic Constitutive Model for Lead-Free Solder Including Effects of Silver Content, Solidification Profile, and Severe Aging," Proceedings of the InterPACK, San Francisco, California, USA.

[64] M. Huang and L. Wang, "Effects of Cu, Bi, and In on microstructure and tensile properties of Sn-Ag-X (Cu, Bi, In) solders," *Metallurgical and Materials Transactions A,* vol. 36, no. 6, pp. 1439-1446, 2005.

[65] M. Matahir, L. Chin, K. Tan, and A. Olofinjana, "Mechanical strength and its variability in Bi-modified Sn-Ag-Cu solder alloy," *Journal of Achievement in Materials and Manufacturing Engineering,* vol. 46, pp. 50-56, 2011.

[66] R. S. Pandher, B. G. Lewis, R. Vangaveti, and B. Singh, "Drop shock reliability of lead-free alloys–effect of micro-additives," *Proceedings 57th Electronic Components and Packaging Technology Conference,* pp. 669-676, 2007.

[67] Z. Zhao, L. Wang, X. Xie, Q. Wang, and J. Lee, "The influence of low level doping of Ni on the microstructure and reliability of SAC solder joint," *Proceedings of 9th International Conference on Electronic Packaging Technology & High Density Packaging,* pp. 1-5, 2008.

[68] I. De Sousa, D. W. Henderson, L. Parry, S. K. Kang, and D.-Y. Shih, "The influence of low level doping on the thermal evolution of SAC alloy solder joints with Cu pad structures," *Proceeding of the 56th Electronic Components and Technology Conference,* pp. 1454-1461, 2006.

[69] J. H. Lee, S. Kumar, H. J. Kim, Y. W. Lee, and J. T. Moon, "High thermo-mechanical fatigue and drop impact resistant Ni-Bi doped lead free solder," in *Proceedings of the 64th Electronic Components and Technology Conference*, pp. 712-716, 2014.

[70] T. S. Yeung, H. Sze, K. Tan, J. Sandhu, C.-W. Neo, and E. Law, "Material characterization of a novel lead-free solder material—SACQ," *Proceedings of the 64th IEEE Electronic Components and Technology Conference,* pp. 518-522, 2014.

[71] L. Sun and L. Zhang, "Properties and microstructures of Sn-Ag-Cu-X lead-free solder joints in electronic packaging," *Advances in Materials Science and Engineering,* vol. 2015, 2015.

[72] M. Sadiq, R. Pesci, and M. Cherkaoui, "Impact of thermal aging on the microstructure evolution and mechanical properties of lanthanum-doped tin-silver-copper lead-free solders," *Journal of electronic materials,* vol. 42, no. 3, pp. 492-501, 2013.

[73] H. T. Lee, Y.-F. Chen, T.-F. Hong, K.-T. Shih, and C.-w. Hsu, "Microstructural evolution of Sn-3.5 Ag solder with lanthanum addition," *Proceedings of International Conference on Electronic Packaging Technology & High Density Packaging,* pp. 617-622, 2009.

[74] H. Hao, Y. Shi, Z. Xia, Y. Lei, and F. Guo, "Microstructure evolution of SnAgCuEr lead-free solders under high temperature aging," *Journal of Electronic Materials,* vol. 37, no. 1, pp. 2-8, 2008.

[75] D. B. Witkin, "Influence of microstructure on mechanical behavior of Bi-containing Pb-Free solders," *Proceedings of IPC APEX EXPO Conference and Exhibition,* pp. 540-547, 2013.

[76] A. Delhaise, D. Perovic, and P. Snugovsky, "The effects of Bi and aging on the microstructure and mechanical properties of Sn-rich alloys," *Proceedings of the International Conference on Soldering and Reliability,* 2015.

[77] H. D. Solomon, "Creep Strain Rate Sensitivity and Low Cyclic Fatigue of 60/40 Solder," Brazing and Soldering, Vol. 11, pp. 68-75. 1986.

[78] Q. Guo, E. C. Cutiongco, L. M. Keer, and M. E. Fine, "Thermomechanical Fatigue Life Prediction of 63Sn/37Pb Solder," Journal of Electronic Packaging, Vol. 114, pp.145-151, 1992.

[79] E. P. Busso, M. Kitano, and T. Kumazawa, "A Visco-plastic Constitutive Model for 60/40 Tin-lead Solder used in IC Package Joints," Journal of Engineering Materials Technology, Vol. 114, pp. 333-337, 1992.

[80] D. R. Frear, S. N. Burchett, M. K. Neilsen, and J. J. Stephens, "Microstructurally Based Finite Element Simulation of Solder Joint Behavior," Soldering and Surface Mount Technology, Vol. 2, pp. 39-42, 1997.

[81] D. L. McDowell, M. P. Miller, and D. C. Brooks, "A Unified Creep-Plasticity Theory for Solder Alloys," Fatigue of Electronic Materials, ASTM STP, Vol. 1153, pp. 42-59, 1994.

[82] J. H. Lau (Ed.), Solder Joint Reliability, Theory and Applications, Van Nostrand Reinhold, New York, 1991.

[83] X. Q. Shi, W. Zhou, H. L. J. Pang, and Z. P. Wang, "Effect of Temperature and Strain Rate on Mechanical Properties of 63Sn/37Pb Solder Alloy." Journal of Electronic Packaging, Vol. 121, pp. 179-185, 1999.

[84] X. J. Yang, C. L. Chow, and K. J. Lau, "Time Dependent Cyclic Deformation and Failure of 63Sn/37Pb Solder Alloy," International Journal of Fatigue, Vol. 25, pp. 533-546, 2003.

[85] P. M. Hall, "Forces, Moments, and Displacements During Thermal Chamber Cycling of Leadless Ceramic Chip Carriers Soldered to Printed Boards," IEEE Transactions on Components, Hybrids, and Manufacturing Technology, Vol. 7(4), pp. 314-327. 1984.

[86] P. M. Hall, "Creep and Stress Relaxation in Solder Joints of Surface Mounted Chip Carriers," IEEE Transactions on Components, Hybrids and Manufacturing Technology, Vol. 12(4), pp. 556-565, 1987

[87] Y. H. Pao, S. Badgley, R. Govila, and E. Jih, "An experimental and modeling study of the thermal cyclic behavior of Sn–Cu and Sn–Pb solder joints," Electronic Packaging Materials Science VII, (Materials Research Society Symposium, Number 323), pp. 153-158, 1994.

[88] Y. H. Pao, K. L. Chen, and A. Y. Kuo, "A Nonlinear and Time Dependent Finite Element Analysis of Solder Joints in Surface Mounted Components under Thermal Cycling," in Proceedings of the Materials Research Society Symposium, Vol. 226, pp. 23-28, 1991.

[89] Y. H. Pao, S. Badgley, R. Govila, and E. Jih, "An Experimental and Finite Element Study of Thermal Fatigue Fracture of Pb-Sn Solder Joints," Journal of Electronic Packaging, Vol. 115, pp. 1-8, 1993.

[90] P. Haacke, A. F. Sprecher, and H. Conrad, "Computer Simulation of Thermomechanical Fatigue of Solder Joints Including Microstructural Coarsening," Journal of Electronic Packaging, Vol. 115, pp. 153-158, 1993.

[91] C. H. Raeder, L. E. Felton, R. W. Messler, and L. F. Coffin, "Thermomechanical Stress-Strain Hysteresis of Sn-Bi Eutectic Solder Alloy," Proceedings of the IEEE International Electronics Manufacturing Technology Symposium, 263-268, 1995.

[92] M. Dusek, and C. Hunt, "Low Cycle Isothermal Fatigue Properties of Lead-free Solders," Soldering and Surface Mount Technology, pp. 25-32, 2007.

[93] B. Hu, J. Zhou, Y. Yang, F. Wan, "The Effect of Temperature on Low Cycle Fatigue of an Eutectic Solder," Proceeding of International Conference on Electronic Materials and Packaging, pp. 1-5, 2006.

[94] X. Q. Shi, H. L. J. Pang, W. Zhou, Z. P. Wang, , "A Modified Energy-Based Low Cycle Fatigue Model For Eutectic Solder Alloy," Scripta Materialia, Vol. 41(3), pp. 289-296, 1999.

[95] C. Kanchanomai, Y. Mutoh, "Low-Cycle fatigue prediction model for Pb-free solder 96.5Sn-3.5Ag," Journal of Electronic Materials, Vol. 33, No. 4, 2004.

[96] J. H. L. Pang, B. S. Xiong, and T. H. Low, "Creep and Fatigue Characterization of Lead Free 95.5An-3.8Ag0.7Cu Solder," Proceedings of the 54th Electronic Components and Technology Conference, pp. 1333-1337, 2004.

[97] D. Herkommer, J. Punch, and M. Reid, "A Reliability Model for SAC Solder Covering Isothermal Mechanical Cycling and Thermal Cycling Conditions," Journal of Microelectronics Reliability, Vol. 50, pp. 116-126, 2010.

[98] Q. Zhang, and A. Dasgupta, "Constitutive and Durability Properties of Selected Lead-Free Solders," Pb-Free Electronics, Chapter 6, Edited by M. Pecht and S. Ganesan, 2nd Edition, Wiley, 2006.

[99] Q. Zhang, A. Dasgupta,. and P. Haswell, "Isothermal Mechanical Durability of Three Selected Pb-Free Solders: Sn3.9Ag0.6Cu, Sn3.5Ag, and Sn0.7Cu," Journal of Electronic Packaging, Vol. 127(4), pp. 512-522, 2005.

[100] R. S. Whitelaw, R. W. Neu, and D. T. Scott, "Deformation Behavior of Two Lead-Free Solders: Indalloy 227 and Castin Alloy," Journal of Electronic Packaging, Vol. 121(2), pp. 99-107, 1999.

[101] T. K. Korhonen, P. L. Lahman, M. A. Korhonen, and W. D. Henderson, "Isothermal Fatigue Behavior of the Near Eutectic Sn-Ag-Cu Alloy Between -25 ºC and 125 ºC," Journal of Electronic Materials, Vol. 36(2), pp. 173-178, 2007.

[102] J. K. Shang, Q. L. Zeng, L. Zhang, and Q. S. Zhu, "Mechanical Fatigue of Snrich Pb-Free Solder Alloys," Journal of Material Science: Materials in Electronics, Vol. 18, pp. 211-227, 2007.

[103] C. Andersson, Z. Lai, J. Liu, H. Jiang, and Y. Yu, "Comparison of Isothermal Mechanical Fatigue Properties of Lead-Free Solder Joints and Bulk Solders," Material Science and Engineering A, Vol. 394, pp. 20-27, 2005.

[104] Y. Kanda, Y. Kariya, Y. Oto, "Influence of Cyclic Strain-Hardening Exponent on Fatigue Ductility Exponent for a Sn-Ag-Cu Micro-Solder Joint," Journal of Electronic Materials, Vol. 41, No. 3, pp. 580-587, 2012.

[105] Fossum, A. F., Vianco, P. T., Neilsen, M. K., Pierce, D. M., "A Practical Viscoplastic Damage Model for Lead-free Solder," Journal of ElectronicPackaging, Vol. 128 pp. 71-81, 2006.

[106] C. Andersson, P. Sun, J. Liu, "Low Cycle Fatigue of Sn-based Lead-free Solder Joints and the Analysis of Fatigue Life Prediction Uncertainty," Proceedings of High Density Microsystem Design and Packaging and Component Failure Analysis conference, pp. 272-279, 2006.

[107] J. Lau, R. Lee, D. Shangguan, "Thermal Fatigue-Life Prediction of Lead-Free Solder Joints," Proceedings of International Mechanical Engineering Congress and Exposition (IMECE04), pp. 1-6, 2004.

[108] H. Chen, J. Han, J. Li, M. Li, “Inhomogeneous Deformation and Microstructure Evolution of Sn-Ag-Based Solder Interconnects During Thermal Cycling and Shear Testing,” Microelectronics Reliability, Vol. 52, pp. 1112-1120, 2012.

[109] M. Berthou, P. Retailleau, H. Fremont, A. Guedon-Gracia, C. Jephos-Davennel, “Microstructure Evolution Observation for SAC Solder Joint: Comparison between Thermal Cycling and Thermal Storage,” Microelectronics Reliability, Vol. 49, pp. 1267-1272, 2009.

[110] L. Yin, L. Wentlent, L. Yang, B. Arfaei, A. Oasaimeh, P. Borgesen, “Recrystallization and Precipitate Coarsening in Pb-Free Solder Joints During Thermomechanical Fatigue,” Journal of Electronic Materials, Vol. 41, pp. 241-252, 2012.

[111] I. Dutta, D. Pan, R. A. Marks, S. G. Jadhav, “Effect of Thermo-Mechanically Induced Microstructural Coarsening on the Evolution of Creep Response of SnAg-Based Microelectronic Solders,” Materials Science and Engineering A, Vol. 410-411, pp. 48-52, 2005.

[112] I. Dutta, P. Kumar, G. Subbarayan, “Microstructural Coarsening in Sn-Ag-based Solders and Its Effects on Mechanical Properties,” The Journal of The Minerals, Metals & Materials Society, Vol. 61, pp. 29-38, 2009.

[113] L. Qi, J. Huang, X. Zhao, H. Zhang, “Effect of Thermal-Shearing Cycling on Ag_3Sn Microstructural Coarsening in SnAgCu Solder,” Journal of Alloys and Compounds, Vol. 469, pp. 102-107, 2009.

[114] M. Erinc, P. J. G. Schreurs, M. G. D. Geers, “Intergranular Thermal Fatigue Damage Evolution in SnAgCu Lead-Free Solder,” Mechanics of Materials, Vol. 40, 780-791, 2008.

[115] H. Chen, L. Wang, J. Han, M. Li, H. Liu, “Microstructure, Orientation and Damage Evolution in SnPb, SnAgCu, and Mixed Solder Interconnects Under Thermomechanical Stress,” Microelectronic Engineering, Vol. 96, pp. 82-91, 2012.

[116] L. Xu, J. H. L. Pang, F. Che, “Impact of Thermal Cycling on Sn-Ag-Cu Solder Joints and Board-Level Drop Reliability,” Journal of Electronic Materials, Vol. 37, pp. 880-886, 2008.

[117] G. Cuddalorepatta, A. Dasgupta, “Effect of Cyclic Fatigue Damage Accumulation on the Elastic-Plastic Properties of SAC305 Solders,” Thermal, Mechanical and Multi-Physics simulation and Experiments in Microelectronics and Microsystems, pp. 1-7. 2009.

[118] M. A. Matin, W. P. Vellinga, M. G. D. Geers, “Thermomechanical Fatigue Damage Evolution in SAC Solder Joints,” Materials Science and Engineering A, Vol. 445-446, pp. 73-85, 2007.

[119] M. A. Matin, W. P. Vellinga, M. G. D. Geers, “Microstructure Evolution in a Pb-Free Solder Alloy During Mechanical Fatigue,” Materials Science and Engineering A, Vol. 431, pp. 166-174, 2006.

[120] U. Sahaym, B. Talebanpour, S. Seekins, I. Dutta, P. Kumar, and P. Borgesen, "Recrystallization and Ag3Sn particle redistribution during thermomechanical treatment of bulk Sn–Ag–Cu solder alloys," *IEEE Transactions on Components, Packaging and Manufacturing Technology,* vol. 3, no. 11, pp. 1868-1875, 2013.

[121] M. Maleki, J. Cugnoni, and J. Botsis, "Isothermal ageing of SnAgCu solder alloys: three-dimensional morphometry analysis of microstructural evolution and its

effects on mechanical response," *Journal of Electronic Materials,* vol. 43, no. 4, pp. 1026-1042, 2014.

[122] A. Telang *et al.*, "Grain-boundary character and grain growth in bulk tin and bulk lead-free solder alloys," *Journal of Electronic Materials,* vol. 33, no. 12, pp. 1412-1423, 2004.

[123] S. L. Allen, M. R. Notis, R. R. Chromik, and R. P. Vinci, "Microstructural evolution in lead-free solder alloys: Part I. Cast Sn–Ag–Cu eutectic," *Journal of Materials Research,* vol. 19, no. 5, pp. 1417-1424, 2004.

[124] P. Kumar, B. Talenbanpour, U. Sahaym, C. Wen, and I. Dutta, "Microstructural evolution and some unusual effects during thermo-mechanical cycling of Sn-Ag-Cu alloys," *Proceedings of ITherm* pp. 880-887, 2012.

[125] P. Chauhan, S. Mukherjee, M. Osterman, A. Dasgupta, and M. Pecht, "Effect of isothermal aging on microstructure and creep properties of SAC305 solder: a micromechanics approach," *Proceedings of InterPACK,* 2013.

[126] W. Yang, R. W. Messler, and L. E. Felton, "Microstructure evolution of eutectic Sn-Ag solder joints," *Journal of Electronic Materials,* vol. 23, no. 8, pp. 765-772, 1994.

[127] T.-C. Chiu, K. Zeng, R. Stierman, D. Edwards, and K. Ano, "Effect of thermal aging on board level drop reliability for Pb-free BGA packages," *Proceedings of the 54th Electronic Components and Technology Conference,* pp. 1256-1262, 2004.

[128] A. R. Fix, W. Nüchter, and J. Wilde, "Microstructural changes of lead-free solder joints during long-term ageing, thermal cycling and vibration fatigue," *Soldering & Surface Mount Technology,* vol. 20, no. 1, pp. 13-21, 2008.

[129] S. Ahat, M. Sheng, and L. Luo, "Microstructure and shear strength evolution of SnAg/Cu surface mount solder joint during aging," *Journal of Electronic Materials,* vol. 30, no. 10, pp. 1317-1322, 2001.

[130] W. K. Choi and H. M. Lee, "Effect of soldering and aging time on interfacial microstructure and growth of intermetallic compounds between Sn-3.5 Ag solder alloy and Cu substrate," *Journal of Electronic Materials,* vol. 29, no. 10, pp. 1207-1213, 2000.

[131] A. Z. Akhtar, K. H. Wirda, I. S. R. Aisha, and I. Mahadzir, "Microstructure evolution at the solder joint during isothermal aging," *Proceedings of the 36th International Electronic Manufacturing Technology Conference,* pp. 1-5, 2014.

[132] M. Berthou, P. Retailleau, H. Frémont, A. Guédon-Gracia, and C. Jéphos-Davennel, "Microstructure evolution observation for SAC solder joint: Comparison between thermal cycling and thermal storage," *Microelectronics Reliability,* vol. 49, no. 9-11, pp. 1267-1272, 2009.

[133] W. C. Oliver and G. M. Pharr, "An improved technique for determining hardness and elastic modulus using load and displacement sensing indentation experiments," *Journal of Materials Research,* vol. 7, no. 6, pp. 1564-1583, 1992.

[134] D. Tabor, *The Hardness of Metals*. Oxford university press, 2000.

[135] P. Zhang, S. Li, and Z. Zhang, "General relationship between strength and hardness," *Materials Science and Engineering: A,* vol. 529, pp. 62-73, 2011.

[136] D. Herkommer, J. Punch, and M. Reid, "A reliability model for SAC solder covering isothermal mechanical cycling and thermal cycling conditions," *Microelectronics Reliability,* vol. 50, no. 1, pp. 116-126, 2010.

[137] G. Z. Wang, Z. N. Cheng, K. Becker, and J. Wilde, "Applying Anand model to represent the viscoplastic deformation behavior of solder alloys," *Journal of Electronic Packaging,* vol. 123, no. 3, pp. 247-253, 2001.

[138] D. Bhate, D. Chan, G. Subbarayan, T. C. Chiu, V. Gupta, and D. R. Edwards, "Constitutive behavior of Sn3. 8Ag0. 7Cu and Sn1. 0Ag0. 5Cu alloys at creep and low strain rate regimes," *IEEE Transactions on Components and Packaging Technologies,* vol. 31, no. 3, pp. 622-633, 2008.

[139] D. A. Porter, K. E. Easterling, and M. Sherif, *Phase Transformations in Metals and Alloys, (Revised Reprint)*, CRC press, 2009.

[140] R. E. Smallman, *Modern physical metallurgy*, 4th ed. Elsevier, 2016.

[141] R. Boistelle and J. Astier, "Crystallization mechanisms in solution," *Journal of Crystal Growth,* vol. 90, no. 1-3, pp. 14-30, 1988.

[142] Y. D. Han *et al.*, "A modified constitutive model for creep of Sn–3.5Ag–0.7Cu solder joints," *Journal of Physics D: Applied Physics,* vol. 42, no. 12, p. 125411, 2009.

[143] S. Su, F. Akkara, M. Abueed, M. Jian, S. Hamasha, J. C. Suhling, P. Lall, “Fatigue Properties of Lead-Free Doped Solder Joints” *Proceedings of ITherm 2018*, pp. 1243-1248, San Diego, CA, May 29 - June 1, 2018.

[144] M. Mayo and W. Nix, "A micro-indentation study of superplasticity in Pb, Sn, and Sn-38 wt% Pb," *Acta Metallurgica,* vol. 36, no. 8, pp. 2183-2192, 1988.

[145] M. Mayo, R. Siegel, A. Narayanasamy, and W. Nix, "Mechanical properties of nanophase TiO 2 as determined by nanoindentation," *Journal of Materials Research,* vol. 5, no. 5, pp. 1073-1082, 1990.